

Image sensor technology for visualizing
multi-neurotransmitters

(多項目の神経伝達物質を可視化可能な
イメージセンサ技術)

March, 2019

Doctor of Philosophy (Engineering)

Lee You-Na

李 宥奈

Toyohashi University of Technology

Contents

Abstract	iii
1 Introduction	1
1.1 Chemical communications between neural networks.....	1
1.2 How have we been monitoring chemical signals?	4
1.3 Can we provide a better tool?	7
1.4 Outline.....	7
2 Theories	8
2.1 The ISFET	8
2.2 Electrolyte-solid interface	9
2.2.1 Reference electrode.....	9
2.2.2 EDL at the gate surface	11
2.3 Imaging of pH distribution in real-time.....	12
2.3.1 pH image sensor	13
2.3.2 CCD technology for the pH-image sensor	13
2.4 Bio-image sensors for multiplex detection	16
3 Experimental methods and materials	18
3.1 Preparing pH image sensor.....	18
3.2 Measurement setup	19
3.3 Patterning enzyme-immobilized membrane	21
3.4 Preventive measures against H ⁺ diffusion.....	22
3.4.1 Barrier layers	22
3.4.2 Microhole array	22
4 Enzyme-immobilization technique	23
4.1 Patterned enzyme-immobilized membranes	23
4.2 Fabrication	24
4.3 Optimization - ATP and H ⁺ image sensor	25
4.3.1 The patterned enzyme-immobilized membrane	25
4.3.2 Detecting and real-time imaging in ATP and H ⁺ dynamics	27

5	Bio-image sensor	30
5.1	ATP, ACh and H ⁺ image sensor	30
5.2	Diffusion characteristics of H ⁺ and neurotransmitters	31
5.3	Bio-image sensor design	33
5.4	Imaging of ATP and ACh	33
5.5	Sensing characteristics	36
5.6	Additional investigation – Microhole array	37
5.6.1	Optimizing the array height	39
5.6.2	Comparison of H ⁺ diffusion	40
6	High performance pH-image sensor	42
6.1	Enhanced platform with higher spatio-temporal resolution	42
6.2	Operating principle	44
6.3	Sensor chip design and fabrication	47
6.3.1	Pixel structure	47
6.3.2	Array architectures	50
6.4	Sensor characterization	51
6.4.1	Test setup	51
6.4.2	Sensing parameters	53
6.4.3	Summary	58
6.5	Evaluation of practical spatial resolution	60
6.5.1	Experimental evaluation method	60
6.5.2	Comparison with simulation result	63
7	Concluding remarks	64
	References	66
	Acknowledgements	74

Abstract

Recently the scientific studies of the nervous system have increased substantially with advances in analytical equipment. Those are wildly contributed it possible to understand how biochemical signals are transmitted through synaptic junctions by the release and the feedback of neurotransmitters. Their studies and the development of medicines require effective analysis equipment to quantify biochemical activities in neuronal communications and several analytical techniques have been developed. However, most of the analytical techniques focus on the detection of a single neurotransmitter, even though neurons communicate in a complex interaction of neurotransmitters. It led to the development of ISFET array based bio-image sensor which is portable and customizable as well as implantable for long-term recording. When comparing to neural probe arrays which are successfully applied to electrical signal recording in the brain, biochemical recording may be more complicated due to the diversity of neurotransmitters, but it is very encouraging by their similarity between the probe and ISFET arrays.

In this thesis, we will introduce a bio-image sensor which is ISFET based enzyme sensor array with integrated with readout in order to monitor spatiotemporal activities of various neurotransmitters in the same time.

This thesis consists of three main parts:

1. We invented new enzyme-immobilization technique using conventional photolithography. Before developing a bio-image sensor used for spatiotemporal monitoring of more than two neurotransmitters, we proposed an enzyme-immobilization technique that is the integration of an imaging device technology and ISFET based enzyme sensor. Using this technique, we can not only simply select the kinds of proton-consuming or-generating enzymes according to the neurotransmitters wishing to analyze, but also immobilize them in a planned shape on a pH image sensor by conventional photolithography technology. The prototype applying the suggested technique was fabricated and tested to image the concentration gradient of ATP and H^+ . During the measurements, we became interested in H^+ diffusion via liquid, since the degraded ATP also by enzymatic reaction generates H^+ and the diffused H^+ were able to contribute to signal interrupting among neighboring pixels. When

designing and placement of enzyme-immobilized pixels, the crosstalk by the H^+ diffusion should be considered to improve the target discriminability of a bio-image sensor.

2. We then applied this technique to fabricate ATP, ACh and H^+ image sensor as a further development of our previous research. This bio-image sensor contained a patterned enzyme-immobilized membrane, as small as a pixel size, to enhance spatial resolution. Moreover, several attempts, such as new pattern placements, barrier layers and microhole arrays, were attempted to reduce the H^+ diffusion via liquid. The fabricated bio-image sensors were demonstrated to confirm their multi-detection and discrimination abilities to visualize the concentration changes of ATP and ACh in real-time 2D images.

3. Additionally, we modified the circuit design of the pH-image sensor to improve spatiotemporal resolution in order to investigate the neural networking in detail. The pH image sensor was developed toward large-scale, high-density and fast frame rate imaging. The pH image sensor was fabricated by a modified CMOS process technology. A small pixel pitch was achieved by utilizing a shrunken in-pixel circuit and an efficiently arranged readout circuit architecture. Moreover, the frame rate was able to accelerate by operating steps of measuring and read out in parallel. We demonstrated the imaging capability with our evaluation method for practical high-spatial resolution in biological environments and compared the experimental result with the simulation result to figure out the reason then.

Introduction

1.1 Chemical communications in neural networks

During the second half of the twentieth century, the scientific studies of the nervous system increased substantially with advances in analysis equipment. Those are widely contributed it possible to understand how electrical and electrochemical signals are transmitted through synaptic junctions by the release and feedback of neurotransmitters¹. Figure 1 illustrates the electrical signal (action potential) used to communicate long distance rapidly along axons of neurons and the electrochemical signal (neurotransmission) which is accomplished by ions and neurotransmitters in order to communicate between neurons. Their signaling mechanisms have been investigated activities to understand brain functions and to expend the knowledge for treating nervous disease, depression, drug

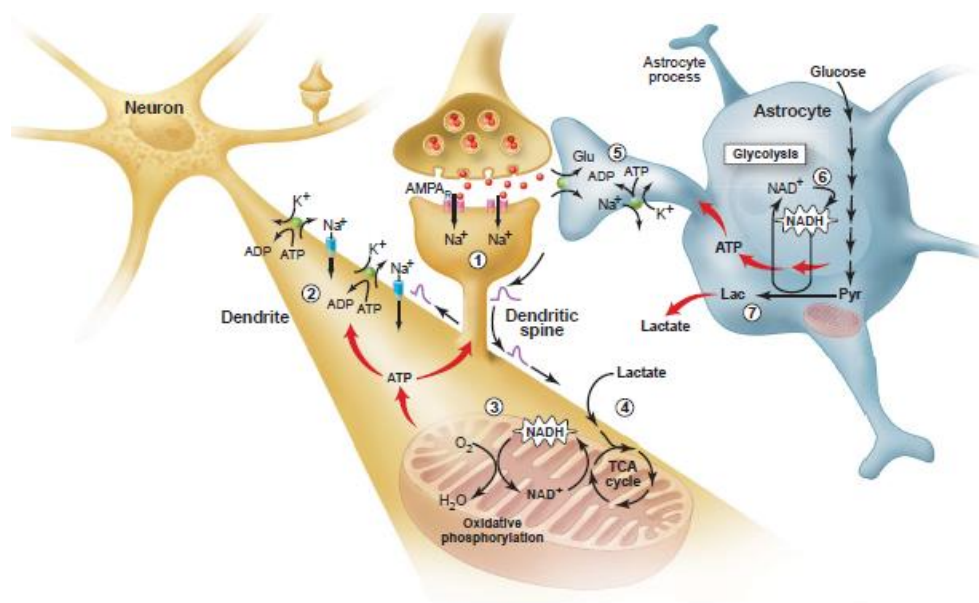
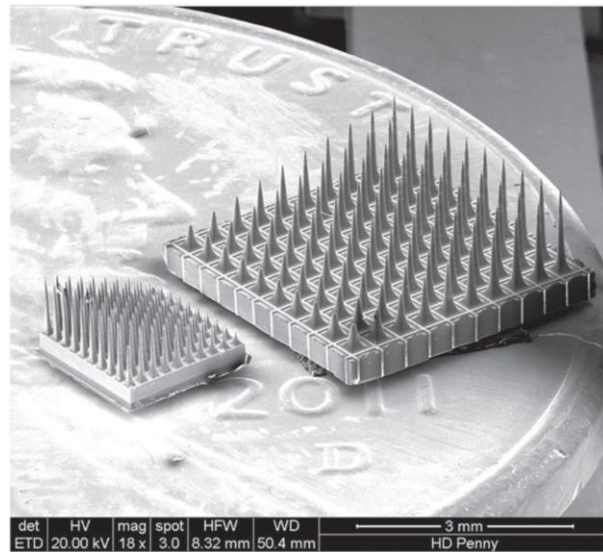


Figure 1 Brain energetics with electrical and electrochemical signaling pathways among neurons and glia cells with permission from the publisher¹.



(a)



(b)

Figure 2 (a) Utah electrode arrays, (b) Recording and using the neural signal to move a robotic arm with the Utah electrode array. with permission from the publisher ⁹

dependence, Alzheimer's disease, Parkinson's disease etc²⁻⁷, as well as upgrade human as connecting between our brain and external machines.

Because it is easier to measure of electricity than concentration changes of different chemicals, the technologies to record and stimulate neural activities by electrical signals have been already reached the level to be applied to human beings⁸. Figure 2 shows the most popular achievement, the Utah electrode array and its application^{9,10}. As a Brain-Computer Interface (BCI), this device is comprised of more than 100 electrode needles on a chip to record the electrical signals from the motor cortex, and using the recorded signals were able to control a robotic arm. It is the state-of-the-art technology which is able to measure the neuron to neuron signaling in a few micrometer orders. On the other hand, a non-invasive type of devices with much simpler structure triggered the starting of developing a brain-

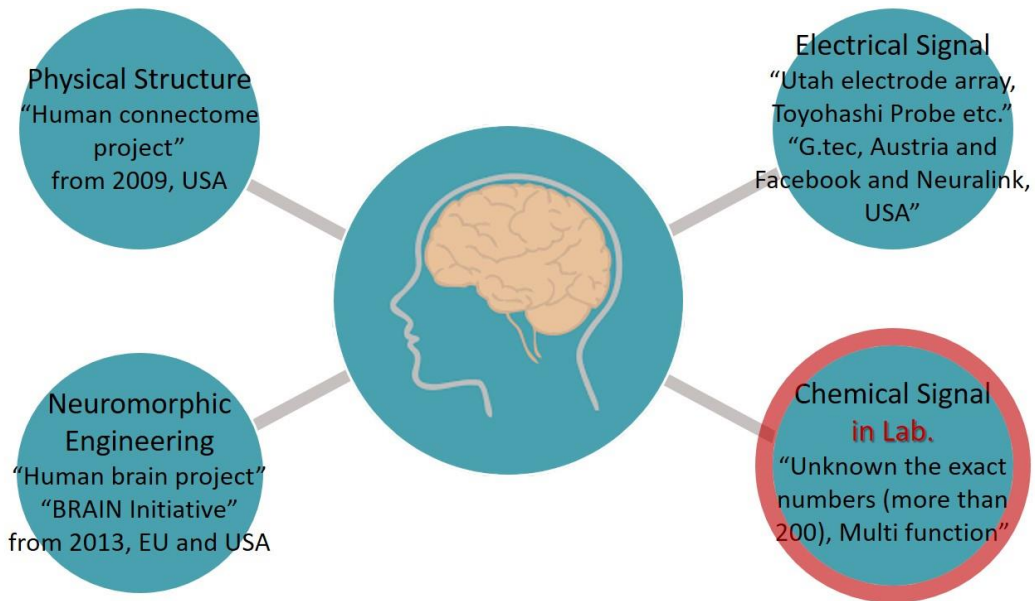


Figure 3 Various approaches to study the human brain in the world.

to-brain (B2B) communication and led startups, such as Neuralink Corp., USA, Facebook, USA and G. Tec Medical Engineering GmbH, Austria, to attempt commercializing. According to these progresses, people are starting to believe that we may solve the mysteries of our brain function and mind, and the demands for studying of chemical signals and developing of analysis equipment are also rapidly growing. Until now the measuring of electrical signals that include the direction and magnitudes of the delivered neural signals have provided us lots of new insights and practical applications, thus it is expected how many possibilities can be created by identifying kinds of chemicals and tracking each pathway. Besides that, there are some state-led projects such as Human Connectome Project of USA since 2009 which aims to build a network map within the human brain, and the Human Brain Project of EU and BRAIN Initiative of USA from 2013 which aim to investigate the brain on different points of view with the support of the development and application of innovative technologies. These brilliant and recent researches to understand the human brain are summarized in figure 3.

1.2 How have we been monitoring chemical signals?

In the human brain, over 85 billion neurons exist and their communication occurs by complicated activities of more than one hundred neurotransmitters coming into chemical synapses¹¹⁻¹³. Even though some neurotransmitters, such as ATP, acetylcholine, dopamine, serotonin, are very familiar to us, their new functions keep being reported according to discoveries of new kinds of neurotransmitter and their mechanisms. These studies and development of medicines require effective analysis equipment to quantify biochemical activities in neuronal communications.

To satisfy the needs, several analytical techniques with different strategies have been developed. However, many of them, such as microelectrodes¹⁴, biosensors¹⁵, liquid chromatography and capillary electrophoresis separations¹⁶, fluorometry and fluorescence microscopy¹⁷, and liquid chromatography and high-resolution mass spectrometry¹⁸, can offer the information on the averaged concentrations of various neurotransmitters in the corresponding areas. In other words, they are not able to provide spatial information that is directly related to understanding the neurotransmission mechanisms due to their theoretical and structural limitation. They can be suitable for simple and rough testing, but not for analyzing requiring high accuracy.

To investigate the multiple neurotransmission, the analysis tools need to have the following qualifications: Imaging ability with high spatio-temporal resolution and multiplex detection ability with good selectivity. Only a few imaging tools based on reflection mechanism of light and electrochemical scanning technology have nearly satisfied the qualifications and some of them have been commercialized. Figure 4 illustrates the system of a scanning electrochemical microscopy, which is one of the tools enabling to image the distribution of various chemicals on the surface¹⁹⁻²¹. However,

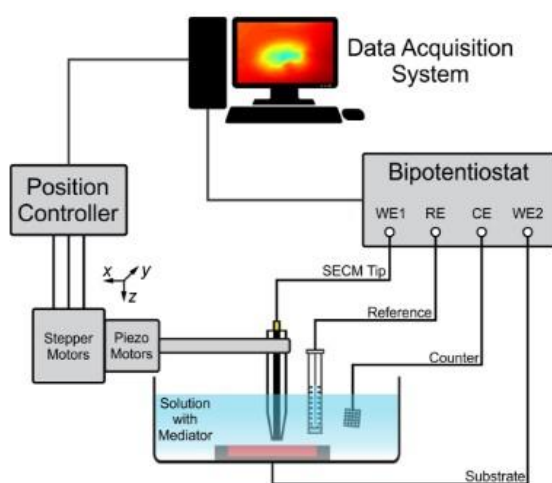


Figure 4 Measurement system of scanning electrochemical microscopy with permission from the publisher^{19,65}.

it not only has the scan rates in the sub-second scale which is limited by the time of scanning pass but also cannot get in-vivo imaging. On the other hand, figure 5 shows multiplex detection images taken by Raman spectroscopy and two-photon fluorescence microscopy²²⁻²⁵. These are the most popular methods that allow imaging of neurotransmitters' activities in high spatial and temporal resolution. They enable noninvasive observation and two photon fluorescence microscopy even produces 3D images. However, in such light-based resolution imaging, there are drawbacks such as the essential use of expensive and huge, precise alignments and lenses and the damage of cells from the light exposure of high-intensity. In addition, to use fluorescence microscopes, pretreatments as the fluorescent labeling biomolecules to the target cells are necessary before carrying out analysis²⁶. In figure 6, we compare the bio-image sensors in my study of the mentioned real-time imaging technologies above. Among the imaging equipment, the bio-image sensor has high portability due to the relatively small size by lacking a filter. Developing smaller-sized devices are important to reduce stress in mice where sensors are implanted in the brain during long-term recording. Most of all, the good portability suggests our sensor being suitable for BCI systems to transfer chemical signals. Furthermore, the bio-image sensor has a big possibility of improving high spatial resolution along with the progress of advanced CMOS technologies.

Required specifications of an analysis tool for monitoring chemical signaling in the brain:

- ① Multi-detection ability (= selectivity)
- ② High spatial resolution (= small pixel pitch and density of an array)
- ③ High imaging speed (= temporal resolution)
- ④ Portability (= filterless and implantation possibility)

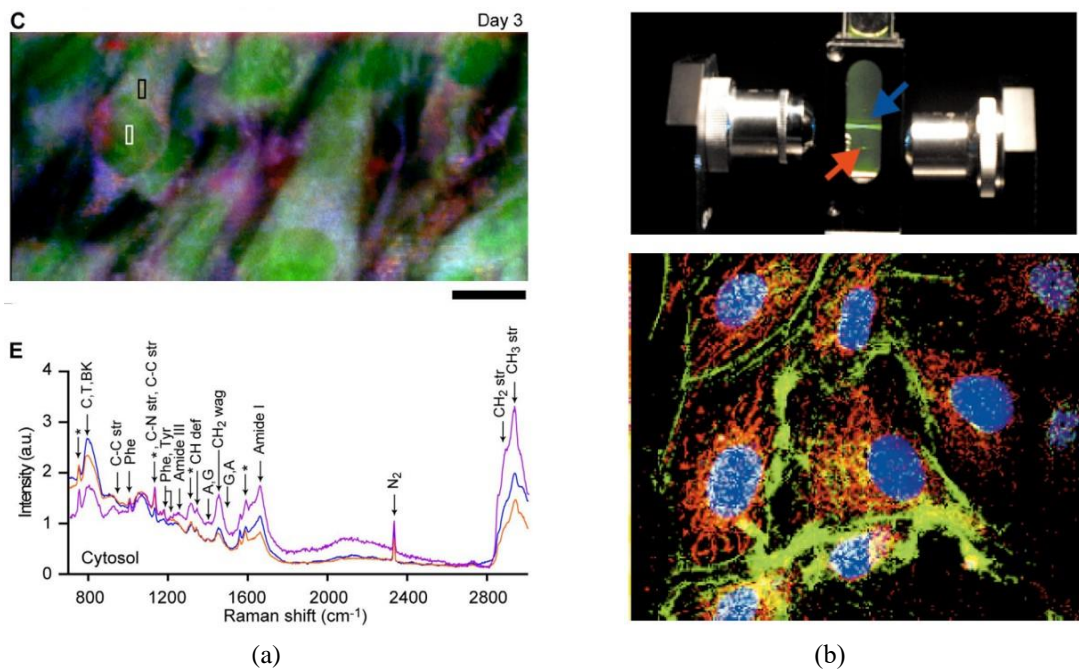


Figure 5 Multiple color imaging of various biomoleculars taken by (a) raman spectroscopy and (b) two-photon fluorescence microscopy with permission from the publisher^{22,23}.

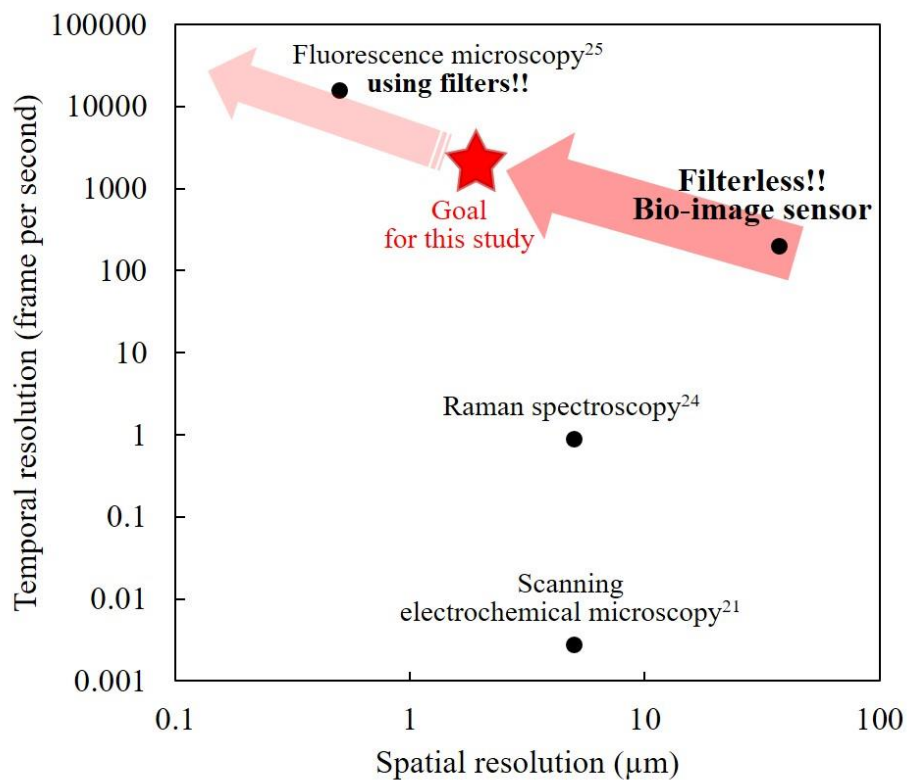


Figure 6 The reported real-time 2D imaging technologies for detecting multi-biomarkers are compared with our bio-image sensor.

1.3 Can we provide a better tool?

Then how can we get the advanced tool that enables to monitor and image spatiotemporal activities of various neurotransmitters at the same time? This thesis will suggest one possible idea to come true. We are going to combine two different engineering fields of biochemical and semiconductor techniques for developing a bio-image sensor.

This thesis consists of three main parts:

- First, we develop new enzyme-immobilization technique using conventional photolithography²⁷.
- We then apply this technique to pH image sensor based on a charge coupled device technology to develop bio-image sensor that enables to monitor spatiotemporal activity of various neurotransmitters in same time.
- Additionally, we upgrade the platform specification of pH image sensor to perform with higher spatial and temporal resolution³⁰.

1.4 Outline

Chapter 2 will provide a theoretical background how pH image sensor operates. **Chapter 3** is about the proposed enzyme-immobilization technique; how enzymatic reactions can identify the kinds of neurotransmitter and transfer their information into pH change, how enzyme can be locally immobilized on pH image sensor. **Chapter 4** shows the firstly developed ATP and hydrogen ion image sensor applied the immobilization technique and its device characteristics. **Chapter 5** is about the advanced bio-image sensor to monitor multi-neurotransmitters and how can enhance its discriminability. And it will be discussed why the molecular diffusion is problematic in biological measurement using bio-image sensor and how it can be decreased to improve sensor's sensitivity and spatial resolution. **Chapter 6** is regarded upgrading of pH image sensor which is used as a platform of the bio - image sensor. In order to improve device performances, in-pixel and readout circuits are redesigned and fabricated. And the enhanced sensor is demonstrated by our new evaluation method to confirm its practical spatial resolution.

Theories

To study biological changes in neural networks, electrochemical strategies, such as an ion sensitive field effect transistor (ISFET), have been developed to transduce biochemical information from cells to artificial systems^{31–33}. One of the key benefits in ISFET is that the gate can be modified with specific biological elements such as enzymes, antibodies, ion-selective polymer and nucleic acids^{34–38}. These potential advantages of monitoring multiplex interactions among various analyte samples are promising multiple variations of biosensing platforms. We have been developing an ISFET array which can image and record the spatial concentration gradient of multiple metabolites and that includes CMOS and charge coupled device (CCD) imaging techniques that are widely used for digital cameras^{39–46}. Therefore, a pH image sensor is a biosensing platform consisting of an ISFET array and a readout integrated circuit. In this chapter, we introduce the fundamentals of the bio image sensor and their theoretical limitations of sensing capability.

2.1. The ISFET

The ISFET is a chemical sensor. The most basic structure of ISFETs is a metal oxide semiconductor FET (MOSFET) using the modified gate which has an ion-sensitive membrane on the gate oxide and requires a reference electrode to operate in solution. The basic structure of the ISFET used for our pH image sensor is similar to a n-type MOSFET (NMOS). Figure 7 compared to the common structure of a NMOS and ISFET³³. The transistor should have four terminals: a source, drain, gate and bulk. In the case of NMOS, N-type dopant is diffused into a p-type substrate to generate the source and gate. The channel is formed beneath the gate, and through the channel the carriers flow out of the source and come into the drain. The resistance of the channel is controlled by the gate-to-source voltage (V_{GS}). The generated electric field by the applied gate voltage can control to accumulate the amount of charges in the channels. The minimum V_{GS} that is needed to create a conducting channel between the source and drain is called as the threshold voltage (V_{th}). Then, how operates the ISFET? To measure the pH change, the poly silicon on gate oxide is replaced with a reference electrode, a conductive liquid and an ion-sensitive membrane. Because the molecules in electrolyte generate an electric field

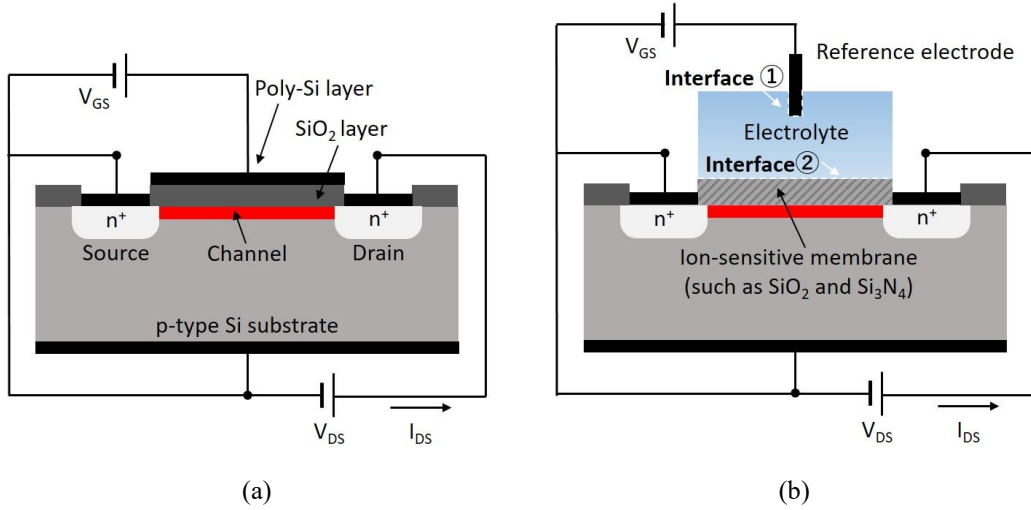


Figure 7 Cross-sectional view of (a) a NMOS and (b) a ISFET.

on the gate according to the applied V_{GS} , we can apply the general equations of NMOS to define the source-to-drain current (I_{DS}) of ISFET as below^{33,47}:

$$I_{DS} = \mu C_{ox} \frac{1}{2} \frac{W}{L} (V_{GS} - V_{th})^2 \quad \text{In saturation region } (V_{DS} \geq V_{GS} - V_{th}) \quad (1)$$

$$I_{DS} = \mu C_{ox} \frac{W}{L} \left[(V_{GS} - V_{th}) V_{DS} - \frac{1}{2} V_{DS}^2 \right] \quad \text{at triode region } (V_{DS} < V_{GS} - V_{th}) \quad (2)$$

$$V_{th} = V_{ref} + V_{chem} \quad (3)$$

where V_{chem} is a chemical potential at the gate surface and the general expression for the I_D of ISFETs in the unsaturated region can be rearranged as below,

$$I_{DS} = \mu C_{ox} \frac{W}{L} \left\{ [V_{GS} - (V_{ref} - V_{chem})] V_{DS} - \frac{1}{2} V_{DS}^2 \right\} \quad (4)$$

2.2. Electrolyte-Solid interface

To convert between electrical and chemical potentials, there are two electrolyte-solid interfaces in the ISFET structure. This section explains the roles of the interface ① and ② in figure 7 (b) that are very important for conversion between the electrical and chemical potentials.

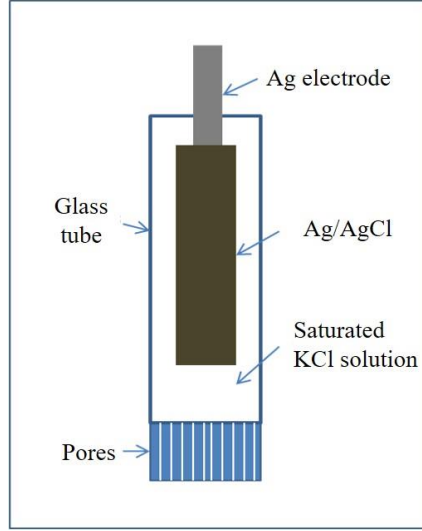


Figure 8 An Ag/AgCl reference electrode.

2.2.1. Reference electrode

Interface ① in figure 7 was formed between the electrolyte and a reference electrode which has a stable and well-known electrode potential. Ag/AgCl glass reference electrode in figure 8 was used for our sensor to allow to maintain a constant potential in solution. This potential value of the reference electrode is independent of a pH change in the solution. Cl^- ions moves via voids of the glass bottom between the KCl solution in the glass reference electrode and electrolyte until the potentials of them are in equilibrium. The surface of Ag/AgCl redox electrode can be in equilibrium by the following the half-reactions:



This reaction is as fast as a sufficiently high current can be passed through the electrode with almost perfect efficiency. The proved dynamic region of pH is between 0 and 13.5.

The potential E_{ref} of the Ag/AgCl electrode can be calculated by the Nernst equation as follows:

$$V_{ref} = E^0 - 2.3 \frac{kT}{q} \log_{10}(\alpha_{Cl^-}) \quad (6)$$

where k the Boltzmann constant, T the temperature and α_{Cl^-} the effective concentration of chloride ions, E^0 the standard electrode potential against standard hydrogen electrode. The electrode potential change is only related to the concentration of chloride ions. Therefore, a saturated KCl solution having high concentration of chloride ions is commonly used to keep the potential drop constant. The use of this glass-bodied reference electrode has been an obstacle to minimize and implant of ISFET based sensors. Even though there are many attempts to scale down or develop solid state reference electrodes^{48,49}, their implantation in brain still remains one of the big challenges.

2.2.2. EDL at the gate surface

Interface ② has the electrical double layer (EDL) structure formed on a gate surface that is connected with an electrolyte. And Gouy-Chapman-Stern theory is described the potential and charge distribution in EDLs⁴⁷. Because the interface is hydrated by chemical interactions and combined ions, the surface is charged and this region is called as the first layer. The second layer is composed of ions attracted to the surface charge in Coulomb force. The movement and diffusion of ions in the second layer are relatively easier than that in the first layer, but difficult to move than that of free ions in the bulk solution that is distanced sufficiently and not effected by electrical attraction. The layer is thus named the diffuse layer. According to the Nernst equation, the charge caused by pH change in the bulk solution can be expressed for the sensitivity (S):

$$S = -2.3 \frac{kT}{q} \log_{10}(\alpha_{H^+}) \quad (7)$$

here, α_{H^+} is the proton (H^+) activities and $pH = \log_{10}(\alpha_{H^+})$. The theoretical maximum of the sensitivity is about 59.2 mV/pH at 25 °C. The sensitivity depends on the material of ion-sensitive membrane and increased in order of $SiO_2 < Si_3N_4 < Al_2O_3 < Ta_2O_5$ ⁵⁰.

Because our pH image sensor has a Si_3N_4 gate, the further explanation of the surface reaction mechanism focus of a silicon nitride (Si_3N_4) film. However, the top thin layer of the membrane surface converted to SiO_2 by the local oxidation of silicon (LOCOS) process⁵¹ and this model, thus, can be approximately described by the pH sensing mechanism of oxide gate ISFETs. The general site-binding model that explains the multisite proton adsorption at solid-solution interface introduced by Hiemstra et al. 1989⁵². This model describes the changing of a silicon oxide as the result of an equilibrium between the surface sight and the H^+ ions in the bulk solution. The charge caused by the surface bonding of gate oxide is directly related to the sensitivity of the electrostatic potential difference to the bulk pH change. Their relationship is expressed the shifted threshold voltage of ISFETs as shown in figure 9⁵³.

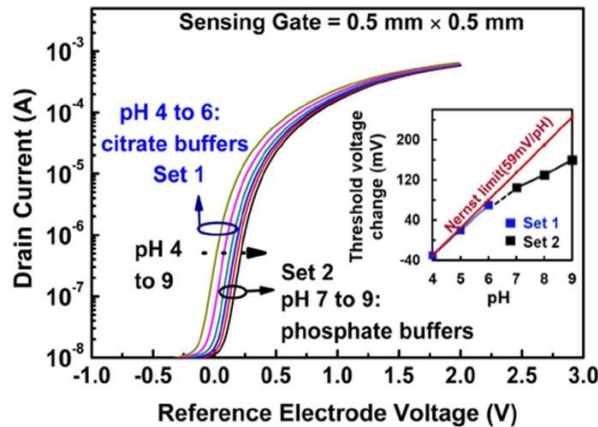
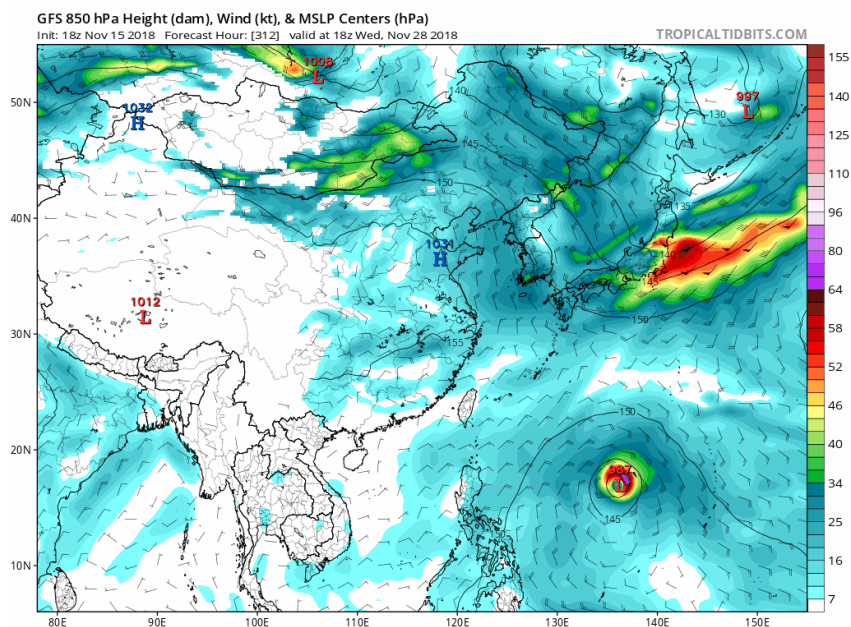


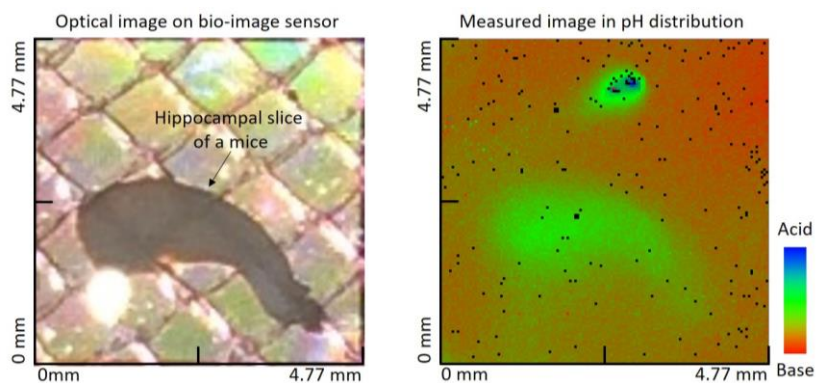
Figure 9 Threshold voltage, V_{th} shifting in I_{DS} - V_{ref} characteristics according to pH changes that is measured by Al_2O_3 -gate ISFETs with permission from the publisher⁵³.

2.3. Imaging of pH distribution in real-time

Now, we know the pH sensing principle of a single ISFET that detect the pH change and quantities H^+ ions. However, it is also necessary to obtain spatial and temporal information about the activity of neurotransmitters for the analysis of neuronal signaling pathways. You may wonder why we want to get the spatial and temporal information of pH and other biomolecules distribution in neural network. The idea to image pH distribution is similar to a weather map to present local differences of atmospheric pressure on a geometry map, as shown figure 10. Today we can understand and predict our weather condition based on this imaging technique and the long-term observed data. Likewise, because local pH changes in the brain are biomarkers of neural activity to follow metabolic processes⁵⁴, it is very important to monitor their locations of pH changes for understanding our neural network function. Like the multiple analysis techniques of air pressure, temperature, humidity, wind speed, etc.



(a)



(b)

Figure 10 (a) Weather map at Nov 15, 2018 referred to TROPICALTIDBITS.COM. The color chart presents the pressure (hPa). (b) The optical and measured images of a hippocampal slice on our bio-image sensor.

made possible the elaborate weather forecasting, we are expecting that the multi-detection technique of different neurotransmission, which is the goal of this thesis provides a new approach in the neuroscience. This section introduces how our bio-image sensor satisfies these spatial and temporal requirements.

2.3.1. pH image sensor

To capture the neuronal phenomena from the electrophysiological activity of neurons, high-density (HD) microelectrode arrays (MEAs) including the Utah array have been developed. MEAs have been focused to⁵⁵⁻⁵⁸. Similar to this concept, many studies integrated a group of ISFETs with peripheral circuits on a chip to achieve spatial and temporal resolution of pH changes^{44,59-62}. Most of the fabrication process of ISFET array is based on a complementary metal oxide semiconductor (CMOS) technology. A size of an ISFET, thus, can be going to scale down according to the progress of CMOS techniques. It is one of the biggest advantage, because the miniaturized array size and sensor pitch are required to capture the activities of co-released neurotransmitters and cell metabolisms on a subcellular level⁶³. Each ISFET in an array is working as a pixel to detect pH change and the integrated peripheral readout circuits conveys the information used to make an image. Using the charged coupled device (CCD) readout technique, the images can be outputted serially. We named the device, pH image sensor.

2.3.2. CCD technology for the pH-image sensor

To be specific, the peripheral readout circuits exist to realize a CCD technology, which can visualize the spatial and quantitative information measured by the ISFET array in real-time. This imaging technology is commonly used for a digital camera from 1970³⁹. The proposed pH image sensor in this thesis is rather like an active pixel sensor (APS) with the intra pixel charge transfer. The advantage of the APS architecture is that it can be fabricated in large and dense arrays and is highly compatible with advanced CMOS device processes⁴⁴. In order to detect the pH change, ISFET is inserted as an active transistor within each pixel. In this section, we introduce the physics of the operation of a bio-image sensor based the CCD technology.

As discussed in section 2, the pH changes in bulk solution not only lead to different potential gradients at the interface of the gate oxide/substrate, but also changes the potential beneath the ion-sensitive gate. The overall potential drops from a reference electrode into a semiconductor. Under the region covered with ion-sensitive membrane, a potential well forms in which the depth is changed by pH variation in the solution. Then, a CCD register consisting of a series of gates transfers the stored electrons in the potential well to an external device (PC). A measurement software installed on a PC automatically transforms the data into two dimensional (2D) image.

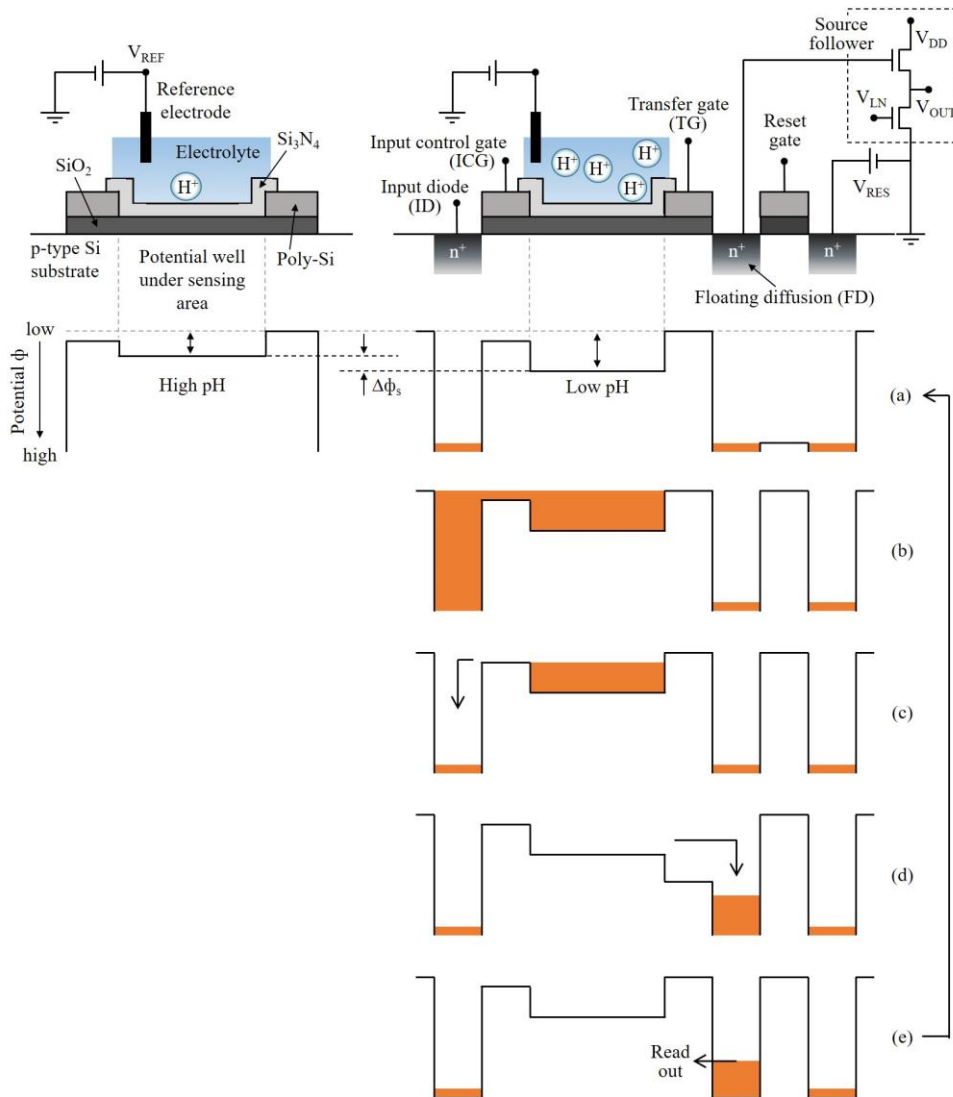


Figure 11 The operational procedure for the principle of a pixel based on CCD imaging technology in high and low pH solutions.

Their detail working principle of a pixel is described in figure 11 and below:

- (a) To initiate a pixel before a measurement, the potential (ϕ) of an input diode (ID) is decreased.
- (b) The potential of the ID is briefly pulsed from high to low.
- (c) By repulsing the potential of ID is stable at high, the charge in the potential well under the sensing area is remained depending on the well depth.
- (d) A transfer gate (TG) is turned on and transfers the stored charge to a floating diffusion (FD).
- (e) The potential value at the FD is read out by a source follower circuit, and return to (a) to start a new cycle. The procedure from the scheme (a) to (e) is one cycle.

Next, the electronic signals measured at each pixel are read out very rapidly as pH value corresponding image location. The image is reconstructed and displayed on a computer monitor instantaneously.

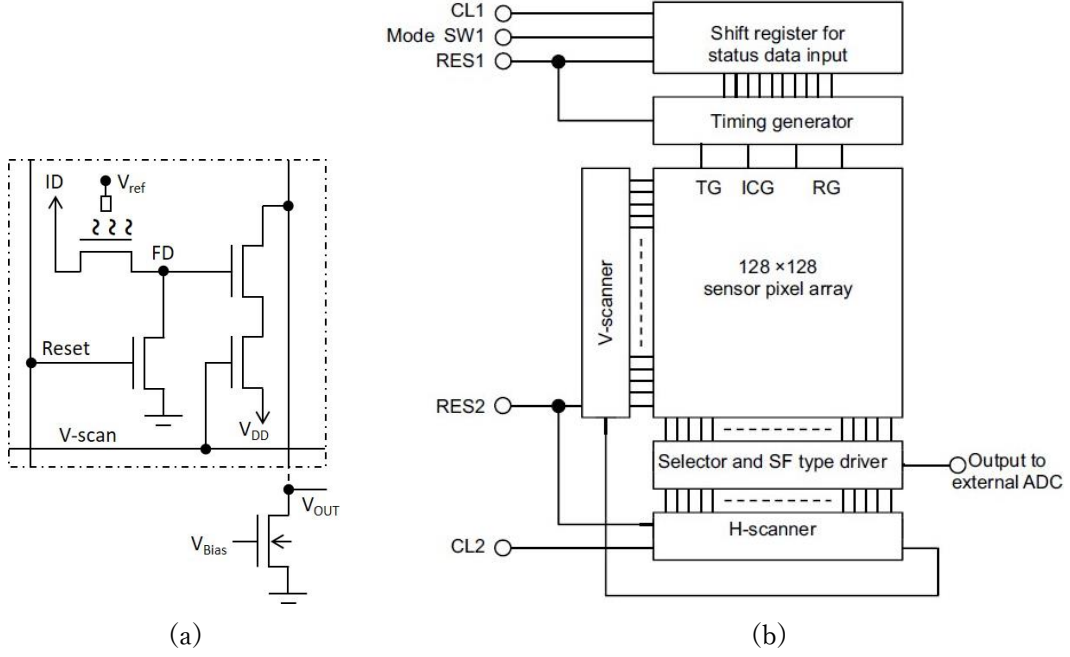


Figure 12 (a) Analog front end topology for single pixel readout with four transistors and (b) sensor readout circuits schematic with permission from the publisher⁶⁴.

Figure 12 present a topology of a single pixel and system block of our pH image sensor that were suggested in our previous work⁶⁴. 128x128 pixels are arranged in a two-dimensional grid with readout circuitry integrated to efficiently measure the full array. The integrated peripheral circuit consists of a timing generator, a shift resistor and both vertical and horizontal scanners. In full-frame CCD operation, the accumulated charge in each pixel is shifted by vertical and horizontal scanners and then transferred to output sequentially. All of the transistor on-off timing is controlled by the timing generator.

As indicated in the sensor architecture, the V_{OUT} is the measured result including attenuation by the readout circuit. Therefore, a sensor's gain (g) which can be achieved by measuring a ratio between input and output voltages is

$$g = \frac{\Delta V_{OUT}}{\Delta V_{ref}} \quad (8)$$

Moreover, the equation of a measured sensor sensitivity (S_{sen}) measured by using various standard pH solutions is defined as

$$S_{sen} = \frac{\Delta V_{OUT}}{\Delta pH} \quad (9)$$

Combination of the equation (8) and (9) leads to the expression for the sensitivity of the reference voltage difference to the bulk pH change:

$$\frac{S_{sen}}{g} = \frac{\Delta V_{OUT}}{\Delta pH} \times \frac{\Delta V_{ref}}{\Delta V_{OUT}} = \frac{\Delta V_{ref}}{\Delta pH} \quad (10)$$

Combination of this expression with equation (3) yields:

$$\frac{\Delta V_{ref}}{\Delta pH} = \frac{\Delta(V_{th} - V_{chem})}{\Delta pH} \quad (11)$$

So that the equation (9) and (10) can be simplified to:

$$\frac{S_{sen}}{g} = \frac{\Delta V_{ref}}{\Delta pH} = S \quad (12)$$

S is the sensitivity of the electrostatic potential difference to the bulk pH change. The gain is previously acquired before starting a measurement. All of the output data ($V_{OUT, G}$) in this thesis are compensated by the measured gain.

2.4. Bio-image sensors for multiplex detection

As well as real-time imaging capability, an ability to identify biological specimens is very important for neuronal diagnostics. There are electrochemical imaging techniques which can satisfy the conditions. The imaging techniques can be categorized into two groups: Scanners and MEA system. Electrochemical scanners, such as fast-scan cyclic Voltammetry (FSCV)^{65–68} and scanning electrochemical microscopy (SECM)^{19,69,70}, have emerged as powerful imaging platforms. FSCV-based detection, where a triangular wave is applied to electrodes to measure unique cyclic voltammograms, have allowed high selectivity by the repetitive redox reaction on the electrode surface at high scan (up to 100 V/s). In case of SECM based on a scanning probe microscopy (SPM) technique using tip electrodes as scanning probes, it is already commercialized and commonly used for in vitro measurement. These methods are effective for investigating the spatial distribution and for quantitatively analyzing various materials near the region of steady-state diffusion. However, the temporal resolution is limited by the time of one complete scanning pass of all lines in the measuring area. Various large-scale integration (LSI) -based chip containing amperometric or potentiometric MEAs have been developed to record neuronal activities in temporal and spatial scales at sub-cellular resolution⁷¹. However, almost all HD MEAs are focused to capture the neuronal phenomena from the electrophysiological activity of neurons^{55–58}. Few MEAs for simultaneous detection of different biochemical elements have been demonstrated with low spatial resolution, due to the difficulty of optimizing the potentials applied to each electrode⁷². Miniaturized array size and electrode spacing are required to capture the activities of neurotransmitters and cell metabolisms on a subcellular level⁶³.

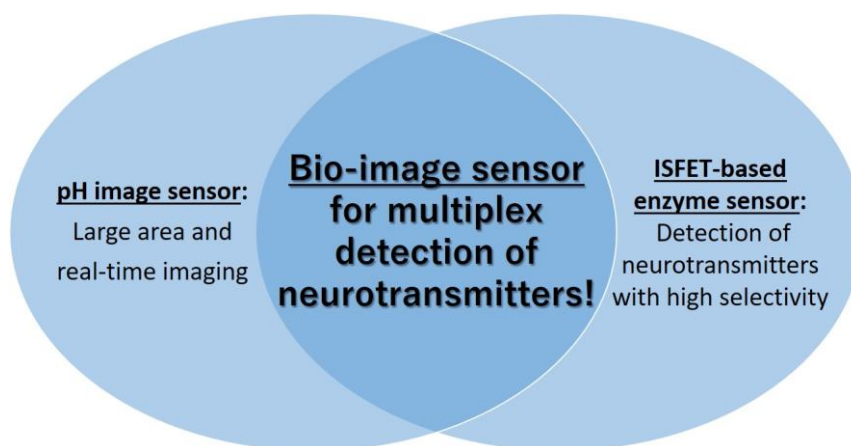


Figure 13 Concept of our bio-image sensor proposed in this thesis.

To overcome all the obstacles, we propose a new approach in this thesis. In brief, our bio-image sensor is the results of the integration of pH-image sensor and ISFET-based enzyme sensor as the concept depicted in figure 13. To develop a prototype sensor, we aim to detect both adenosine 5'-triphosphate (ATP) and acetylcholine (ACh) that are well-known neurotransmitters that have been identified ⁷³⁻⁸¹. In addition, corelease involved ATP and ACh from a mammalian motor nerve was first demonstrated using electrophysiological techniques combined with the firefly luciferase assay ⁸². While the related functional roles of ATP and ACh have been widely recognized ⁸³⁻⁸⁵, their signaling is still recorded by simple tools, such as a glass microelectrode filled with 3 M KCl, a patch clamp using borosilicate glass and a biosensor consisting of a series of enzyme-based microelectrodes ⁸⁶⁻⁸⁸.

To provide our bio-image sensor as a platform for monitoring of the activity of ATP and ACh, we use enzymatic reactions that can generate H⁺ as by-products. Apyrase and acetylcholinesterase (AChE) catalyze the breakdown of ATP and ACh respectively into the smaller molecule and acids, on the following reactions ^{89,90}:



and



If the enzymatic reaction occurs on the gate surface of an ISFET, the generated amount of H⁺ will be detected by the sensor. To apply this enzymatic reaction technique to a pH image sensor, it is necessary to localize enzymes on each pixel separately and elaborately. The immobilization technique of enzymes is described in the following sections.

Experimental methods and materials

3.1 Preparing pH image sensor

The used pH image sensor (version of pHP0128) is shown in figure 14 with the corresponding pixel placement of in the array. The fabrication of this sensor was developed using a CMOS process by our laboratory⁹¹ and outsourced to LAPIS Semiconductor Co., Ltd. The size of a single pixel is $37.30 \mu\text{m} \times 37.30 \mu\text{m}$, and 128×128 pixels are arrayed on a chip. The frame speed of the images is 30 frame/s. Before starting a measurement, the surface of sensor chips is rinsed in Milli-Q water (double distilled water) at $80 \text{ }^\circ\text{C}$ for 30 minutes.

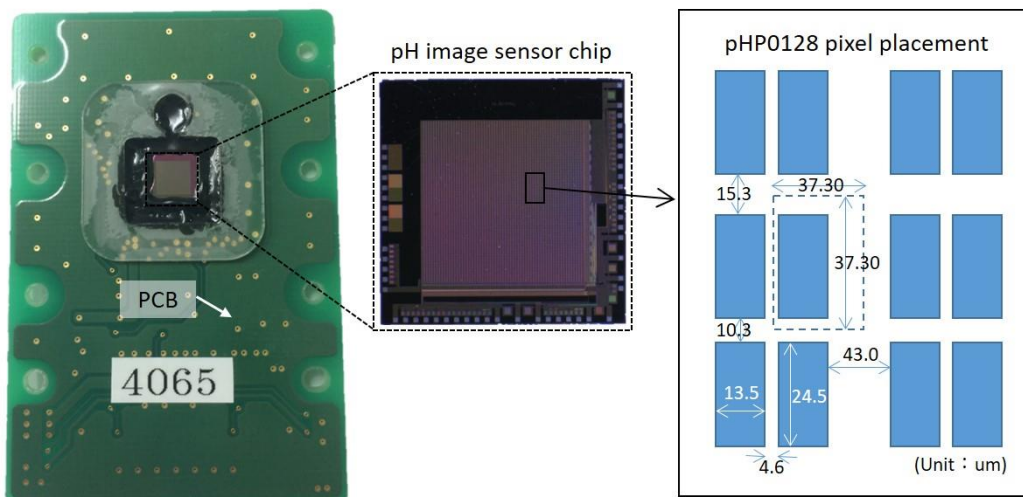


Figure 14 A photo of a pH image sensor and a schematic diagram of partial pixel placement.

3.2 Measurement setup

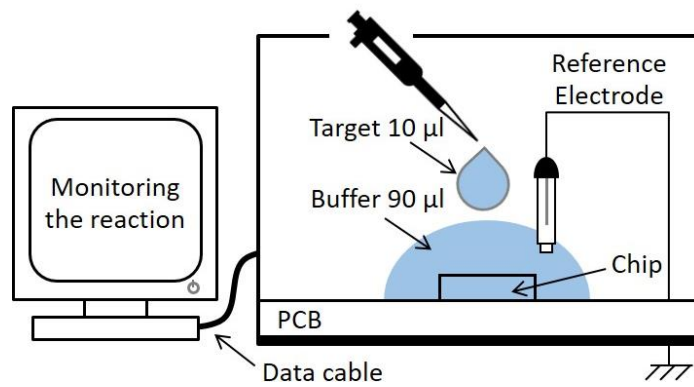
Sensors can be calibrated with the standard solutions of pH 4.01, 6.86 and 9.18 (Wako Pure Chemical Co.), and pH changes of solution mixtures are checked with a standard pH/ion meter (LAQUA F-72, HORIBA, Ltd.).

For measurement of neurotransmitters, we use an artificial cerebrospinal fluid (aCSF) buffer solution which is an electrolyte consisting of 135 mM NaCl, 5 mM KCl, 2 mM CaCl₂, 1 mM MgCl₂, 10 mM D-glucose, 1 mM HEPES-NaOH (pH7.4) and Milli-Q water. The buffer solution resists a variation in pH and could adjust the osmolality between a solution and a cell. Three kinds of the targeted elements, such as ATP (Adenosine 5'-triphosphate sodium salt *n*-hydrate, Wako Pure Chemicals, Osaka, Japan), ACh (Acetylcholine chloride, Sigma-Aldrich Co., MO, USA), and a mixture of ATP and ACh, are prepared at concentrations from 0.1 mM to 25 mM. The components of buffer and electrolyte listed in table 1. The final concentrations of the 10-fold dilution are 0.01, 0.1, 0.25, 0.5, 0.75, 1, and 2.5 mM. ATP and ACh are solved in the aCSF to make ATP, ACh and the mixture of ATP and ACh.

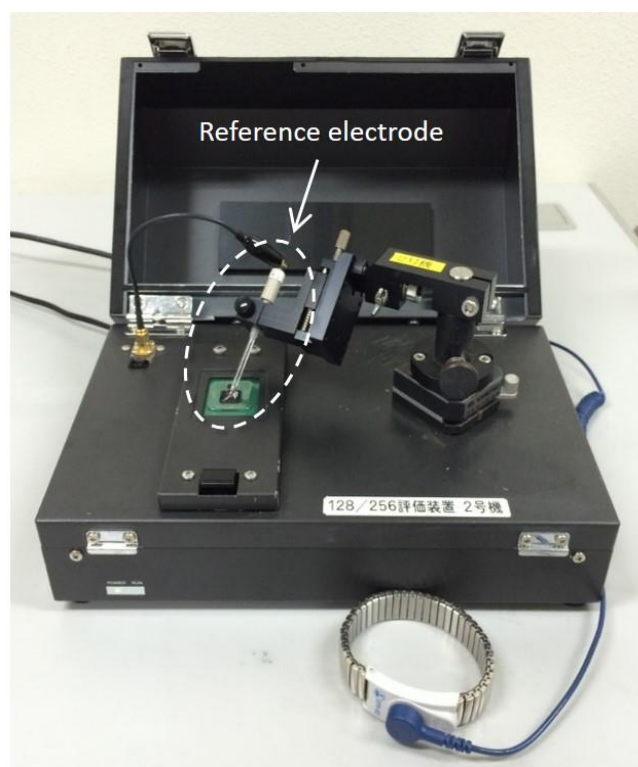
Table 1 Solution components.

Solution	Component	Concentration
Buffer (pH 7.4)	NaCl	135 mM
	KCl	5 mM
	CaCl ₂	2 mM
	MgCl ₂	1 mM
	D-glucose	10 mM
	HEPES-NaOH	1 mM
	Milli-Q water	-
Targeted analyte mixed buffer (pH 7.4)	ATP	0.1 - 25 mM
	ACh	
	ATP + ACh	

The measurement setup is shown in figure 15. The entire pixel array is immersed in 90 µl of the buffer solution. Then, to obtain a homogeneous enzymatic reaction from the entire area, a 10 µl droplet of a targeted element is thoroughly mixed into the buffer solution with a pipette, or some potassium hydrogen phthalate (C₆H₄ (COOK) (COOH), Wako Pure Chemical Co.) is dropped into. Measuring software installed on a PC automatically transforms the measured data into their output images. The used Ag/AgCl reference electrode (EC Frontier Co., Ltd.) saturated with 3 M KCl.



(a)



(b)

Figure 15 (a) A schematic diagram and (b) an optical photo of experimental setup.

3.3 Patterning enzyme-immobilized membrane

To immobilize different enzymes on the pH image sensor, a photolithography technique is used as shown in figure 16⁹². Enzymes are stuck among the linked polymer structure after UV exposure. The detail information concerning the fabrication follows. Firstly, a spin-coater (MS-A100, Mikasa.Co., LTD, Tokyo, Japan.) is used to deposit different enzymes mixed with the cross-linking polymer (BIOSIRFINE®-AWP, Toyo Cosei Co., Tokyo, Japan) with a pH image sensor. This cross-linking polymer is attractive due to the biological stability and porous chemical structure binding⁹³. Next, enzymes are immobilized by a mask aligner (MA6 BSA, SUSS Micro Tec., Garching, Germany). Apyrase (EC 3.6.1.5, Sigma-Aldrich Co., MO, USA) and AChE (EC 3.1.1.7, Sigma-Aldrich Co., MO, USA) in powder are used for enzymatic reactions. Apyrase of 1.6 U/ μ l and AChE of 10 U/ μ l mixed with Milli-Q water are prepared for fabricating of a bio-image sensor prototype. The thickness of the deposited membranes is measured by Microfigure measuring Instrument (ET 4000A; Kosaka Laboratory Ltd., Tokyo, Japan).

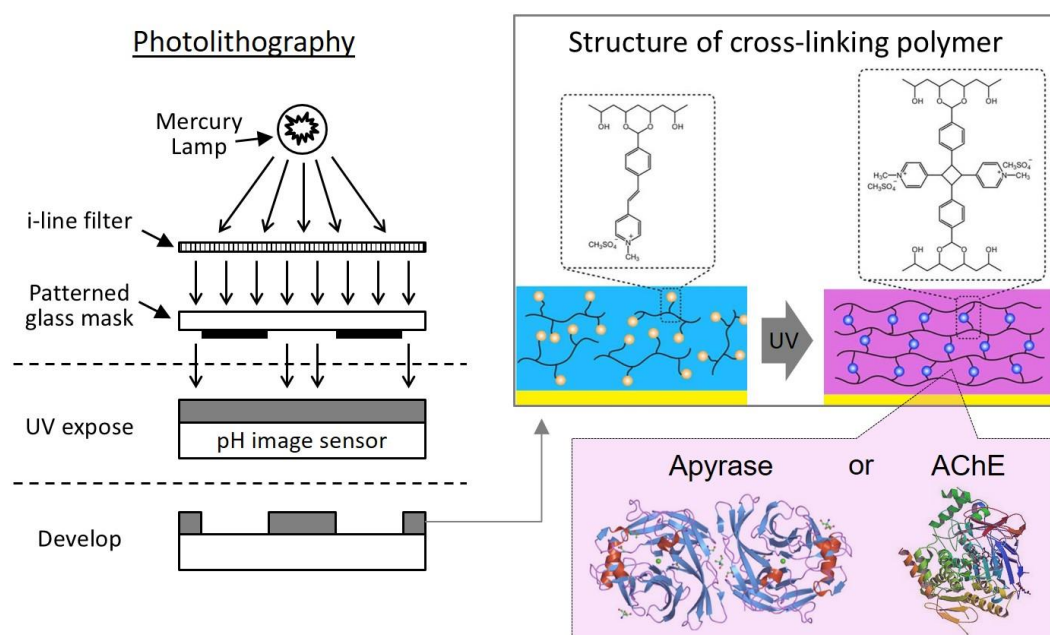


Figure 16 A schematic diagram of enzyme-immobilization on a cross-linked polymer by photolithography. The image of cross-linking polymer structure reproduced from Bai et al.⁹² with permission of its publisher.

3.4 Preventive measures against H⁺ diffusion

3.4.1 Barrier layers

Porous layers made from the cross-linking polymer are placed on the enzyme-immobilized image sensor. A single layer is deposited on the whole sensing area of a bio-image sensor by a spin-coater and then cured by handy type UV lamp (356 nm, LUV-4, As One, Osaka, Japan). The cross - linking polymer is diluted with Milli-Q water to reduce the viscosity.

3.4.2 Microhole array

The proposed microhole array is constructed by a negative photosensitive material SU-8 (SU-8 3000, Nippon Kayaku, Tokyo, Japan) that has a good biocompatibility⁹⁴ and a mask aligner. The surface of the fabricated structure is treated to obtain the hydrophilic property by UV ozone cleaner (UV-1, Samco., Japan). The developer is 1-methoxy-2-propanol acetate. Before testing the H⁺ diffusion preventing capability, AChE is immobilized with magnetic beads (Biotin Labeling Kit-NH₂, Dojindo, Japan) and locally placed on the sensor fabricated with the microhole array.

Enzyme immobilization technique

To achieve a multiplex detection capability based on a pH image sensor, we developed a new process based on photolithography that can immobilize a variety of enzyme-containing polymer patterns on a chip. This chapter will mainly discuss how the enzyme immobilization technique has developed and optimized to fabricate a bio-image sensor, and what kind of parameters determine the sensor performance, such as sensitivity, limit of detection (LOD) and measuring time. This study was published by Lee et al.²⁷

4.1 Patterned enzyme-immobilized membranes

Along with the development of enzyme-based biosensors as a combination of the high specificity of enzymes with a good sensitivity of electrochemical transducers, there are many studies in enzyme immobilization such as adsorption, covalent coupling entrapment, cross-linking and affinity bonds. However, it is still very difficult to immobilize desired enzymes into a small and a particular shape on a semiconductor device. Even though an immobilization method using lift-off technique, that was attempted by Nakamoto et al. in 1988⁹⁶, was able to immobilize glucose oxidase and urease at specific area on a single chip, this sensor could not provide a geometrical information and a good sensitivity about the targeted neurotransmitters due to technical limitations. We thought the low sensitivity of the glucose and urea sensor is the results of the loss of enzyme activities caused by the heating process and low biocompatibility of the used materials.

Therefore, we have developed an enzyme immobilization technique which is the modified photolithography technique having high compatibility with biological materials without any reaction loss. In addition, the advantages of this method is that large-area and high-density geometric enzyme patterns can be constructed on a semiconductor device. Cross-linkable polymer as a photoresist is used for building intra porous structures by UV exposure of photolithography technology. Enzymes are fixed among the structures. The detailed fabrication process and optimization are given in the next section.

4.2 Fabrication

The enzyme immobilization technique is described in figure 17. Firstly, 50 μl of a mixture of enzyme and UV sensitive cross-linking polymer is spin-coated. The mix ratio for enzyme and cross-linked polymer is one to four (1:4). After drying at room temperature during approximately 10 minutes, a photolithography method is used to transfer patterns from a photomask to the deposited mixture layer. Here, the enzyme-immobilized pattern accurately corresponds to the designed pattern shape on the photomask. Excepting the exposed region where enzyme is entrapped in their cross-linked polymer matrices, the uncured mixture of the other regions is removed by Milli-Q water. These three processes (a) - (c) can be repeated to immobilize other kind of enzymes.

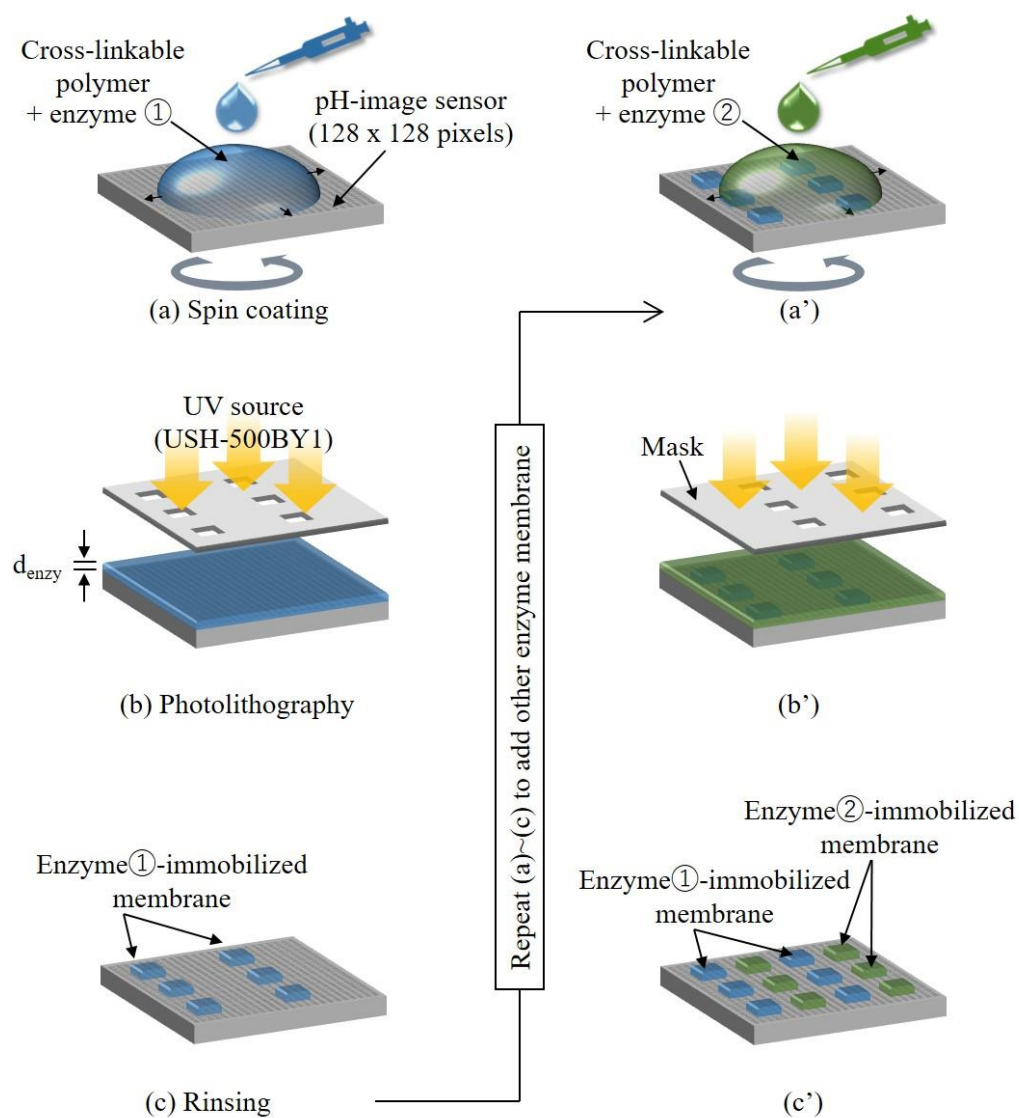


Figure 17 The fabrication process for immobilizing and patterning of different enzymes on a pH image sensor. AChE and apyrase are attempted in our study.

4.3 Optimization - ATP and H⁺ image sensor

Before fabricating the bio-image sensor for measuring ATP, ACh and H⁺ simultaneously, the enzyme immobilization technique was optimized. ATP and H⁺ image sensors were fabricated with the non-patterned apyrase-immobilized membrane. The membrane thicknesses and UV light power for photolithography are tested to find appropriate values that can output a maximized sensitivity.

4.3.1 The patterned enzyme-immobilized membrane

To evaluate the membrane thickness, cross-linkable polymer containing apyrase was immobilized without patterns on the top of a pH image sensor by a UV exposure of 1000 mJ/cm². The membrane thickness was controlled by the speed of a spin coater and measured by Microfigure measuring Instrument. In figure 18 shown the time dependent output voltage was obtained at a single pixel (80, 80) in the range of various ATP concentrations.

Because it takes time until the output signal is saturated after injecting ATP due to the kinetics of the enzymatic reaction, the output voltage differences ($\Delta V_{OUT,G}$) that is compensated by the gain is obtained the difference between the initial output signal and the saturated output signal measured at 160 s after injecting ATP. The response is the average of the output voltage differences of the measured pixels, which is defined as:

$$\text{Response} = \frac{\sum_{j=1}^n (V_{j,saturated} - V_{j,initial})}{n} = \frac{\sum_{j=1}^n (\Delta V_{j,OUT,G})}{n} \quad (15)$$

where n is the number of the pixels, $V_{j,initial}$ the initial output voltage and $V_{j,saturated}$ the saturated output voltage.

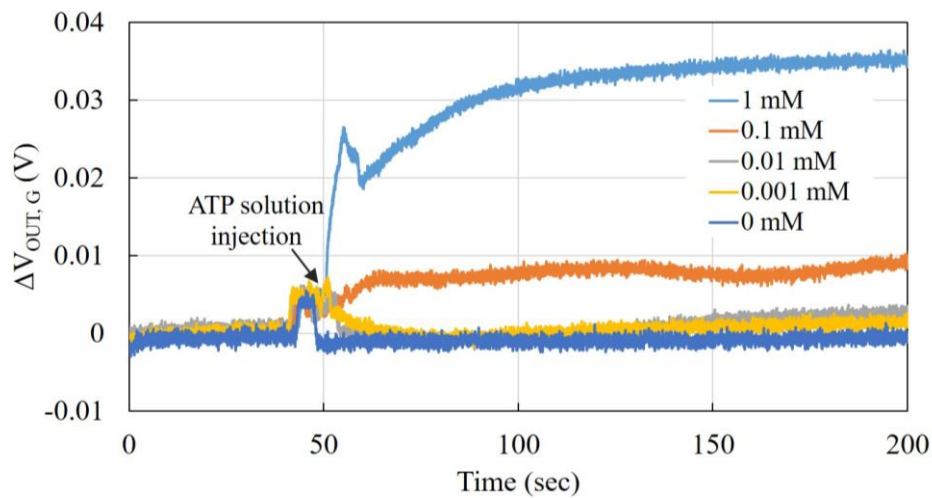


Figure 18 Time dependent output voltage in respect to ATP concentration measured from the pixel at (80,80).

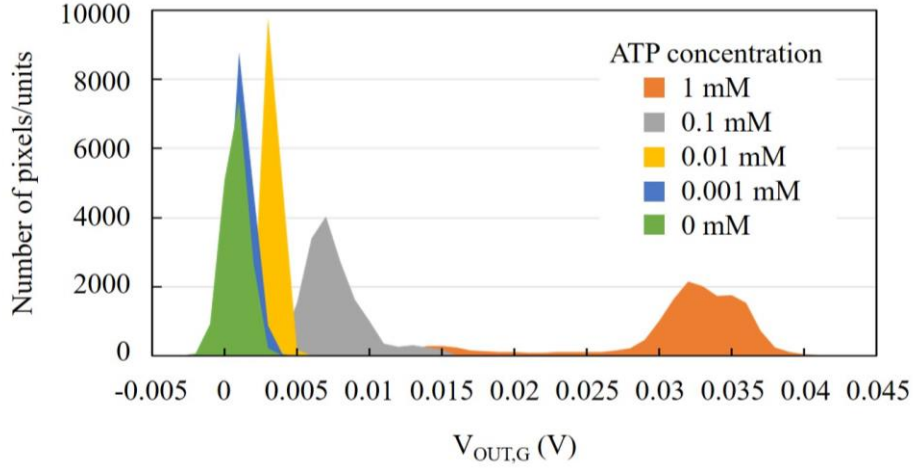


Figure 19 Histogram of the output voltage distribution measured from all pixels.

Their histograms in figure 19 represent the $V_{OUT,G}$ distribution across all of pixels according to various ATP concentrations. The output voltages are initial output voltages measured at 9 seconds and demonstrates an excellent uniformity of the pixel responses with the standard variation (σ) of 0.68 mV. Additionally, the σ obtained 0 mM ATP is a black value and means a noise signal of our sensor. Using this value, the minimum detectable pH change, i.e. pH resolution (pH_{resol}) can be defined as

$$pH_{resol} = \frac{\sigma}{Sensitivity,S} \quad (16)$$

In figure 20, the membrane with a thickness of 0.3 μm shows the highest response of 0.032 V for 1 mM ATP solution. The decreased response means that the membrane does not contain enough apyrase to react with ATP when the thickness is thinner than 0.3 μm . Meanwhile, when the membrane is thicker than 0.3 μm , the movement of H^+ ions through the membrane is obstructed by the thick cross-linked polymer. Based on these results, an apyrase-immobilized membrane was patterned into a size of 250

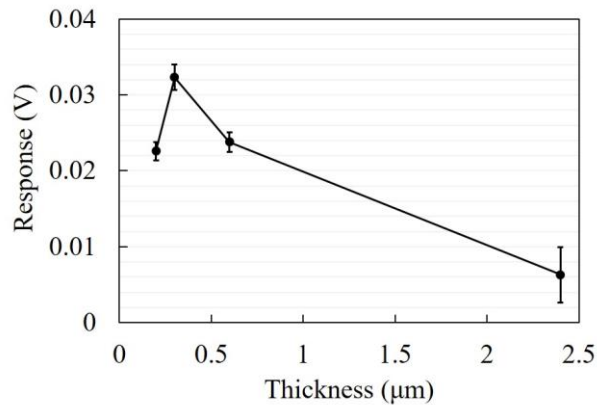


Figure 20 Response with respect to the thickness of the apyrase-immobilized membrane (n=16384).

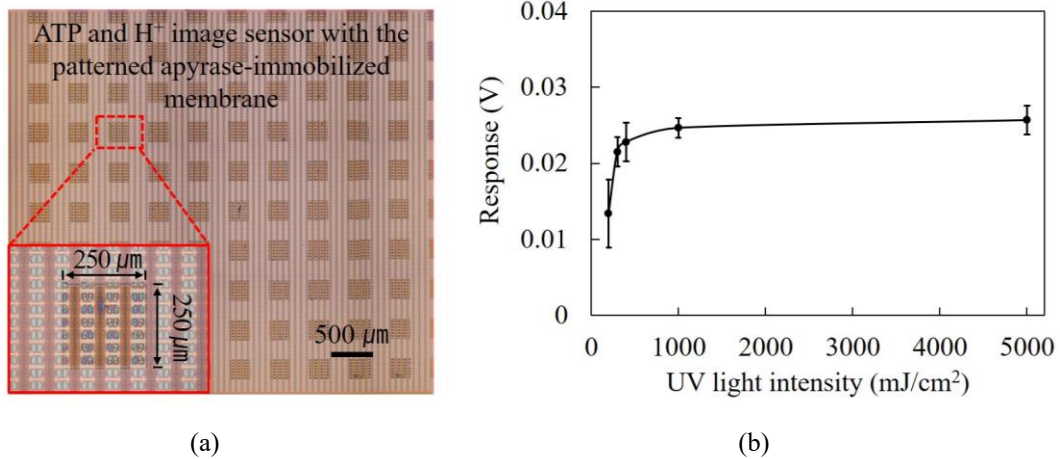


Figure 21 (a) Optical image of the fabricated ATP and H^+ image sensor with the patterned apyrase-immobilized membrane with the size of $250 \mu\text{m} \times 250 \mu\text{m}$. (b) Response with respect to the UV light power of lithographic method for patterning a membrane ($n=36$) at 1 mM concentration ATP.

$\times 250 \mu\text{m}^2$, as shown in figure 21 (a). For patterning the apyrase-immobilized membrane, we used one cycle of the fabrication process in figure 17 (a) - (c). UV light energy over 1000 mJ/cm^2 allowed us to obtain the saturated response to the ATP, as shown in figure 21 (b). The measured response corresponding to 1000 mJ/cm^2 was 0.025 V for 1 mM ATP, and this light intensity is considered to be sufficient for patterning the membrane. The decrease response in below 1000 mJ/cm^2 means that weak light did not form sufficient cross-linking structure and enzymes were lost during rinse. The response of the sensor with the patterned membrane was lower than with the non-patterned membrane, even though the two types of membranes were deposited in the same conditions. That is the only difference between the two types, whether the apyrase-immobilized membrane is patterned or not. It indicates that the H^+ ion produced by enzymatic reactions can diffuse and be detected at adjacent pixels.

4.3.2 Detecting and real-time imaging in ATP and H^+ dynamics

Before imaging of ATP and H^+ dynamics, the ATP sensitivity and detection limit of the fabricated sensor were achieved. The sensor was calibrated according to various ATP concentrations, as shown in figure 22.

The upper limit of the linear response range is up to 0.6 mM ATP and the calculated linearity in the region presents

$$y=0.0378x+0.002=ax+b \quad (17)$$

hence, the a is the sensitivity of 37.8 mV/mM ATP with $R^2=0.9934$. Because a is the sensitivity, the pH resolution of our sensor is 0.017 mM as mentioned in the equation (16).

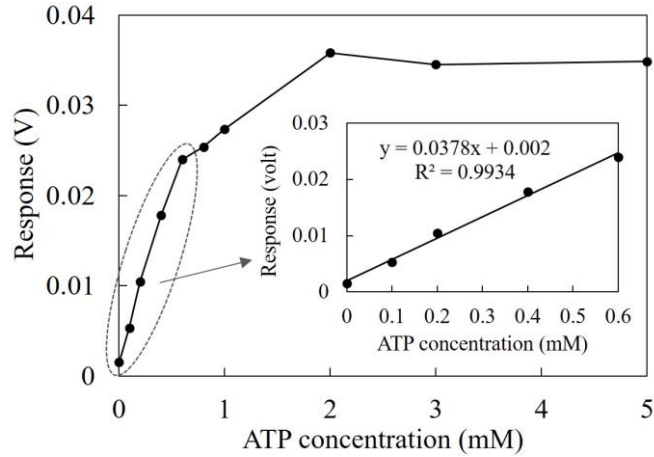


Figure 22 ATP calibration curve and linearity of the proposed bio-image sensor (n=49).

This data is also useful to obtain the limit of detection (LOD) that is the lower limit. In the general definition of IUPAC⁹⁷, LOD is defined as

$$\text{LOD} = \frac{3\sigma - \text{Black value}}{\text{Sensitivity}, S} = \frac{3\sigma - b}{a} \quad (18)$$

When 3σ that is the noise of our device is 2.047 mV, the LOD is 1.25 μM ATP.

Now we know how the measured response at a single pixel can represent a change of the ATP concentration. Our image sensor can reconstruct the output voltages measured at all of 128×128 pixels into 2D images sequentially. The output voltage difference was expressed by a color. Figure 23 (a) shown that all pixels can detect H^+ concentration movement after dropping pH 4.1 buffer solution into pH 8.0 buffer solution. The pH value of the mixed solution at 160 s was pH 7.1. The detection delay at the sensing area of the patterned membranes was measured, because H^+ ions had to pass through the membrane. By the same sensor, the sequential images in figure 23 (b) were obtained after adding 10 mM ATP solution droplet into pH 8.0 buffer solution. The final ATP concentration in the mixed solution was 1 mM. The real-time images are providing the spatiotemporal information of ATP movement, because the pH change was caused by the produced H^+ ions between ATP and the immobilized apyrase. However, the produced H^+ ions were able to diffuse through the solution and be detected by pixels without the apyrase-immobilized membrane. The gradually diffused ions were confirmed by the increased output voltage in the images at 30 s and 160 s.

The H^+ diffusion pathway can be analyzed by the measured data from the serial pixels including the apyrase-immobilized pixels in the center as shown in figure 24. In order to obtain the measurement result without the effect of the diffused H^+ ions, the response data of 12 pixels from the 2D images of figure 23 (b) was extracted and used to evaluate the diffusion characteristics of H^+ ions. Figure 24 shows the sequential response values corresponding to each pixel in an optical image, consisting of

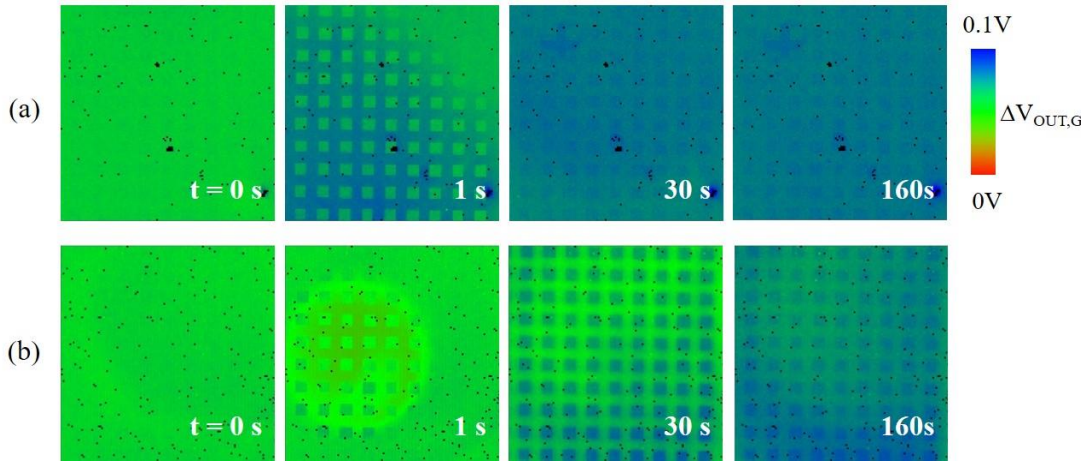


Figure 23 Real-time imaging of ATP and H^+ dynamics by using the fabricated image sensor with the apyrase immobilized membrane. At the time of 0 s, it was measured with pH 8.0 buffer solution. Then, (a) pH 4.1 buffer solution droplet and (b) 10 mM ATP solution droplet were added in the left corner.

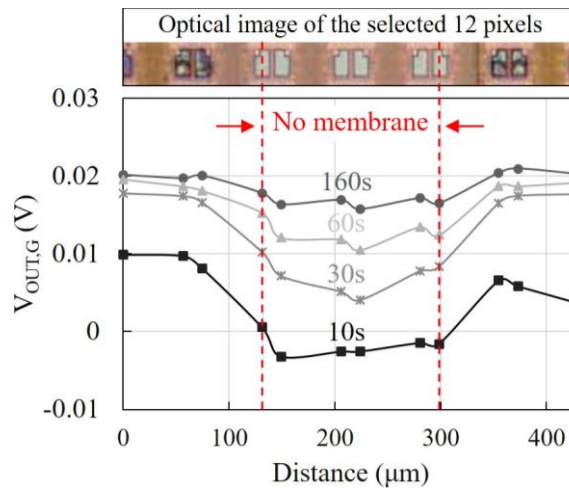


Figure 24 Diffusion characteristics of the produced H^+ ions at the apyrase-immobilized membrane are confirmed by the response change at sensing area without the membrane.

six pixels without the membrane in the center and the other six pixels with the apyrase-immobilized membrane on each side. Even though the six pixels without the membrane have no enzymatic reaction, the measured response in the area was gradually increased depending on the amount of the diffused H^+ ions from the adjacent pixels with the membrane. The biggest response difference between the two areas, where the membrane exists or the membrane does not exist, was observed at 10 s after adding ATP solution. When we consider the diffusion coefficient D of H^+ ions of $7.62 \times 10^{-5} \text{ cm}^2/\text{s}$ ⁹⁸, it is assumed that the diffused H^+ ions at a patterned membrane takes approximately 10.3 s to reach to the nearest pixel of the next membrane. Hence, in order to minimize the effect of the diffused H^+ , it is appropriate that the activities of ATP should be measured within 10 s after adding ATP solution. However, to observe the level of a synapse, the pattern size should be reduced and the diffusion effect will become problematic. Some measures to prevent the signal cross-talk will be attempted.

Bio-image sensor

Our aim in this thesis is the development of bio-image sensor capable of simultaneous detection and real-time imaging of the variation in the concentration of more than two kinds of neurotransmitters and H^+ . We have attempted to fabricate the bio-image sensor and succeed to visualize the dynamics of ATP, ACh and H^+ by using the fabricated sensor. Not only the design of patterns on the pixel array, but also how the discriminability can be improved in the bio-image sensor will be discussed in this chapter. These studies were reported by Lee et al.^{28,29}

5.1 ATP, ACh and H^+ image sensor

ATP, ACh and H^+ image sensor is a further development of our previous research. This bio-image sensor contains a patterned enzyme-immobilized membrane, as small as a pixel size, to enhance spatial resolution. In addition, we tried to improve the sensor with several attempts, such as new pattern placement and barrier layers that can reduce the cross-talk signals resulted from the proton diffusion after enzymatic reaction. This study hints us that a bio-image sensor can be customizable depending on the kinds of proton-consuming or proton-generating enzymes immobilized on pH image sensor. To detect other combinations of neurotransmitters, the other enzymes producing or consuming H^+ after an enzymatic reaction can be applied.

For patterning the apyrase-immobilized membrane, we used two cycles of the fabrication process in figure 17 (a) - (c). AChE and apyrase are used in sequence. And the barrier layer is prepared as following figure 25. It is almost same sequence with figure 17 excepting the photomask and enzymes. A mixture of 40 μ l crosslinking polymer and 10 μ l Milli-Q water is deposited. At 3000 rpm spin coating speed, the thickness of a buffer layer is 0.3 μ m. And then the deposited layer cured by UV light for 100 seconds. The cross-linked layer is rinsed by the running water for about 30 seconds. If you would not want to worry about the remaining enzymes on the previous membrane, I recommend to rinse for longer time and to deposit membranes in order of them with AChE to apyrase. The thickness of the buffer layer is controlled by repeating the process (d) – (f).

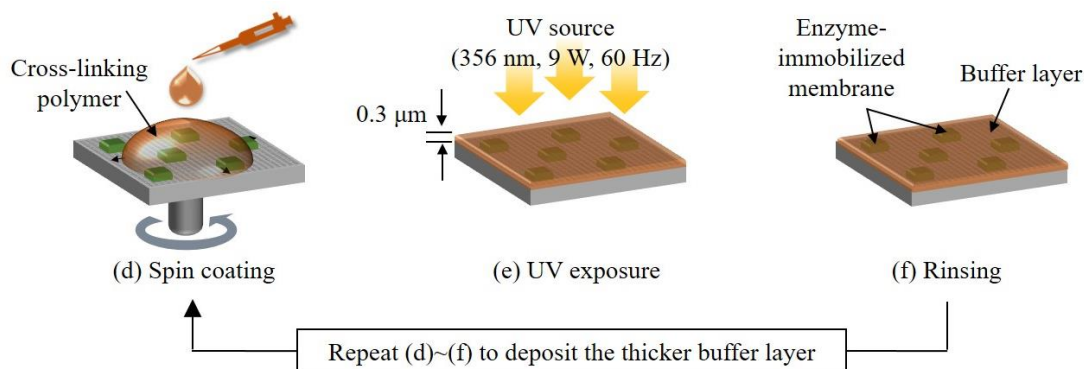


Figure 25 Buffer layer deposition process.

The main point of this study is the immobilization of AChE and apyrase on the H^+ sensitive pixel array for simultaneously monitoring the activities of ACh and ATP. By the corresponding enzymes, ATP and ACh are degraded into their by-products and protons. The majority of the generated H^+ is detected electrochemically at the pixels where the enzymatic reaction occurs. In addition, null sensors that have no enzyme are monitoring the diffused H^+ via electrolyte or the potential variation of non-specific electrochemical signals during the experiment.

5.2 Diffusion characteristics of H^+ and neurotransmitters

The diffusion of the generated H^+ after the enzymatic reaction in a solution is a very fast ($7.62 \times 10^{-5} \text{ cm}^2/\text{s}$ at room temperature)⁹⁸ and unavoidable phenomena in a biological experiment. In order to minimize a signal cross-talk due to the detection of the diffused H^+ at undesired pixels, we have investigated the phenomena and suggest a barrier layer depositing on the bio-image sensor.

Figure 26 (a) shows the diffusion pathway interrupted by the porous barrier layers which are used to decrease the immigration of the produced H^+ after enzymatic reaction. To demonstrate the H^+ diffusion preventing capabilities of the proposed barrier layer, apyrase or AChE is immobilized only at pixel ① and the surrounding pixels ②, ③, and ④ are used as null sensors to monitor the diffused H^+ . Enzyme-immobilized pixels like the pixel ① type are fixed at nine points on an array and placed as far apart as possible from each other to escape the diffusion effect. As shown in figure 26 (b), pixel ②, ③, and ④ are 18.1, 74.6, and 92.7 μm away from pixel ①, respectively. Diffusion characteristics of the produced and diffused protons after enzymatic reaction are observed according to various barrier layer thicknesses of 0, 0.6, 1.2, 1.8, 2.4, and 3.0 μm . Their response value is provided as the output voltage difference ($\Delta V_{\text{OUT, G}}$) between the measured value at 0 and 170 seconds after dropping the targeted solution into the electrolyte. In figure 26 (c), both apyrase-mediated degradation of 1mM ATP and AChE-mediated degradation of 1 mM ACh shows as the highest signal at the pixel ①. The magnitude of ΔV_{Out} measured at the pixel ②, ③, and ④ is dramatically decreased depending on the distance, because the pixels are detecting the H^+ propagated spherically out of the pixel ①.

Furthermore, the decreased ΔV_{OUT} according to the layer thickness indicates the consumption of the diffused H^+ from AChE-mediated degradation of 1 mM ACh. In case of the apyrase-mediated degradation of 1 mM ATP, the small output voltage signal makes difficult to distinguish the original signal and the decreased signal by the barrier layer. The diffused H^+ into the layer seems to be chemically bonded with unsatisfied chains of the crosslinking polymer or to be trapped by the porous structure. Because the H^+ detection at the pixel ④ with the barrier layers is nearly not obtained, we design so that the enzyme-immobilized pixels are placed at intervals of over $92.7 \mu\text{m}$ to minimize signal overlap.

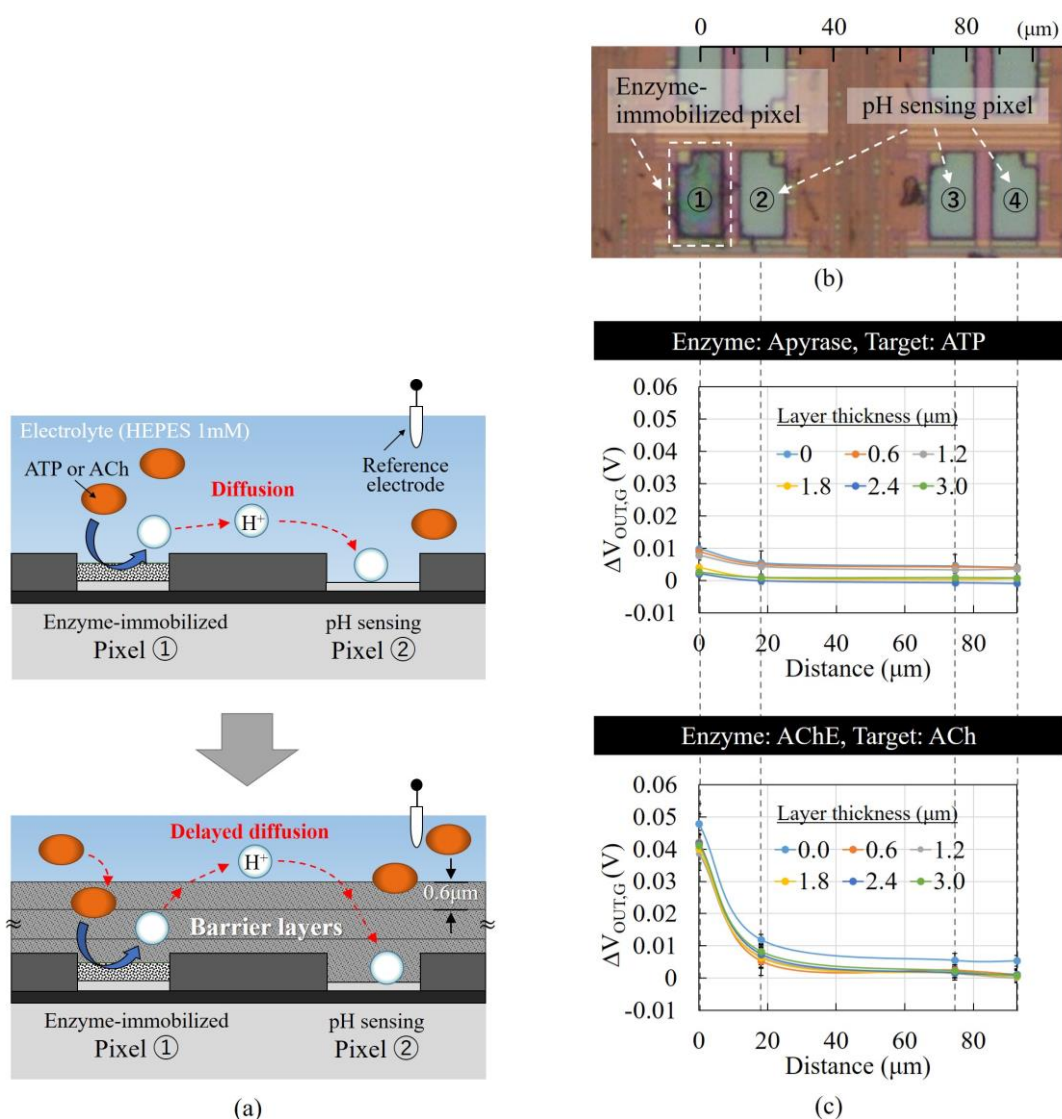


Figure 26 H^+ diffusion barrier layers. (a) Illustration of the diffusion pathways of the generated H^+ after enzymatic reaction. (b) Optical image of an enzyme-immobilized pixel ① and pH sensing pixel ②, ③, and ④, as null sensors (c) Diffusion characteristics of the produced and diffused protons according to various barrier layer thicknesses. The mean output voltages ($n=9$) represent the response values measured before/after enzymatic reaction between apyrase immobilized at pixel ① and 1 mM ATP (top), or between AChE immobilized at pixel ① and 1 mM ACh (down).

To optimize the thickness of the barrier layer, we have to consider a thicker layer can obstruct the inflow of ATP and ACh, as shown in figure 27. The saturation speed that indicates the immigration speed of 1 mM ACh from electrolyte to the sensing area surface at the pixel ① is reduced from 36.1mV/s to 0.1 mV/s, when the barrier layer thickness is changed from 0 μm to 3.0 μm . On the other hand, the saturated value of ΔV_{Out} seems to be independent of the layer thickness. We are considering that most of the unsatisfied chains such as dangling bonds exists on the surface of the barrier layer, and they catch the diffused H^+ as much as the reduced voltage value due to the existence of a barrier layer. Therefore, the thin barrier layer of 0.6 μm has been determined to deposit on the bio-image sensor. When 0.6 μm -thick layer exists on the pixel ①, the saturation speed is 9.8 mV/s with $R^2=0.9165$.

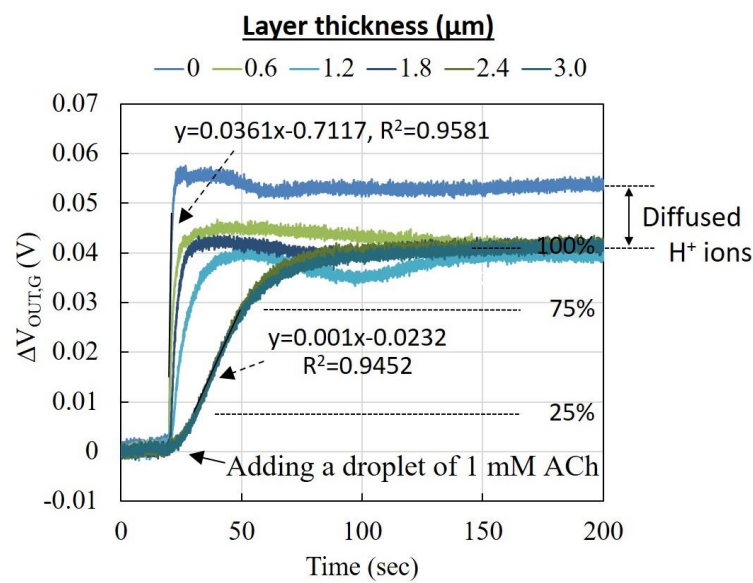


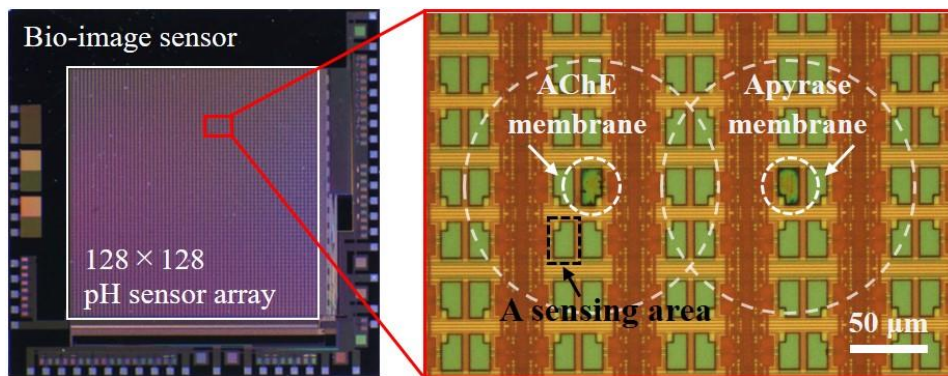
Figure 27 Saturation speeds according to H^+ barrier layer thickness, when ACh of 1 mM concentration reacts with AChE immobilized at pixel ①.

5.3 Bio-image sensor design

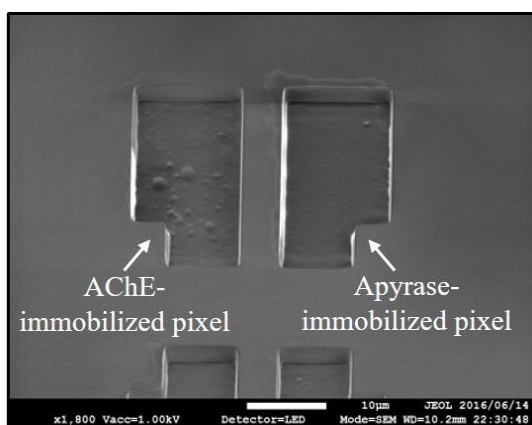
The fabricated bio-image sensor before depositing the 0.6 μm -thick barrier layer is shown in figure 28. Apyrase-immobilized pixel is located 92.7 μm to ACh-immobilized pixel. A pair of the two kinds of enzyme-immobilized pixels and surrounding null pixels has a space of $280.3 \times 223.8 \mu\text{m}^2$, thus it is provided at a spatial resolution to distinguish multi-neurotransmitters. 256 pairs are placed to map the activities of ATP, ACh, and H^+ concentration change.

5.4 Imaging of ATP and ACh

Figure 29 demonstrates the utility of the bio-image sensor to image spatial and temporal distributions of multi-neurotransmitters. As seen in the simultaneous images observed after adding droplets of 1 mM ATP, 1 mM ACh, and 1 mM mixture, the selective detection of ATP and ACh presents as dots by



(a)



(b)

Figure 28 (a) Optical image of the proposed bio-image sensor with AChE and apyrase immobilized pixels circled. (b) SEM images of AChE and apyrase immobilized pixels that are prepared just for this image. A barrier layer has not deposited yet. The other pixels without enzyme membrane act as pH sensing pixels.

the corresponding enzyme-immobilized pixels. The images at the 0, 5, and 100 seconds time points provide the spreading movement presented in figure 29(a). Here, to examine the effect of the H^+ diffusion barrier layer, we compare the response for a 1 mM mixture solution of ATP and ACh at the horizontally selected pixels from (64,46) to (105,46) in figure 29 (b). The peaks at 100 seconds become much more distinguishable than when the barrier layer is absent. The signal intensity of 1 mM ATP, that is approximately 6.2 times smaller than that of 1 mM ACh, could be due to the buffering ability of HEPES in electrolyte or a difference of dissociation constants. Finally, we compare the voltage peaks of the example cross-section extracted from the images of 1 mM ATP, 1 mM ACh, and 1 mM mixture, as shown in figure 29 (c). ATP and ACh are detected only at apyrase and AChE-immobilized pixels, respectively. It means that enzymes are not mixed during the repeated coating process. Additionally, the overlapping results of the voltage peaks measured individually for detecting ATP and ACh are exactly matched up with the peaks generated by the mixture solution. These results suggest that the detection of multi-neurotransmitters by the proposed bio-image sensor is nearly H^+ diffusion-independent. This hints at that a bio-image sensor can be customizable depending on the kinds of proton-consuming or proton-generating enzymes immobilized on pH image sensor.

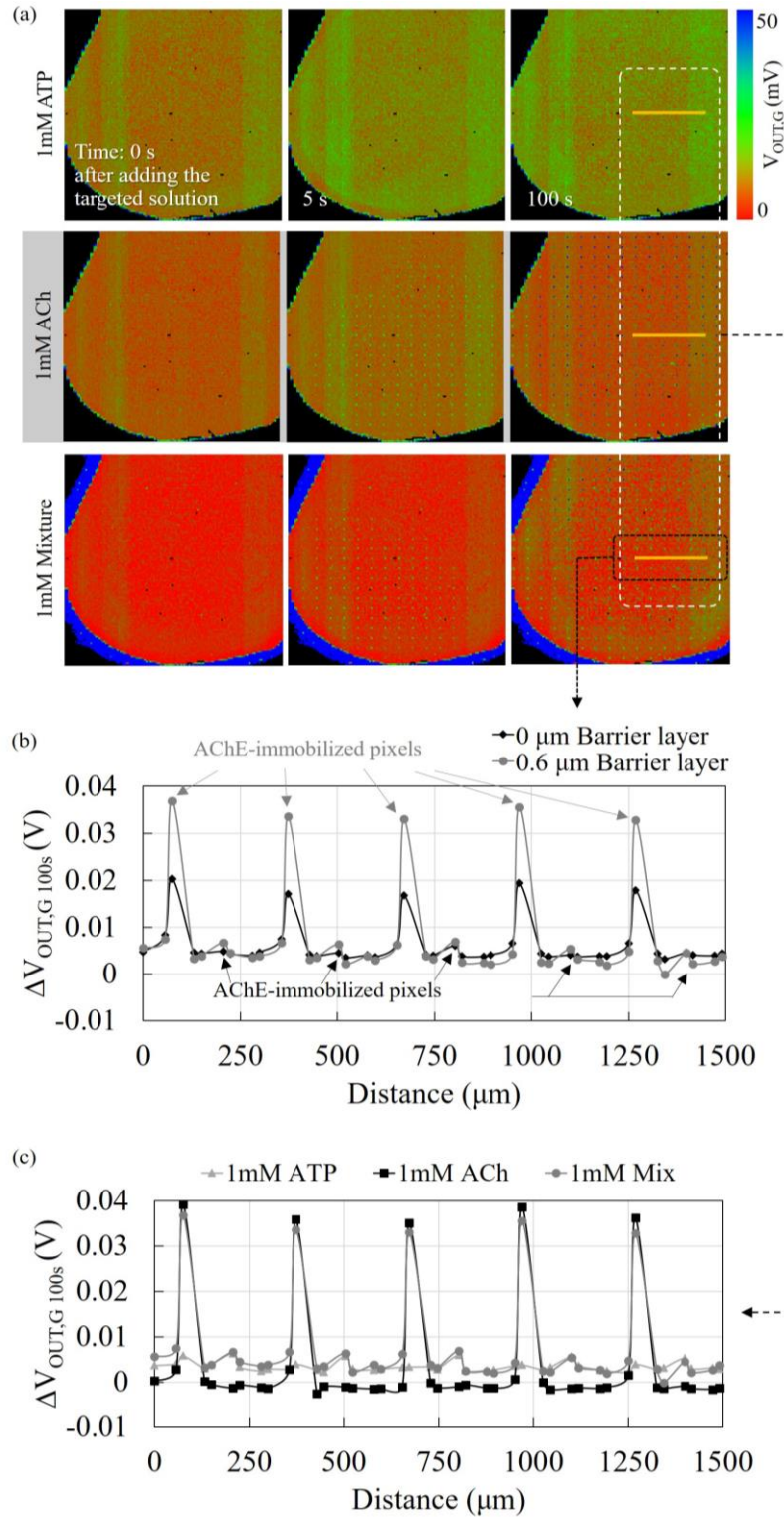
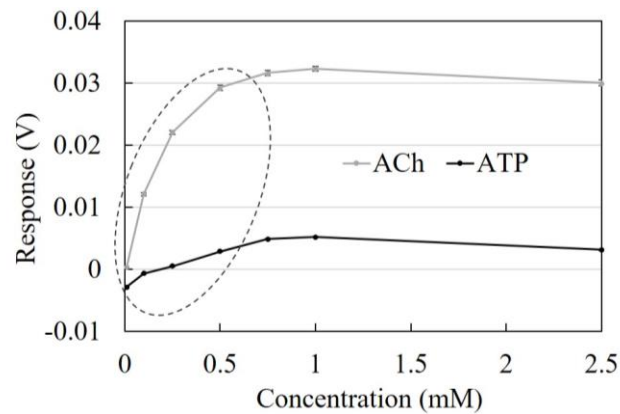


Figure 29 Simultaneous imaging of ATP, ACh, and their mixture. (a) Simultaneous imaging at 0, 5, and 100 s after adding a droplet of the targeted elements such as 1 mM ATP, 1 mM ACh, and 1 mM mixture. Locations of example cross-sections in **b**, **c** are from (64,46) to (105,46) by yellow lines. (b) Example cross-section from the image in **a** compared with the measured results without a barrier layer at the same location and detection timing after adding the mixture solution. (c) Example cross-section from the image in **a**.

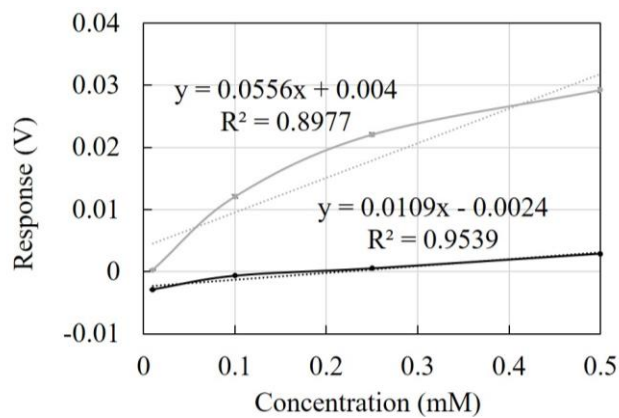
5.5 Sensing characteristics

To demonstrate the ATP or ACh sensing capability of our bio-image sensor, the detection characteristics are evaluated as calibration curves determined by averaging 100 pixels each depending on the immobilized enzymes, as shown in figure 30. Variability of ΔV_{Out} measured in pixels for a given ATP or ACh concentration increases with increasing concentration. The obtained sensitivities are 55.6 mV/mM for ACh detection with $R^2=0.8977$ and 10.9 mV/mM for ATP detection with $R^2=0.9539$ in the concentration range up to 0.5 mM. The LODs are 0.43 mM ATP at apyrase-immobilized pixel and 0.07 mM ACh at AChE-immobilized pixel, offering enough performance for analyzing their roles in the human cortical or blood ^{79,99}. A better LOD for sub- μM resolution to analyze the synaptic transmission of neurotransmitters will be pursued in future study.

When the bio-image sensor stored at -4°C and had been measured 0.5 mM mixture for 10 days to evidence the measurement repeatability, it shows very small output voltage drift of -0.02 mV/hour at AChE or apyrase-immobilized pixels as shown in figure 31. It seems to be related to the functional decline of enzymes.



(a)



(b)

Figure 30 ATP and ACh sensing characteristics. (a) Calibration curves of the proposed bio-image sensor ($n=100$) and (b) linearity in the concentration range up to 0.5 mM of the targets.

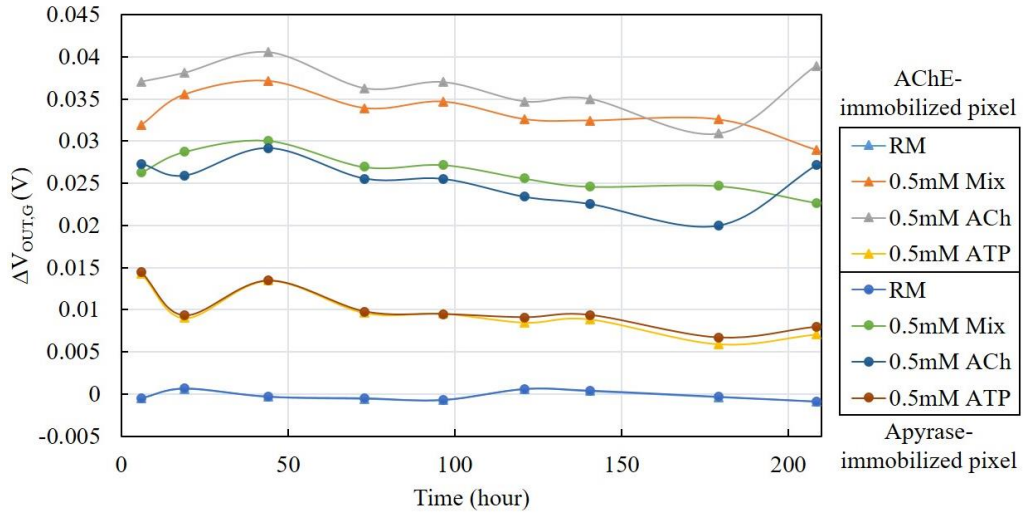


Figure 31 Reliability test of the fabricated sensor without barrier layers. Two pixels having AChE and apyrase respectively were measured according to the various solutions during 10 days and shows a good reproducibility.

5.6 Additional investigation - Microhole array

Microhole array is an additional mean to prevent diffusion of the produced H^+ ions after enzymatic reaction. Because this structure was constructed with SU-8 as a negative photoresist and have a very low moisture permeability, it is very effective to reduce the horizontal diffusion. Figure 32

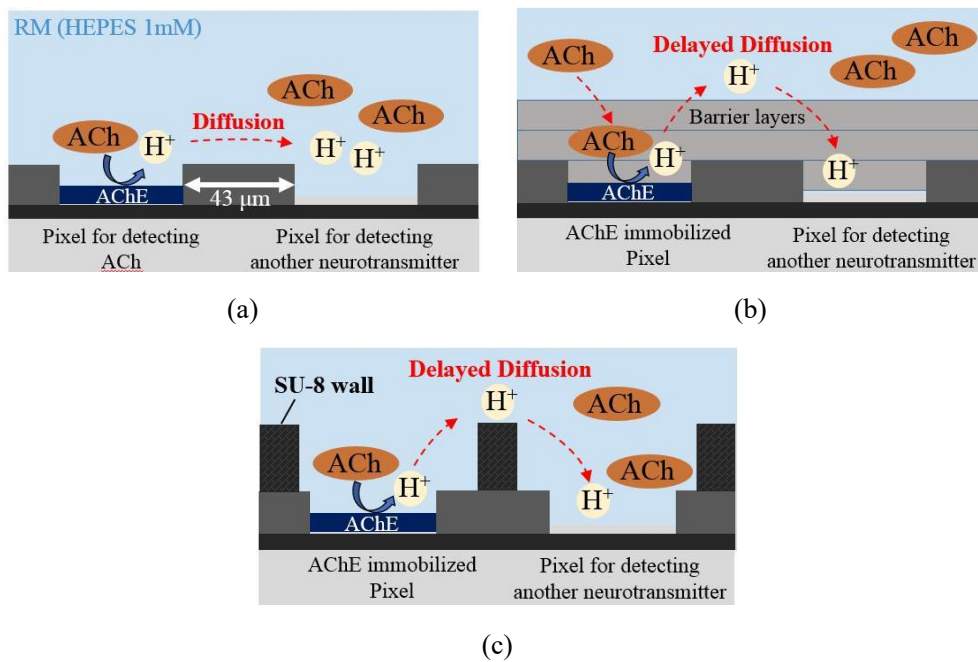


Figure 32 H^+ diffusion characteristics on an image sensor (a) without any additional structure, (b) with barrier layers, and (c) with micro hole array structure.

schematically illustrates the different diffusion pathways among ACh and H⁺ before and after enzymatic reaction. Unlike the barrier layers on the image sensor, the micro hole array structure has an opened space on a sensing area and does not disturb the ACh immigration from the RM to the sensor surface. We expect the combination of the barrier layers and microhole array to improve our sensor.

The fabrication process is following the basic photolithography method and the widely well-known detail process is referred in ¹⁰⁰. We prepared microhole arrays with various heights of 0, 15, and 60 μm on pH image sensors and the open area of a hole has the size of 24.5 × 31.6 μm² corresponding to the dimension of two vicinal pixels. Since SU-8 is a hydrophobic material, the solution cannot reach the sensing area without any appropriate treatment. Therefore, the SU-8 surface was modified to be hydrophilic by cleaning with a UV ozone cleaner for 15 minutes at 110 °C in an O₂ flow of 0.75 L/min. The treatment generates C=O hydrophilic functional groups on the SU-8 surface¹⁰¹. Figure 33 shows the fabricated micro hole array structure using SU-8 photoresist has a hole size of 24.5 × 31.6 μm² and a wall height of 60 μm that can surround two pixels.

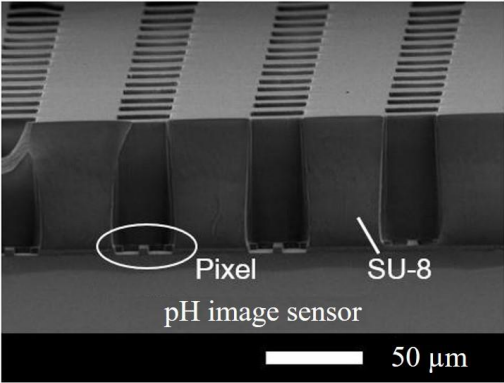


Figure 33 Cross-sectional SEM image of the micro hole array structure on a pH image sensor.

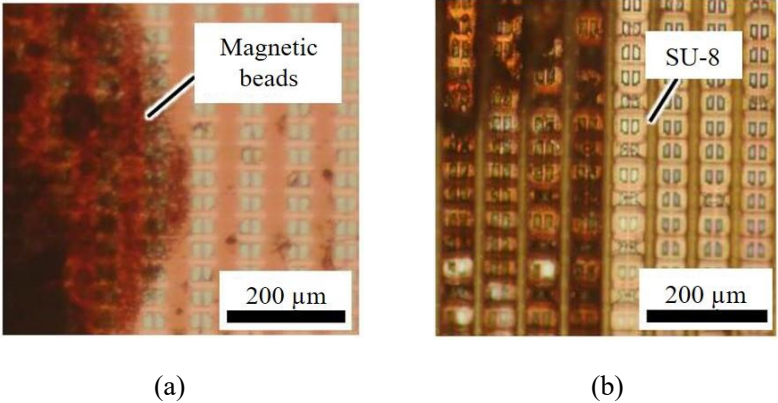


Figure 34 Top view images of the sensors with AChE immobilized using magnetic beads (a) without the structure and (b) with the structure.

5.6.1 Optimizing the array height

The microhole array structure with various heights of 0, 15, and 60 μm were constructed on bio-image sensors to find out the best height minimizing crosstalk signals. AChE is immobilized with magnetic beads and locally placed on sensors, as shown in figure 34. We confirmed that the beads are fixed only on the sensor surface and not on the wall structure. The output signals measured at the AChE immobilized pixels present the same ACh concentration dependence, whether with or without structures in figure 35. The ACh sensitivity of the sensor did not change regardless of the existence of the structure.

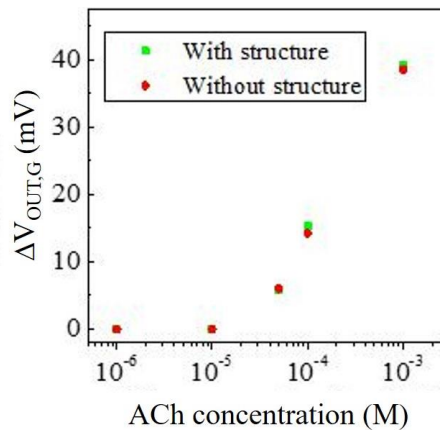


Figure 35 ACh concentration dependence of the sensor with and without the structure.

The diffused H^+ were measured in null pixels that were 75, 150, 225, and 300 μm away from the AChE-immobilized pixel presented as a point at 0 μm in figure 36 (a). As the structure became higher, $\Delta V_{\text{OUT,G}}$ became smaller. Particularly, there was almost no effect of H^+ diffusion of the pixels that are further than a distance of 150 μm , when the sensor had a 60- μm -height structure. We concluded that the discernment ability of a multi-neurotransmitter image sensor depends on the thickness of the proposed structure. However, if this sensor is applied to observe a nerve cell in our future works, a short distance between the cell and the sensing surface of the sensor might be necessary, due to the small amount of releasing neurotransmitters and the relatively short spacing between cells. Figure 36 (b) shows the starting time of the output voltage change caused by the detection of the diffused H^+ after adding a 1 mM ACh solution. The starting points measured by the pixel at 75 μm distance from the enzymatic reaction starting pixel did not dramatically change depending on the thickness of the structure. However, the delayed time of the starting point was observed at the pixel at 150 μm distance clearly. There was a time delay of almost double between the two sensors with 15 and 60 μm height structures. Therefore, in order to use the sensor with the structure of 15 μm height without the effect of the diffused H^+ , the distribution of ACh should be detected within 25 seconds after adding a 1 mM ACh solution. Based on this result, it is expected that a lower structure can be used by adjusting the measuring time or the spacing among enzyme-immobilized pixels taking the minimum effect by the diffused H^+ .

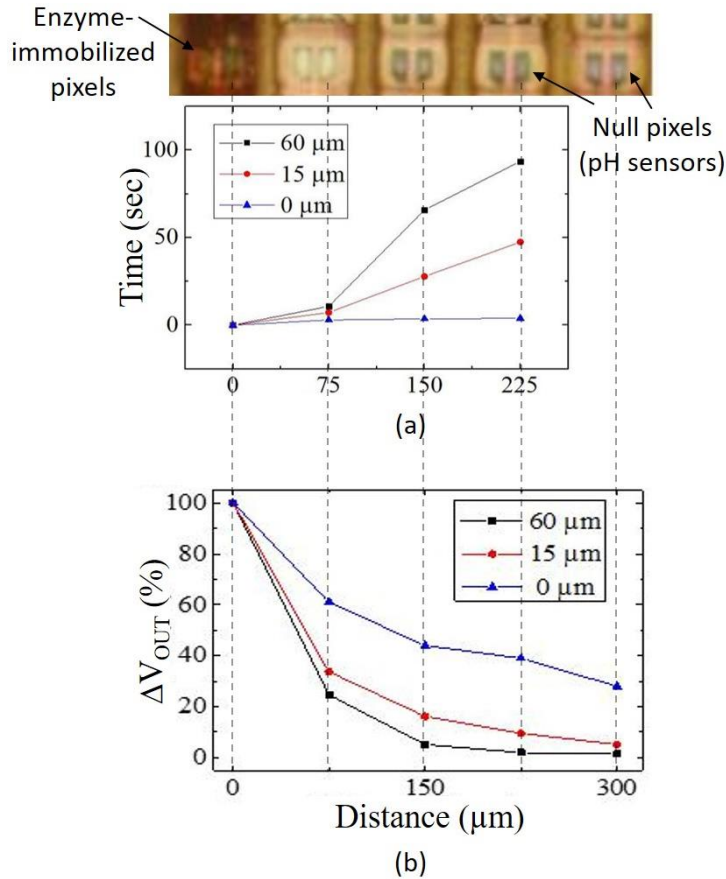


Figure 36 (a) Output voltage and (b) the reaction starting time after dropping ACh solution as a function of the distance from magnetic beads at three different structure heights.

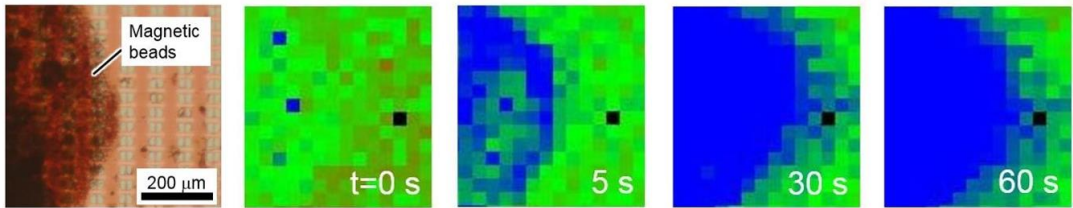
5.6.2 Comparison of H⁺ diffusions

To demonstrate the H⁺ diffusion prevention ability of the proposed structure, image sensors with and without a micro hole array structure are compared. These two kinds of sensors in figure 37 were used to measure the activity of 1 mM ACh into 2D real-time images with 14×16 pixels. In figure 37 (b) the sensor with the structure presents an increased output voltage only in the part where the AChE was immobilized on the left side after adding 1 mM ACh solution, while the sensor without the structure in figure 37 (a) presents H⁺ diffusion to the right side. These images provide us an intuitional insight that the proposed structure enables to suppress the H⁺ diffusion.

In figure 38, the measured time-dependent output voltage changes at two pixels are compared according to the existence of the micro hole array structure. Black line presents the H⁺ value generated at the pixel immobilized AChE after the enzymatic reaction whilst the red line is the measured data on a pixel with no enzyme which is 75 μm away from the AChE-immobilized pixel to monitor the diffused

H⁺. The output voltage percentage difference between an enzyme-immobilized pixel and a null pixel is increased from 35 % to 83%, according to the existence of the structure on the sensor. It means that the signal crosstalk caused by H⁺ diffusion is effectively reduced by the proposed micro hole array structure. The other strength of this wall structure is that it holds H⁺ that should be diffused if there was no structure, thus there is no loss of sensitivity which is a disadvantage of the H⁺ diffusion barrier layer.

(a) Without array structure, only beads



(b) With array structure and beads

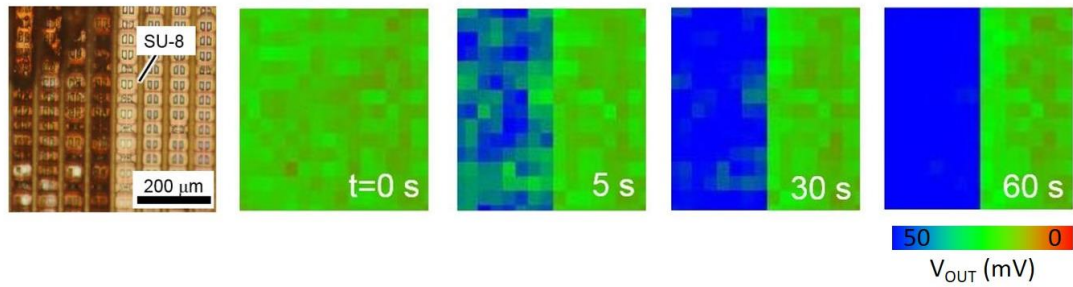


Figure 37 2D real-time image of 14×16 pixels after dropping 1 mM ACh (a) without the structure and (b) with the structure.x

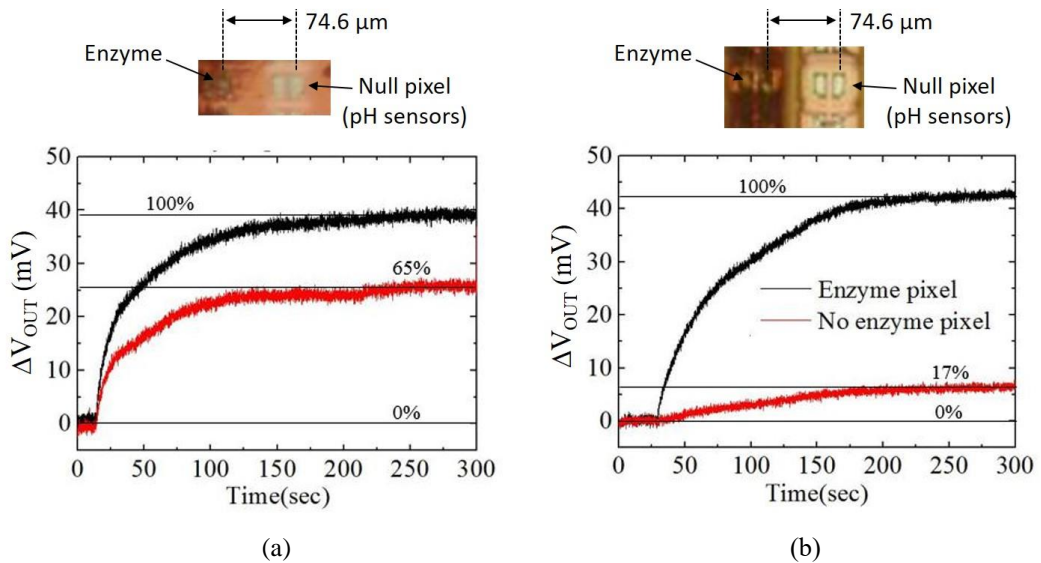


Figure 38 Time-dependent changes in the output voltage measured at enzyme-immobilized pixel and no enzyme pixel (a) without the structure and (b) with the 60-μm-height-structure.

High performance pH-image sensor

To provide a better image platform, we developed new pH image sensor consisted of a higher-density array and more efficient readout circuitry and the study was reported by Lee et al. ³⁰ In this chapter, we introduce how we can achieve higher spatio-temporal performance by changing chip designs. The proposed sensor will be not only demonstrated its characteristics and imaging ability, but also compared to other state-of the-art pH image sensors. Additionally, we originally proposed a method to evaluate the practical spatial resolution of biochemical image sensors or arrays. The difference between the designed pixel pitch and the experimentally obtained practical spatial resolution will be discussed and verified by simulation.

6.1. Enhanced platform with higher spatio-temporal resolution

Real-time imaging of pH changes by biosensing platforms offers new opportunities in neural networks to observe chemical activity and to help understand their mutual interactions ^{102–104}. The transient, localized pH changes are caused via several mechanisms and indicate that there is neural activity at the corresponding place ⁵⁴. To study these biological changes, electrochemical strategies, such as an ion-sensitive field-effect transistor (ISFET), have been developed to transduce biochemical information from nerve cells to artificial systems. One of the key benefits in an ISFET is that the gate can be modified with specific biological elements such as enzymes, antibodies, ion selective polymer and nucleic acids ^{34–38}. These potential advantages of monitoring multiplex interactions among various analyte samples are promising multiple variations of the biosensing platform. Thus, recent studies have developed large-scale, high-density ISFET sensors based on the progress of CMOS integrated circuit technologies ^{59,105–109}. They allow imaging and recording activities in large neural populations.

Previous improvement in compact modelling includes variant gate structures on an ISFET, such as floating and extended gate ¹¹⁰, double gate ¹¹¹ or enclosed gate ³¹. While the sensing area size has been successfully reduced in many researches, their spatial resolutions are still insufficient to investigate the neurotransmission at chemical synapses. According to a report the synaptic density was 0.007 - 0.25 synapse/ μm^2 ¹¹² in hippocampal of a rat. In other words, it means that there is approximately one synapse per 4 μm^2 in case of high density. Apart from the chemical signals, the scaling of transistor dimension on a readout channel was successfully employed in achieving microelectrode array imaging of action potential ¹¹³. However, the imaging speed is still problematic as the sensor density increases. A significantly higher temporal resolution than a few milliseconds is required to detect molecules released from vesicles ¹¹⁴. Because of temporal requirements for real-time monitoring, some ion-image sensors process the measured signals to transfer digitized data via a pipelined analog-to-digital converter (ADC) ^{60,115}. To realize a small pixel size with a high frame speed, our sensor employs a column-parallel single slop (SS) ADC architecture connected with two memory cells. The SS ADC architecture is well known for having a good linearity and small area among CMOS imaging technologies for digital cameras ^{43,116}. The plural memory cells carrying out write and read by turns are implemented to achieve high-speed readout.

Therefore, we aim to design and develop a pH image sensor toward large-scale, high-density and fast frame rate imaging. The pH image sensor is fabricated by a modified CMOS process technology. A small pixel pitch is achieved by utilizing a shrunken in-pixel circuit and an efficiently arranged readout circuit architecture. Moreover, the frame rate is accelerated by the operation of measuring and readout in parallel. We then evaluate the imaging capability with high-spatial resolution in biological environments using the proposed pH image sensor.

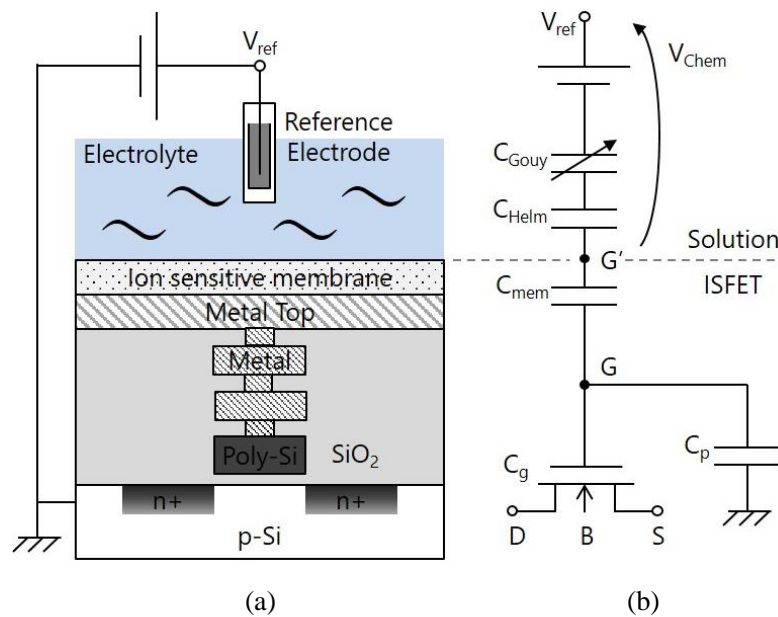


Figure 39 (a) A cross-sectional view of the extended gate ISFET structure and (b) its behavioral macromodel.

6.2. Operating principle

ISFET was developed as a chemical sensor, which is a MOSFET using the extended gate to an ion sensitive membrane replacing the gate oxide and requiring a reference electrode to operate in solution. Its structure is depicted in figure 39 (a). The pH response results from a parallel shift of threshold voltage ($V_{T(\text{ISFET})}$) in the ISFET I_D - V_{GS} characteristic. The shift is caused by the site-bonding reaction between the electrolyte and the surface of the Ta_2O_5 layer¹¹⁷. Therefore, pH sensing of the ISFET can be described using a combination of the surface reaction model and the Gouy-Chapman-Stern double layer model of ion distribution^{118,119} by

$$V_{T(\text{ISFET})} = V_{T(\text{nMOS1})} + V_{\text{Chem}} \quad (19)$$

and

$$V_{\text{Chem}} = \gamma + 2.3\alpha U_T \text{pH} \quad (20)$$

where $V_{T(\text{nMOS1})}$ is the threshold voltage of the nMOSFET (nMOS_1) in the extended gate ISFET structure; V_{Chem} a grouping of a chemical potential at the ion-sensitive membrane surface; γ a pH-independent grouping factor of chemical potentials; α a sensitivity parameter ($0 < \alpha < 1$) relative to the ideal Nernstian sensitivity; U_T the thermal voltage kT/q ; and pH a measure of the hydrogen ion activity $\text{pH} = -\log_{10}[\text{H}^+]$ in solution¹²⁰.

This model can be represented in an equivalent circuit as shown in figure 39 (b). The pH change causes the threshold voltage shift that is defined as a change in the floating gate voltage as follows⁴⁴,

$$V_{G'} = V_{\text{ref}} - V_{\text{Chem}} = V_{\text{ref}} - (\gamma + \alpha S_N \text{pH}) \quad (21)$$

$V_{G'}$ is a membrane surface voltage and S_N is the ideal Nernstian sensitivity that is limited to $2.3kT/q = 59 \text{ mV/pH}$ at RT⁵³. The reference voltage (V_{ref}) is an input signal of this model and is attenuated by the capacitive division:

$$\begin{aligned} V_G &= V_{G'} \left[\frac{C_{\text{mem}}}{C_{\text{mem}} + C_g + C_p} \right] \\ &= \left[V_{\text{ref}} - (\gamma + \alpha S_N \text{pH}) \right] \times \left[\frac{C_{\text{mem}}}{C_{\text{mem}} + C_g + C_p} \right] \end{aligned} \quad (22)$$

where C_{mem} , C_g and C_p are the ion sensitive membrane, gate oxide and wiring capacitances, respectively; and the V_G a gate voltage of nMOS_1 . The C_{mem} is given by

$$C_{\text{mem}} = A \varepsilon_0 (\varepsilon_{\text{Ta}_2\text{O}_5} / d_{\text{Ta}_2\text{O}_5}) \quad (23)$$

where A is the surface dimensions of a metal top; ε_0 the vacuum permittivity; $\varepsilon_{\text{Ta}_2\text{O}_5}$ the relative permittivity of tantalum pentoxide (Ta_2O_5) that is used as the ion sensitive membrane in our sensor; and $d_{\text{Ta}_2\text{O}_5}$ the thickness of the Ta_2O_5 membrane. The C_{mem} for our sensor is 1.6 fF.

As shown the proposed in-pixel circuit in figure 40 (b), the value of the charges that is stored at a floating diffusion (FD) by a source follower (SF₁) is readout via next source follower (SF₂) as an output voltage (V_{OUT}). SF₁ consists of nMOS₁ and its parasitic resistance as a source load resistor. The V_{OUT} considering voltage gains (g_n) of the source followers can be calculated, as below,

$$V_{OUT} \cong [V_{FD} - (V_{T(nMOS2)} + \Delta V_2)]g_2 = \{[V_G - (V_{T(nMOS1)} + \Delta V_1)]g_1 - (V_{T(nMOS2)} + \Delta V_2)\}g_2 \quad (24)$$

Here, the ΔV_n is a voltage difference via source followers and described as follows:

$$\Delta V_n = \sqrt{2I_n / (\mu C_g W / L)} \quad (25)$$

where I_n is the source follower current (I_1 or I_2); W and L the width and length of the channel of nMOSFETs (nMOS₁ and nMOS₂), respectively; μ the carrier mobility in the channel.

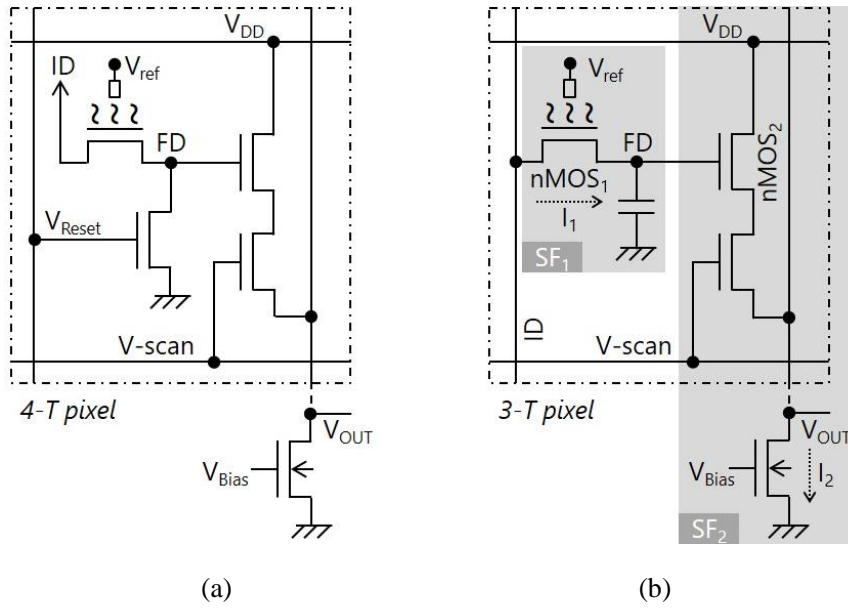


Figure 40 Analogue front end topologies for single pixel readout with (a) four transistors (4-T) and (b) three transistors (3-T).

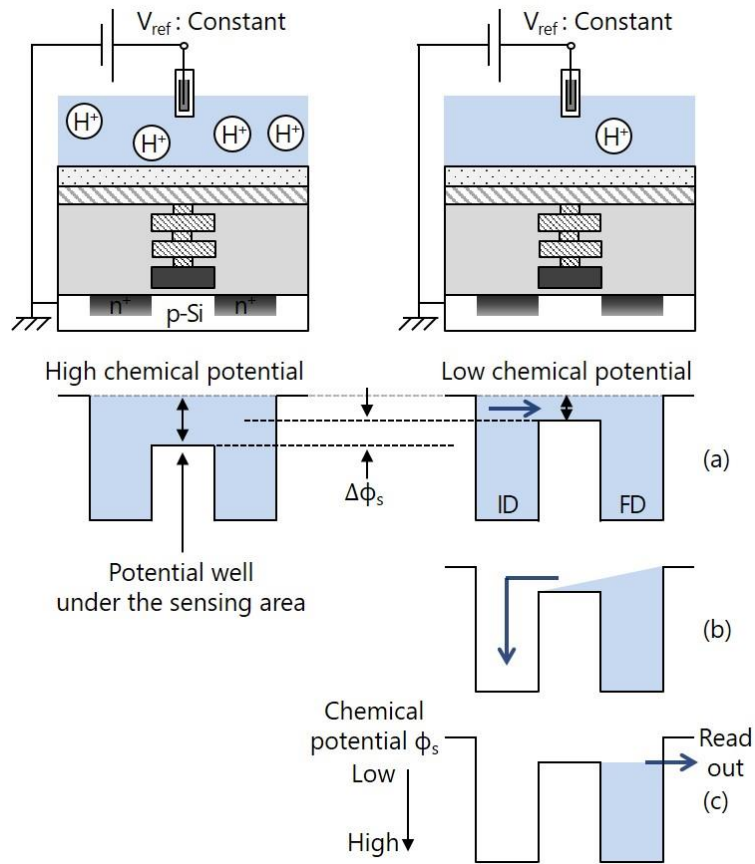


Figure 41 The operating principle of a pixel with three transistors to convert from pH changes to electrical signals. (a) Supplying charges into FD by biasing ID to GND. (b) Spilling the charges from FD by applying a high bias voltage of V_{DD} to ID. (c) Reading out the voltage level of FD through a source follower circuit.

6.3. Sensor chip design and fabrication

The proposed pH image sensor in this paper is rather like an active pixel sensor (APS) with the intra pixel charge transfer. The advantage of the APS architecture is that it can be fabricated in large and dense arrays and is highly compatible with advanced CMOS device processes⁴⁴. In order to detect the ion concentration, the ISFET is inserted as an active transistor within each pixel. In this section, we introduce several techniques that are used to enable the denser array and higher frame rate.

6.3.1. Pixel structure

A chemical APS topology with four transistors (4-T) was suggested in our previous work, as shown in figure 40 (a)⁶⁴. Unfortunately, its pixel size was insufficient for tracing synaptic signaling pathway among nervous cells. The scaling of a pixel pitch is an important aspect of imaging device applications. Based on the previous APS topology, we explore the possibility of a simpler pixel structure with a reduced number of transistors for each pixel, hence increasing the spatial resolution. The proposed pixel with three transistors (3-T) is shown schematically in figure 40 (b). Its operating principle to convert pH changes to electrical signals is depicted in figure 41. The depth of the potential under the sensing area is changed by the hydrogen ion (H^+) concentration on the ion-sensitive membrane surface. By setting an input diode (ID) to GND, electrons are charged into the FD. Next, excepting some electrons corresponding to the potential level of the sensing area, the others are discharged to ID due to the increased voltage level of V_{DD} . The potential at the sensing area depends on a pH value of a sample. The potential is then read out through a source follower circuit by turning on a transfer gate transistor (TG). The applied voltage of V_{DD} is 3.3V. The fabricated pixel size is $2 \mu m \times 2 \mu m$. In the top view of a pixel layout, a metal top area of $1.42 \mu m \times 1.42 \mu m$ and a spacing of $0.58 \mu m$ are placed as shown in figure 42.

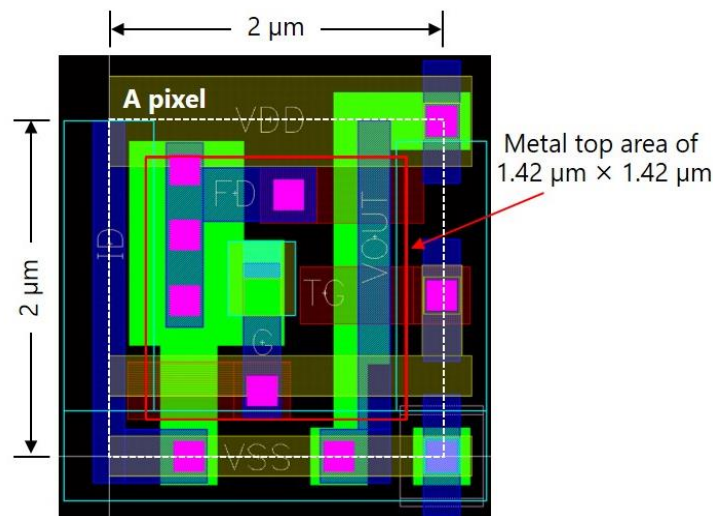


Figure 42 A top view of the designed pixel layout.

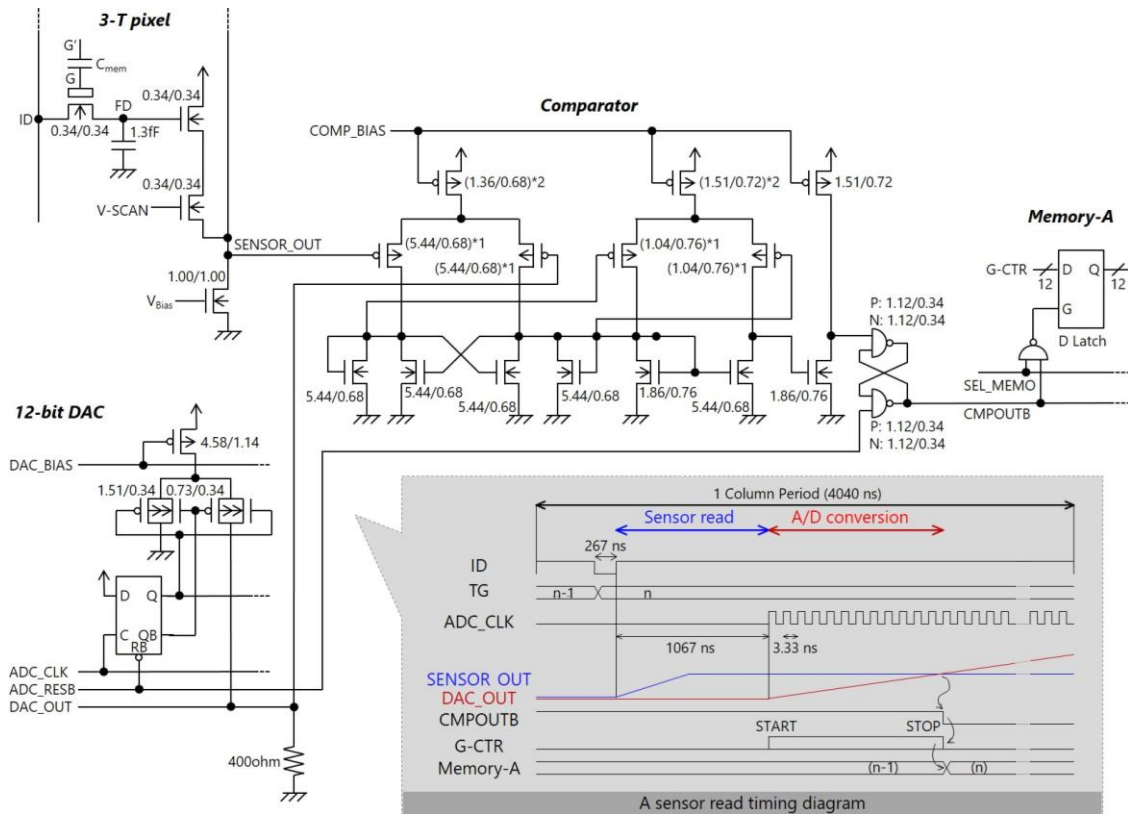
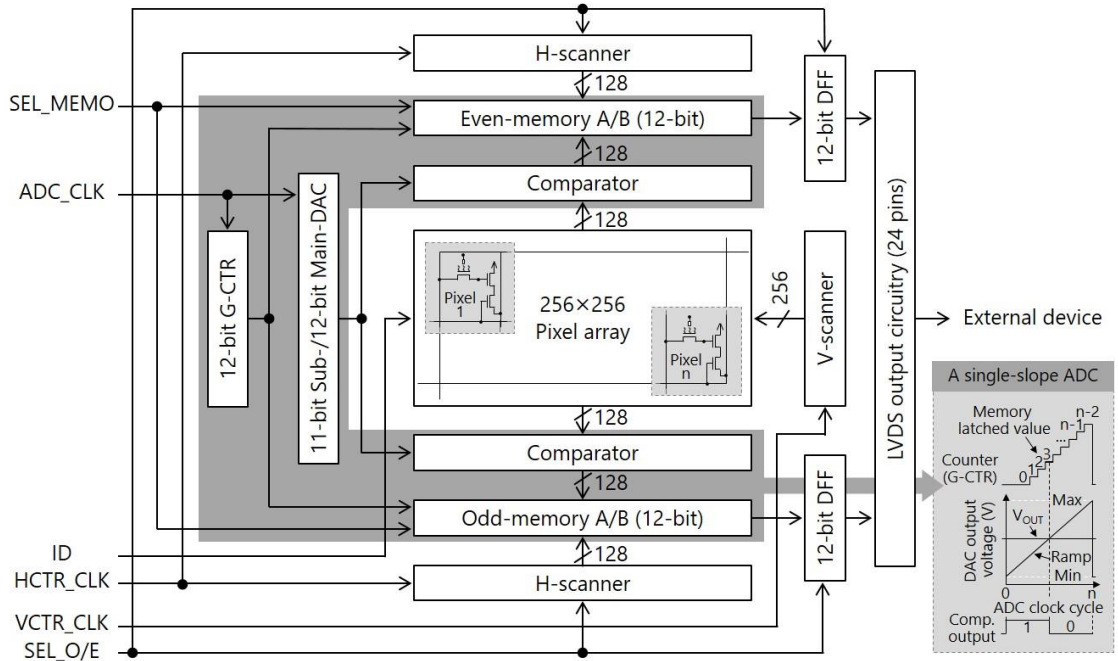
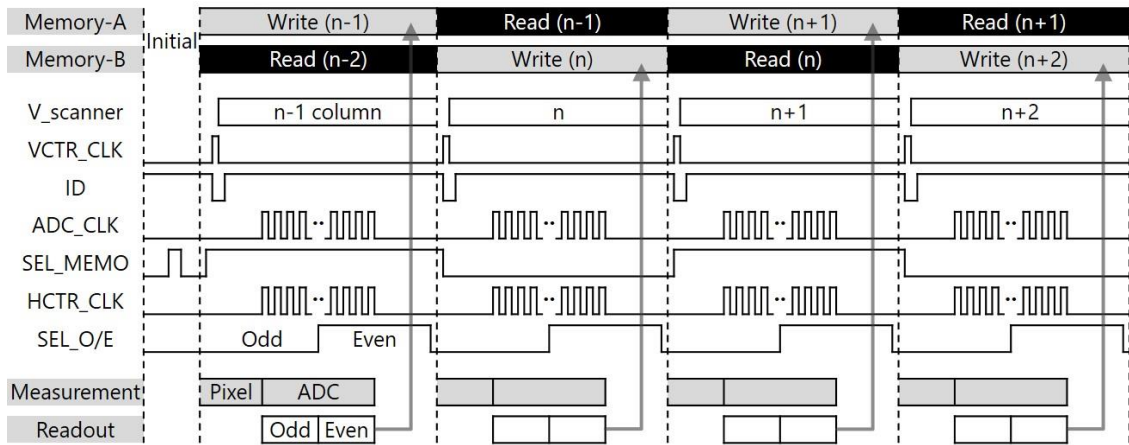


Figure 43 Sensor readout circuit schematic. Sensor read timing diagram.

Figure 43 illustrates the sensor read circuit that consists of a 3-T pH sensor circuit, a 12-bit digital-to-analog converter (DAC), a comparator, and a memory. The pH sensor circuit composed an ISFET, a TG, a bias transistor, and a FD. The three transistors have a same gate size (width = 0.34 μm and length = 0.34 μm), and implement with the gate circuit using the standard thick oxide (3.3V) transistors, commonly used in I/O circuits, to prevent undesired leakage currents. The FD has a parasitic capacitance of 1.3 fF. We decided to use a comparator comprising of two differential amplifiers, because the smallest offset voltage of a comparator was achieved in our preliminary simulation using this circuit design. The DAC consists of Main-DAC and Sub-DAC. The Main-DAC generates an analog ramp signal that increments by 1 LSB per an ADC clock signal (ADC_CLK). Meanwhile, the Sub-DAC works once at the start of operation and determines the starting voltage value of the ramp signal sweeping range. The output value of a DAC, thus, is the sum of output values (DAC_OUT) of a Main-DAC and a Sub-DAC. As shown in a read-timing diagram highlighted in figure 43, a sensor output (SENSOR_OUT) is initialized at a low level of ID, and then starts to read the output signal at the moment when the level of ID switched on to high. After a waiting time of about 1 ms, a ADC_CLK is inputted to the DAC to generate analog ramp signals by the Main-DAC. Next, an A/D conversion and a counting of a gray code counter (G-CTR) are carried out simultaneously. At the crossing moment of the SENSOR_OUT and DAC output (DAC_OUT) signals that are inputted to the comparator, the counting of G-CTR is stopped. The counting values are the digitized data of SENOR_OUT and recorded in Memory-A. Writing processes of Memory-A and Memory-B are controlled by memory selection signals (SEL_MEMO).



(a)



(b)

Figure 44 pH image sensor (a) system block and (b) timing diagrams.

6.3.2. Array architecture

Figure 44 shows a block diagram of the pH image sensor architecture along with a timing diagram taken from various points within the architecture. 256×256 pixels are arranged in a 2D grid with readout circuitry integrated to efficiently measure the full array. Because a unit size of memory and comparator circuits are bigger than that of a single pixel, the integrated circuits are split into top and bottom parts to be arranged densely. Each of them is connected to odd or even columns of a pixel array that is selected by a vertical scanner line (V-scanner). A 12-bit ADC consists of a G-CTR, DACs, memory circuits and comparators. 256 ADCs are connected to each pixel column. And the dynamic range of the ADC is from 0 V to 1.4 V.

To operate with a high frame rate, three measures against the circuit design are implemented. The first measure is to have two kinds of memory. Each odd- and even-memories have a two sections named Memory-A and Memory-B, in order to store digitized data. These two kinds of memory segment allow the image captures to be processed in parallel with the readout processes. Therefore, the operating time that is required for an array integrated with a single memory reduces by almost half. As depicted in figure 44 (b), one column (n-1) of the array is temporally stored in one of memories, and then quickly transferred to a next stage while the data of the next column (n) is being captured. Writing to and reading from the Memory-A and the Memory-B are controlled by SEL_MEMO and the data in the memory are read in order of odd and even by HCTR_CLK and selection signals (SEL_O/E). The operating time of one column period is determined by the longer one of the sensor measurement time and readout time.

The second measure is to implement a sub-DAC in order to reduce analog-to-digital (A/D) conversion time. Our sensor employs a single-slope type ADC technology, as shown in figure 44 (a). The A/D conversion time is determined by the counting steps, as a stepped digital ramp, of G-CTR. By setting an initial voltage value close to the sensor output using the Sub-DAC, it allows to reduce counting steps spent for comparing of the sensor output and the DAC output during operation of the Main-DAC. The third measure is to make it possible to select two types of pixel array configuration, 256×256 and 128×128 . In case of the 128 odd rows \times 128 odd column configuration, the number of columns and the number of rows per screen are halved, and the frame rate is greatly improved. According to the reduced pixel number, the imaging resolution is degraded by half, but the total size of measuring region is not changed.

Additionally, for the high-speed data transmission between our sensor chip and a printed circuit board (PCB), we employ a standard LVDS technology at the end of the device circuit. The implemented termination scheme is the simplest one having a single resistor of 100Ω between the driver outputs. This LVDS is able to operate up to 350 MHz. The proposed sensor design is fabricated in the modified

1-poly 4-metal 0.15 μm CMOS technology, including a deposition process of Ta_2O_5 . Figure 45 shows a microphotography of the 5.2 mm \times 5.2 mm chip consisting of 256 \times 256 pixels and adjacent integrated readout circuitry.

6.4. Sensor characterization

We experimentally confirm the proposed sensor's characteristics, which are device gain, sensitivity, recording speed and imaging ability, to insure the capability for monitoring a pH change that can happen in a biological environment such as that seen by enzymatic reactions ¹²¹.

6.4.1. Test setup

The fabricated device is connected by wire-bonds and encapsulated with epoxy on a PCB which has a chamber for containing a solution on the pixel array. To connect between 24 pins of the LVDS circuit and a PC, the PCB composes includes a FPGA (XC7ATFGG484, Xilinx) as a DRAM interface and a 2-Gb DDR3 SDRAM (MT41J128M16, Micron Tech. Inc.) that temporarily stores the output data. The measurement setup is shown in figure 46. A micro pipette is used to inject the new solution into the chamber with the previous solution. Measuring software installed on the PC automatically transforms the measured data into their output images.

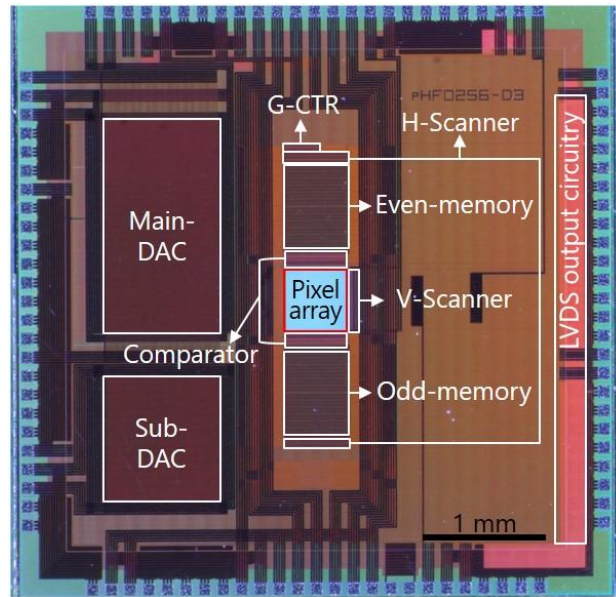


Figure 45 Microphotograph of the fabricated pH image sensor

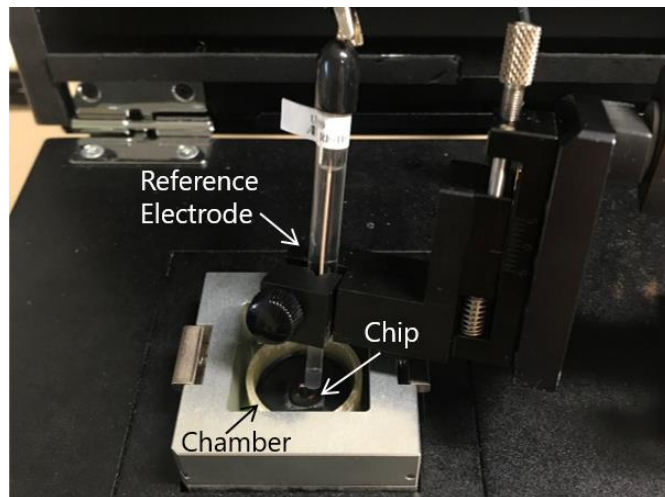


Figure 46 A photo of experimental setup.

6.4.2. Sensing parameters

As mentioned in section 6.2 the V_{OUT} is the measured result including attenuation by the readout circuit. A sensor's gain (g_{sen}) of the whole system can be achieved by measuring a ratio between input and output voltages and can be written as

$$g_{sen} = dV_{OUT} / dV_{ref} \quad (26)$$

Moreover, the equation of a sensor sensitivity (S_{sen}) measured by using various standard pH solutions is defined as

$$S_{sen} = (dV_{OUT} / dpH) \quad (27)$$

So that we can obtain the membrane pH sensitivity (S_{mem}):

$$S_{mem} = (dV_{ref} / dpH) = S_{sen} / g_{sen} \quad (28)$$

The gain was derived as a slope value of the linear region in the graph of V_{ref} versus V_{OUT} , as shown in figure 47. To our sensor, V_{ref} was applied from -0.5 to 3.5 V and the gain was 0.51. The same gains were verified, even though solutions were changed in pH 4.01, 6.86 and 9.18. The gain is previously acquired before starting a biological measurement and is used to compensate the measured V_{OUT} into the potential difference at the membrane surface (V_G).

In order to evaluate the pH sensitivity of the fabricated chip, the V_{OUT} versus pH curve was obtained as shown in figure 48. The array area was immersed sequentially into buffer solutions according to base-to-acid and acid-to-base directions. The result is an average of all pixels (65,536 pixels) of 10 frames, which was measured on an interval of 60 seconds to counteract the drift effect. A change of 27 mV/pH is obtained from the pH calibration curve with a correlation coefficient (R^2) larger than 0.99. Therefore, the membrane pH sensitivity in this CMOS process is 55.1mV/pH which was calculated using the gain. This value is very near to the theoretical pH sensitivity of Ta_2O_5 -gate ISFET that has been reported as 55~57 mV/pH¹¹⁷. Since this result shows a good repeatability during the tests using pH buffers, we verified our sensor can stably operate in the pH range from pH 3 to pH 10.

The next experiment in figure 49 was performed to present a time-course according to the pH change, which implies that a biochemical reaction could be captured when the sensor is used for a cell measurement. The chamber on the sensor was filled with pH 9.18 buffer to give a baseline signal and then pH 4.01 buffer was added to initiate the reaction. In this measurement, the pixel placed at the

center (128, 128) of the array was used, and the V_{ref} of 1.55 V and at 25 MHz ADC clock frequency was applied to achieve a frame rate of 15 frames per second (fps). The histograms presented in figure 50 represent the V_G distribution across all pixels at the point of 9 seconds and demonstrates an excellent uniformity of the pixel responses with the standard variation (σ) of 0.0029 V. Additionally, the σ means a noise signal measured from our sensor. Using this value, the minimum detectable pH change, i.e. pH resolution (pH_{resol}) can be obtained from

$$pH_{resol} = \sigma / S_{mem} \quad (29)$$

Therefore, the calculated pH resolution is about 0.06 pH. The resolution can be degraded at higher ADC clock frequency, due to the increase of noise signals.

Figure 51 shows the same responses can be observed with much higher operating speed of 1933 fps at the other pixel (18, 87). 96 data were recorded in 0.05 seconds. The frame rate was achieved, when the measurement software selectively outputs data of 128 odd rows \times 128 odd columns in the pixel array at an ADC clock frequency of 300 MHz. The improved temporal resolution is expected to make possible to observe small and fast changes of biomolecules in the microcellular level.

Based on the experimental results, we conducted a monitoring of ion diffusion behavior. The recorded data from each pixel are processed to construct 2D images in real-time, as shown in figure 52. We tested the slowest and fastest frame rates, 15 fps and 1933 fps, to verify the imaging ability of our sensor and successfully obtained the images composed of 256×256 pixels and 128×128 pixels, respectively. After dropping a few grains of potassium hydrogen phthalate into a solution of pH 9.18, the transient response and progress of the diffused acid across the sensor surface were monitored at full spatial resolution. This diffusion scenario is analogous to the release of protons from cells and provides spatial and temporal information on how the reaction begins and progresses.

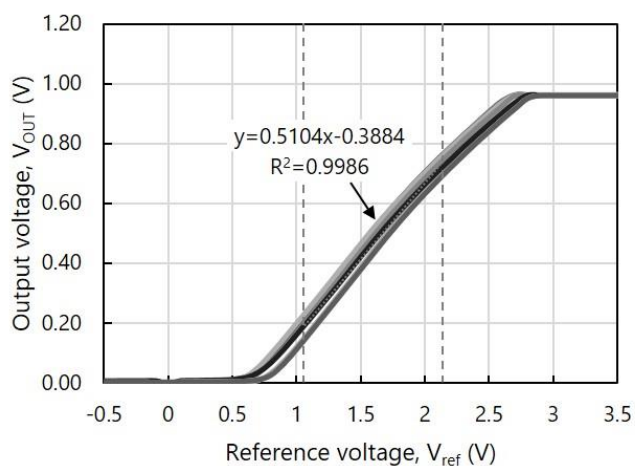


Figure 47 Reference vs. output voltages in pH 4.01 buffer for ten pixels.

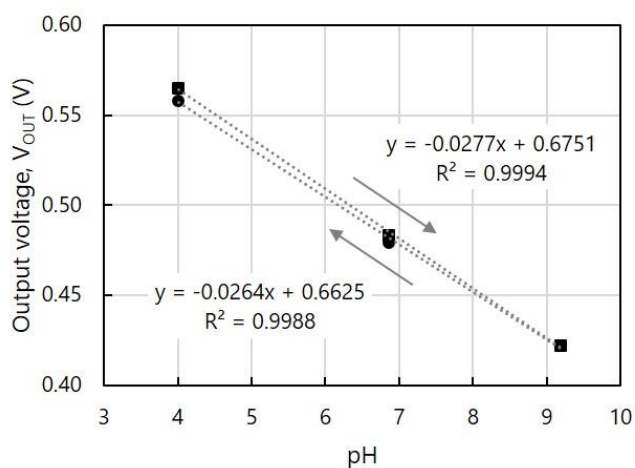


Figure 48 pH calibration curve (n = all pixels of 10 frames. The standard error bar is indicated but smaller than the markers).

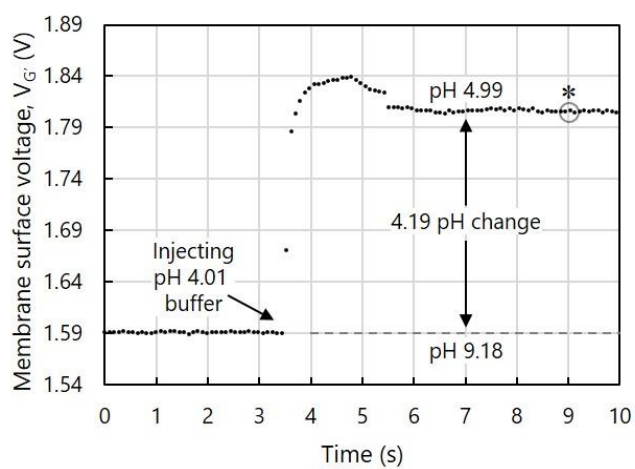


Figure 49 Reaction monitoring of a pH change at $V_{ref} = 1.55$ V and 15 fps.

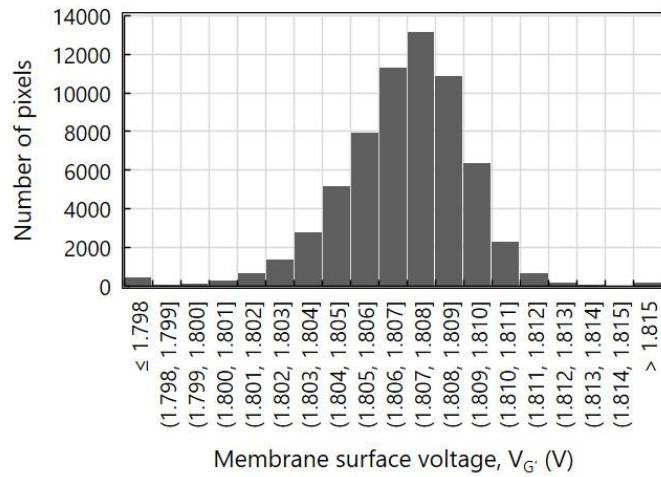


Figure 50 Membrane surface voltage distribution of a frame at 9 s (denoted by * in Figure 49).

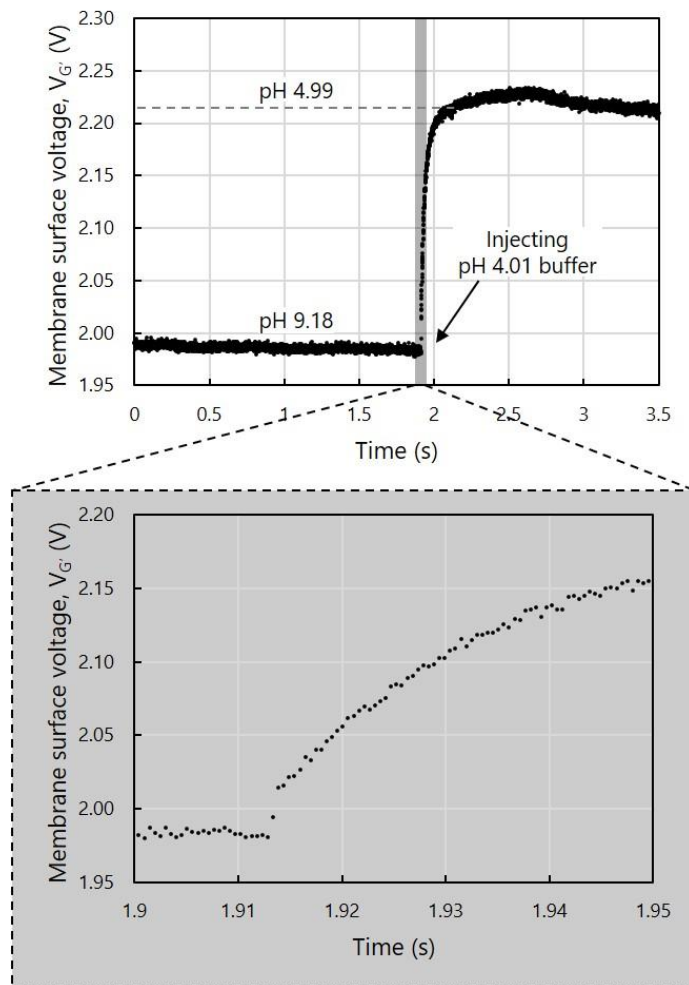


Figure 51 Reaction monitoring of a pH change at 1933 fps. 96 data are recorded in 0.05 s.

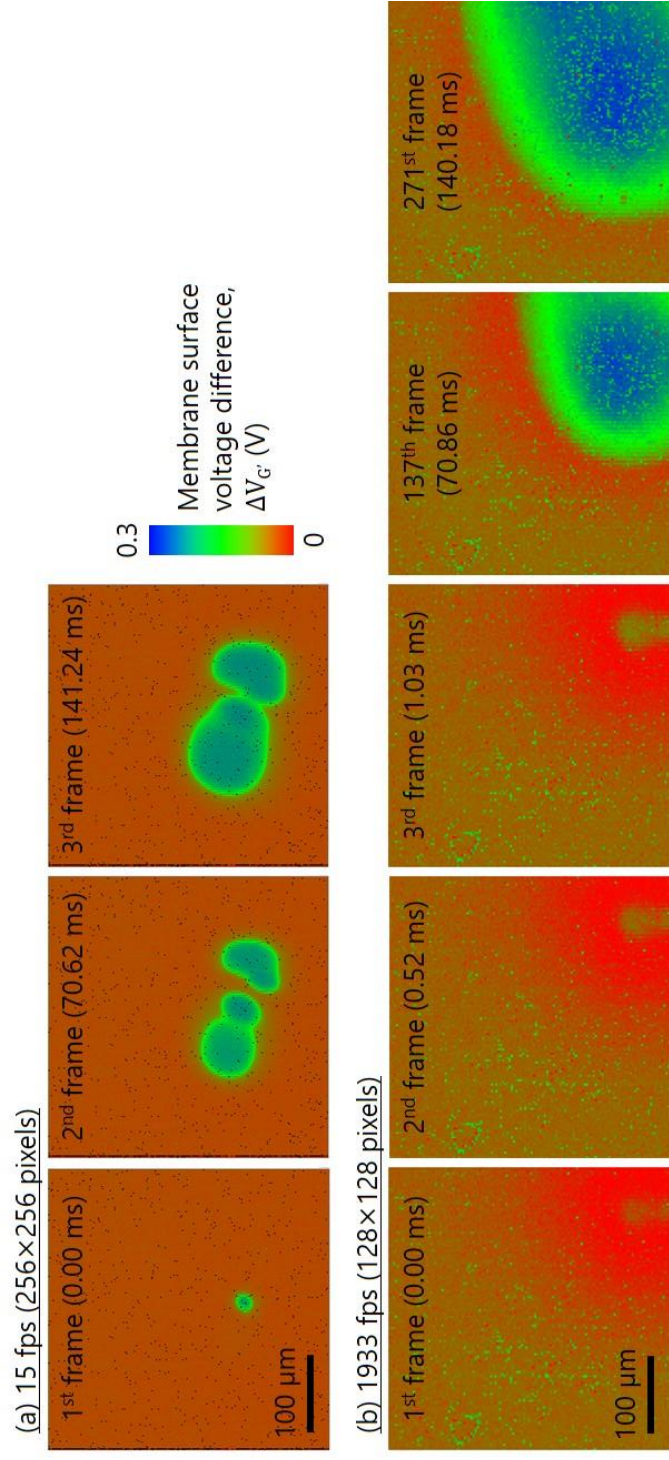


Figure 52 Measured images during about 142 ms after dropping the acid salt into a solution of pH 9.18 at the frame rates of (a) 15 fps and (b) 1933 fps.

6.4.3. Summary

Table 2 summarizes the performance characteristics of the proposed pH image sensor, and table 3 compares the sensor with other state-of-the-art pH image sensors ^{60,106,108,109,115}. Our sensor has not only an excellent spatiotemporal resolution and a pH sensitivity of 55.1 mV/pH, but a real-time imaging ability to visualize the measured information. The attempted fastest frame rate was 1933 fps. To our knowledge, only our sensor provides the highest spatial resolution combining with significantly fast imaging speed compared to the previously reported pH image sensors.

Table 2 Summary of sensor performance parameters

Process technology	1P4M 0.15 μm CMOS
Pixel transistors	3 transistors
Ion-sensitive membrane	Ta ₂ O ₅
Ion sensitive membrane capacitance	1.6 fF
Membrane thickness	300 nm
Pixel pitch	2 \times 2 μm^2
Pixel array	256 \times 256 (programmable 128 \times 128)
Chip size	5.2 \times 5.2 mm ²
Sensing area	1.42 \times 1.42 μm^2
Supply voltage	3.3 V
Maximum frame rate	1933 fps (with 128 \times 128 at 300 MHz)
Membrane surface pH sensitivity	55.1 mV/pH
pH resolution	0.06 pH (at 25 MHz)
pH sensing range	pH 3 ~ pH 10
ADC clock frequency	25 ~ 300 MHz
ADC dynamic range	0 V ~ 1.4 V
ADC effective number of bits	9-bits

Table 3 Comparison of the state-of-the-art pH image sensors

Parameters	Unit	Huang et al. 2015	Cheah et al. 2016	Duarte-Guevara et al. 2017	Jiang et al. 2018	Zeng et al. 2018	This work
CMOS technology	-	0.18 μm	0.35 μm	0.18 μm	65 nm	0.35 μm	0.15 μm
Pixel pitch	$\mu\text{m} \times \mu\text{m}$	10 \times 10	10.2 \times 10.2	7 \times 7	4.4 \times 4.4	18 \times 18	2 \times 2
Pixel array	Pixels	64 \times 64	256 \times 256	1024 \times 1024	512 \times 128	128 \times 128	256 \times 256
Maximum frame rate	fps	1200	500	0.01	375 ^a	3000	1933 ^b
Ion-sensitive membrane	-	Si ₃ N ₄	Ta ₂ O ₅	HfO ₂	Si ₃ N ₄	Si ₃ N ₄	Ta ₂ O ₅
Membrane surface pH sensitivity	mV/pH	103.8 (amplified)	45	45.8	123.8 (amplified)	50	55.1

^aThe maximum frame rate was measured by simulation. ^bThe frame rate was achieved by a sensor operating mode with 128 \times 128 pixels.

6.5. Evaluation of practical spatial resolution

In this section we demonstrate the practical spatial resolution of the proposed pH image sensor. In general, the spatial resolution of the highly integrated ISFET array refers to the number of pixels and pixel pitch. However, the practical spatial resolution has not been tested by standard quality assurance procedures such as an analysis of the modulation transfer function (MTF) in test objects¹²². Therefore, we propose for the first time the use of a line pattern as an evaluation method to compare how different the pixel pitch and practical spatial resolution are in electrochemical imaging applications. Based on the theories of the surface reaction and double layer model described in section 6.2 this test was carried out on the assumption that the pH change can only be measured on the sensor surface. The image blurs due to an ion diffusion in the bulk solution was not considered. Based on the measured results, we assume the reason why the spatial resolution is degraded and verify it with a simulation program.

6.5.1. Experimental evaluation method

In figure 53 (a), patterns of line and space with various widths from 2 μm to 30 μm are arranged in a resolution test chart. This test object was formed on the sensor surface by a photolithography technique. At first, OAP and a photoresist (THMR-iP3100, Tokyo Ohka Kogyo. Inc.) were spin-coated on the top of the sensor at 500 rpm for 5 s and 3000 rpm for 25 s. Before exposing the sample for 9 s at i-line by a mask aligner (MA6, SUSS Micro Tech.), it was post-baked at 100 $^{\circ}\text{C}$ for 90 s. The patterns were developed by NMD-3 (Tokyo Ohka Kogyo Co., Ltd.) and rinsed with deionized water.

To produce a set of test images with different sharpness, the test object prepared on the sensor top was immersed in a solution of pH 9.18. The optical and measured images of patterns are compared to confirm the position where line and space is placed on the pixel array. Due to the low capacitance of the used positive photoresist, the pixel covered with the resin does not have a sufficient pH sensitivity in the applied range of V_{ref} and is presented as a black dot in the measured image. Since the top structure of a pixel consists of a metal top area of $1.42 \mu\text{m} \times 1.42 \mu\text{m}$ and a spacing of $0.58 \mu\text{m}$, the $3.5 \mu\text{m}$ wide lines must cover at least one column in pixels. However, the image of narrower lines than $3.5 \mu\text{m}$ gives us the blurred edges and mismatched shapes, while the image of the lines wider than $4.0 \mu\text{m}$ shows the comparatively well matched and sharp edges of lines, as shown in figure 53 (b) and (c). We think the blurred image is caused by unintended capacitive coupling, and will discuss this further in the next section. From this method, we conclude that the practical spatial resolution of our sensor is about twice that of the pixel pitch. It means that the sensor can distinguish and image objects that are farther than $4.0 \mu\text{m}$ apart. The resolution would be sufficient to distinguish synapses in a low density¹¹².

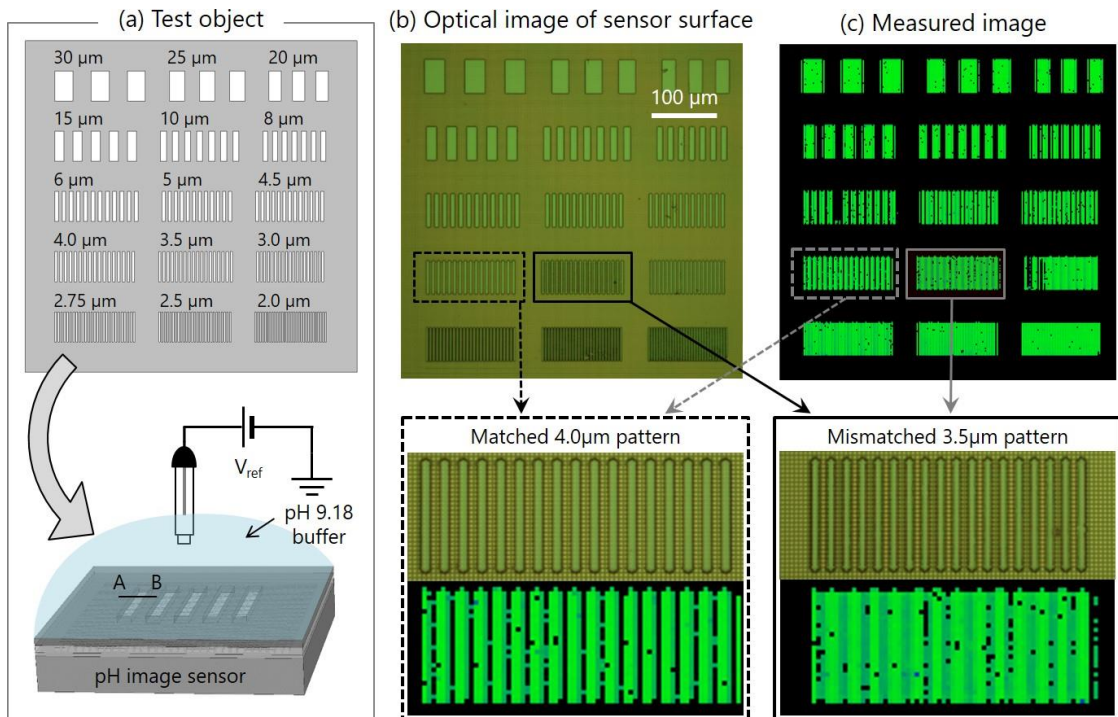


Figure 53 The proposed evaluation method. (a) Test object and measurement setup; (b) optical image of the patterned sensor surface; (c) the measured image. The images of 4.0- μm -wide lines from (b) and (c) shows the comparatively matched edge of lines, but in case of the images of 3.5- μm -wide lines the line edge blurs and mismatches.

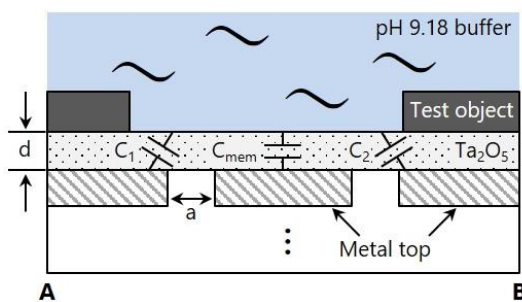
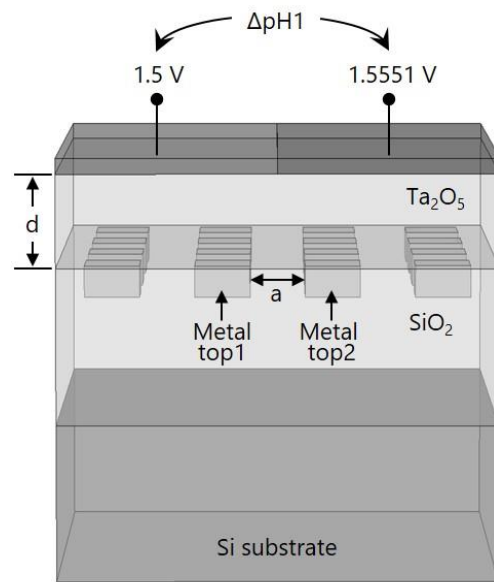
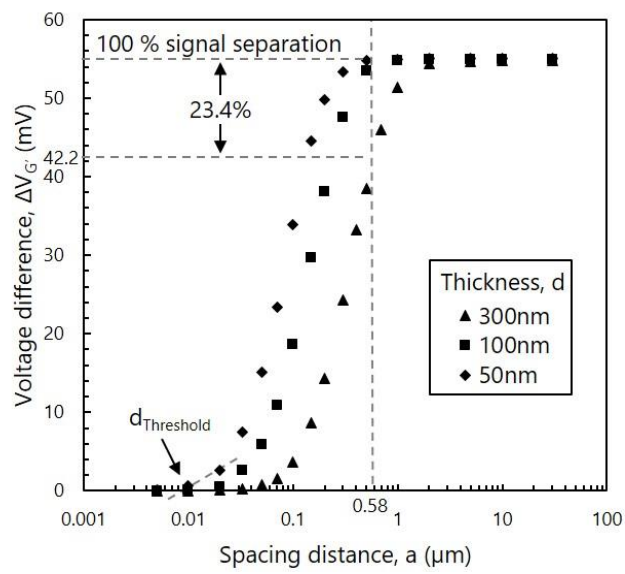


Figure 54 A cross-sectional view of A-B line in figure 53 (a).



(a)



(b)

Figure 55 A simulation (a) model and (b) result to demonstrate the interference potential according to the Ta₂O₅ thicknesses.

6.5.2. Comparison with simulation result

The signal crosstalk observed at the pixels below the object patterns would imply that there are capacitive couplings such as C_1 and C_2 in a Ta_2O_5 membrane as shown schematically in figure 54. The coupling effect among pixels is considered as a main factor to degrade the sharpness in an image of the object. A model of the coupling effect through the Ta_2O_5 membrane covered electrode array is verified by a 3D device simulator (SPECTRA, Link Research Co.), as shown in figure 55 (a). The spacing between metal tops and the dimension of a metal top are $0.58 \mu\text{m}$ and $1.42 \mu\text{m} \times 1.42 \mu\text{m}$, respectively. Membrane surface voltages are differently given at the left and right sides on the model surface, and the difference value is 55.1 mV which corresponds with 1-unit change in pH according to our sensor's sensitivity. Ta_2O_5 membranes with thicknesses of 50, 100, 300 nm are used for investigating the attenuated voltage value by the coupling effect. The surface membrane potential difference ($\Delta V_{G'}$) between metal top 1 and 2 is obtained as below,

$$\Delta V_{G'} = V_{Metal2} - V_{Metal1} \quad (30)$$

The closer the value of $\Delta V_{G'}$ is to 55.1 mV , the less the coupling effect, i.e. the higher discriminating ability between pixels. Figure 55 (b) shows the simulated results depending on the spacing (a) between the metal top 1 and 2, and the membrane thickness (d). From this graph, we verified that the coupling effect decreased according to the increased spacing distance and the declined effect emerged as the distinguishable voltage difference when the spacing is expanding to a particular distance ($d_{\text{Threshold}}$). Moreover, it shows that the $d_{\text{Threshold}}$ starting to occur the voltage difference was shifted inversely proportional to the Ta_2O_5 membrane thickness. In case of our sensor containing the spacing distance of $0.58 \mu\text{m}$ and the membrane thickness of 300 nm, the voltage difference of 42.2 mV was occurring. In other words, the changed surface potential on nearby metal tops transmitted through the Ta_2O_5 membrane and reached into the metal top 1 as much as 23.4 % of the measured value in the metal top 2. Using the sensor with the 300-nm-thick Ta_2O_5 membrane, the crosstalk signal is decreased below 1 % when metal tops place more than $4 \mu\text{m}$ away. It supports that the practical spatial resolution of $4 \mu\text{m}$ previously determined by the experiment in section 6.5.1 was reasonable.

Based on these results, we suggest that the spatial resolution of electrochemical image sensors should be redefined as an importance performance characteristic separated from the pixel pitch. Owing to enhance the practical spatial resolution of our sensor, we will explore new sensor designs considered the membrane thickness and pixel spacing distance as well as measures such as a lift-off process of creating patterns of the membrane on metal tops.

Concluding remarks

To analyze the very complexing chemical communication in the brain, it is very important to have a multiple monitoring capability such as spatial, temporal and quantitative information on individual chemicals. In order to get the multiple monitoring of more than one hundred of neurotransmitters and their co-releasing combination, the possibility of selection of elements is of interest.

In the first of this thesis, we have shown the possibility of multiple monitoring of two neurotransmitters and H^+ ions by the enzyme-immobilization technique that is the integration of an imaging device technique and ISFET based enzyme sensors²⁷. The most important advantages of this technique are that we can not only simply change the kinds of proton-consuming or-generating enzymes according to the neurotransmitters wishing to analyze, but also immobilize them in a desired shape on a pH image sensor by photolithography technology.

Next, based on this technique, we have developed a bio-image sensor that can simultaneously image the spatial and temporal distribution of multi-neurotransmitters with the reduced crosstalk signals. The porous barrier layers and microhole array constructed on a pH image sensor provided the enhanced spatial resolution by minimizing signal overlap by H^+ diffusion after enzymatic reaction, as well as most suitable spacing and thickness among the enzyme-immobilized pixels and the null pH sensor. Since diffusions of biomolecules are unavoidable at measurements in biological environment, the suggested diffusion preventing means will be very useful for using electrochemical biosensor. Multi-detection ability of the fabricated bio-image sensor was demonstrated to obtain simultaneous imaging of the concentration gradients of ATP and ACh in real-time. The bio-image sensor combined with the microhole array is not mentioned in this thesis, because the study has been continued by other master student. The sensor with microhole array could also enhance the discrimination ability of chemicals.

In the last section, we also attempted to improve the sensor performance, such as smaller pixel pitch and higher imaging speed for enhancing spatio-temporal resolution of our pH image sensor³⁰. New circuit designs were considered for the smaller pixel structure and efficient readout. The fabricated sensor's



Figure 56 The great discovery and new viewpoint brought by new analysis tool.

characteristics were experimentally demonstrated and compared to those of the state-of-the-art pH image sensors. Notably, our sensor had the smallest pitch of 2 μm with quite a high frame speed of 1933 fps. In order to evaluate the practical, spatial resolution of biochemical image sensors or arrays, we proposed the evaluation method at first and discussed the results and reasons why the designed pixel pitch and the experimentally obtained practical spatial resolution were different. We believe that these results are able to alert other researchers to the existence of other factors relating to the imaging resolution of various biochemical platforms based on CMOS process.

As a further work, we will move to apply this bio-image sensor to measure chemical signals in the brains. Since the biochemical imaging is the recently flourishing area, it is expected that there are many challenges for actual application of our sensor. In case of in vitro drug tests with cultured cells or sliced brains, our sensor might be a very powerful analysis tool due to its bigger range of measurable elements. In case of in vivo or implantation experiments, as same as the fundamental problems of semiconductor based ISFET sensors, the stable potential in liquid for operating ISFET, the device size such as reference electrode and peripheral circuits and the flexibility of sensor substrates should be considered. Additionally, the mutual influence between the immobilized enzymes on our sensor and cells needs to be surveyed because cells also widely use the enzymatic reactions for their metabolism. Finally, when the usefulness of the sensor is going to be obvious, the database of sensing information according to the pair of an enzyme and a neurotransmitter will be necessary to customize.

New tools always bring new perspectives with us, like the first microscope in figure 56 did that. I wish that our effort could be one step for the better future. Thank you for reading my thesis. I hope you enjoyed reading it.

References

1. Pellerin, L. & Magistretti, P. J. Neuroscience. Let there be (NADH) light. *Science*. **305**, 50–52 (2004).
2. Yu, Y. et al. Antidepressant-like effect of trans-resveratrol in chronic stress model: Behavioral and neurochemical evidences. *J. Psychiatr. Res.* **47**, 315–322 (2013).
3. Stasiak, A. et al. Effects of novel monoamine oxidases and cholinesterases targeting compounds on brain neurotransmitters and behavior in rat model of vascular dementia. *Curr. Pharm. Des.* **20**, 161–171 (2014).
4. Tomkins, D. M. & Sellers, E. M. Addiction and the brain: The role of neurotransmitters in the cause and treatment of drug dependence. *Cmaj* **164**, 817–821 (2001).
5. Mathew, S. J., Coplan, J. D. & Gorman, J. M. Neurobiological mechanisms of social anxiety disorder. *Am. J. Psychiatry* **158**, 1558–1567 (2001).
6. Anisman, H., Merali, Z. & Hayley, S. Neurotransmitter, peptide and cytokine processes in relation to depressive disorder: Comorbidity between depression and neurodegenerative disorders. *Prog. Neurobiol.* **85**, 1–74 (2008).
7. Barone, P. Neurotransmission in Parkinson's disease: beyond dopamine. *Eur. J. Neurol.* **17**, 364–376 (2010).
8. Fisher, R. S. & Velasco, A. L. Electrical brain stimulation for epilepsy. *Nat. Rev. Neurol.* **10**, 261–270 (2014).
9. Normann, R. A. & Fernandez, E. Clinical applications of penetrating neural interfaces and Utah Electrode Array technologies. *J. Neural Eng.* **13**, 061003 (2016).
10. Maynard, E. M., Nordhausen, C. T. & Normann, R. A. The Utah Intracortical Electrode Array: A recording structure for potential brain-computer interfaces. *Electroencephalogr. Clin. Neurophysiol.* **102**, 228–239 (1997).
11. Hnasko, T. S. & Edwards, R. H. Neurotransmitter corelease: mechanism and physiological role. *Annu. Rev. Physiol.* **74**, 225–43 (2012).
12. Barker, D. J., Root, D. H., Zhang, S. & Morales, M. Multiplexed neurochemical signaling by neurons of the ventral tegmental area. *J. Chem. Neuroanat.* **73**, 33–42 (2016).
13. Vaaga, C. E., Borisovska, M. & Westbrook, G. L. Dual-transmitter neurons: Functional implications of co-release and co-transmission. *Curr. Opin. Neurobiol.* **29**, 25–32 (2014).

14. Wei, W. et al. An implantable microelectrode array for simultaneous L-glutamate and electrophysiological recordings in vivo. *Microsystems & Nanoeng.* **1**, 15002 (2015).
15. Cordeiro, C. A. et al. In vivo continuous and simultaneous monitoring of brain energy substrates with a multiplex amperometric enzyme-based biosensor device. *Biosens. Bioelectron.* **67**, 677–686 (2015).
16. Fedorowski, J. & LaCourse, W. R. A review of pulsed electrochemical detection following liquid chromatography and capillary electrophoresis. *Anal. Chim. Acta* **861**, 1–11 (2015).
17. Bovetti, S., Moretti, C. & Fellin, T. Mapping brain circuit function in vivo using two-photon fluorescence microscopy. *Microsc. Res. Tech.* **77**, 492–501 (2014).
18. Johnsen, E., Leknes, S., Wilson, S. R. & Lundanes, E. Liquid chromatography-mass spectrometry platform for both small neurotransmitters and neuropeptides in blood, with automatic and robust solid phase extraction. *Sci. Rep.* **5**, 1–8 (2015).
19. Polcari, D., Dauphin-Ducharme, P. & Mauzeroll, J. Scanning Electrochemical Microscopy: A Comprehensive Review of Experimental Parameters from 1989 to 2015. *Chem. Rev.* **116**, 13234–13278 (2016).
20. SECM150. Bio-Logic Science Instruments (2019). Available at: <https://www.biologic.net/products/scanning-probe-workstation/secm150/>. (Accessed: 15th May 2019)
21. Huang, L. et al. Recent Advances in Scanning Electrochemical Microscopy for Biological Application. *Materials (Basel)*. **11**, 1389 (2018).
22. Ichimura, T., Chiu, L., Fujita, K., Machiyama, H. & Kawata, S. Visualizing the appearance and disappearance of the attractor of differentiation using Raman spectral imaging. *Nat. Publ. Gr.* **5**, 1–3 (2015).
23. So, P. T. C., Dong, C. Y., Masters, B. R. & Berland, K. M. Two-Photon Excitation Fluorescence Microscopy. *Annu. Rev. Biomed. Eng.* **2**, 399–429 (2000).
24. Fu, D., Holtom, G., Freudiger, C., Zhang, X. & Xie, X. S. Hyperspectral Imaging with Stimulated Raman Scattering by Chirped Femtosecond Lasers. *J. Phys. Chem. B* **117**, 4634–4640 (2013).
25. Ikami, H. I. M. et al. Ultrafast confocal fluorescence microscopy beyond the fluorescence lifetime limit. *Optica* **5**, 117–126 (2018).
26. Perry, M., Li, Q. & Kennedy, R. T. Review of recent advances in analytical techniques for the determination of neurotransmitters. *Anal. Chim. Acta* **653**, 1–22 (2009).
27. Lee, Y.-N. et al. Development of an ATP and hydrogen ion image sensor using a patterned apyrase-immobilized membrane. *Talanta* **161**, 419–424 (2016).
28. Lee, Y.-N. et al. A bio-image sensor for simultaneous detection of multi-neurotransmitters. *Talanta* **179**, 569–574 (2018).
29. Ogaeri, Y. et al. Reduced signal crosstalk multi neurotransmitter image sensor by microhole array structure. *Jpn. J. Appl. Phys.* **57**, (2018).
30. Lee, Y. et al. High-density 2- μm -pitch pH image sensor with high-speed operation up to 1933

- fps. *IEEE Trans. Biomed. Circuits Syst.* **13**, 352–363 (2019).
31. Lallement, G., Moser, N. & Pantelis, G. Bio-inspired pH sensing using Ion Sensitive Field Effect Transistors. *2016 IEEE International Symposium on Circuits and Systems (ISCAS)* 2835–2838 (2016).
 32. Bausells, J., Carrabina, J., Errachid, A. & Merlos, A. Ion-sensitive field-effect transistors fabricated in a commercial CMOS technology. *Sensors Actuators, B Chem.* **57**, 56–62 (1999).
 33. Lee, C. S., Kyu Kim, S. & Kim, M. Ion-sensitive field-effect transistor for biological sensing. *Sensors* **9**, 7111–7131 (2009).
 34. Bart, H. van der Schoot & Piet, B. ISFET based enzyme sensors. *Biosensors* **3**, 161–186 (1987).
 35. Levine, P. M., Gong, P., Levicky, R. & Shepard, K. L. Real-time, multiplexed electrochemical DNA detection using an active complementary metal-oxide-semiconductor biosensor array with integrated sensor electronics. *Biosens. Bioelectron.* **24**, 1995–2001 (2009).
 36. Hattori, T. & Sawada, K. 16K Array Charge Coupled Device Multi-Ion Image Sensors for 16K Array Charge Coupled Device Multi-Ion Image Sensors for Simultaneous Determination of Distributions of Sodium and Potassium Ions. *Sensors Mater.* **27**, 1023–1034 (2015).
 37. Kim, J. Y. et al. Multiplex electrical detection of avian influenza and human immunodeficiency virus with an underlap-embedded silicon nanowire field-effect transistor. *Biosens. Bioelectron.* **55**, 162–167 (2014).
 38. Zhang, Q. et al. Polyaniline-functionalized ion-sensitive floating-gate FETs for the on-chip monitoring of peroxidase-catalyzed redox reactions. *Electrochim. Acta* **261**, 256–264 (2018).
 39. Fossum, E. R. & Hondongwa, D. B. A review of the pinned photodiode for CCD and CMOS image sensors. *IEEE J. Electron Devices Soc.* **2**, 33–43 (2014).
 40. Werner, C. F., Takenaga, S., Taki, H., Sawada, K. & Schöning, M. J. Comparison of label-free ACh-imaging sensors based on CCD and LAPS. *Sensors Actuators, B Chem.* **177**, 745–752 (2013).
 41. Barbe, D. F. Imaging devices using the charge-coupled concept. *Proc. IEEE* **63**, 38–67 (1975).
 42. Fossum, E. R. CMOS image sensors: electronic camera-on-a-chip. *IEEE Trans. Electron Devices* **44**, 1689–1698 (1997).
 43. Lyu, T., Yao, S., Nie, K. & Xu, J. A 12-bit high-speed column-parallel two-step single-slope analog-to-digital converter (ADC) for CMOS image sensors. *Sensors (Basel)*. **14**, 21603–21625 (2014).
 44. Moser, N., Lande, T. S., Toumazou, C. & Georgiou, P. ISFETs in CMOS and Emergent Trends in Instrumentation: A Review. *IEEE Sens. J.* **16**, 6496–6514 (2016).
 45. Huang, X. et al. A 64×64 1200fps CMOS ion-image sensor with suppressed fixed-pattern-noise for accurate high-throughput DNA sequencing. *2014 Symposium on VLSI Circuits Digest of Technical Papers* 1–2 (2014). doi:10.1109/VLSIC.2014.6858409
 46. Ballini, M. et al. A 1024-channel CMOS microelectrode array with 26,400 electrodes for recording and stimulation of electrogenic cells in vitro. *IEEE J. Solid-State Circuits* **49**, 2705–

- 2719 (2014).
47. van Hal, R. E. G., Eijkel, J. C. T. & Bergveld, P. A general model to describe the electrostatic potential at electrolyte oxide interfaces. *Adv. Colloid Interface Sci.* **69**, 31–62 (1996).
 48. Lan, W.-J. et al. Paper-based electroanalytical devices with an integrated stable reference electrode. *Lab Chip* **13**, 4103–4108 (2013).
 49. Huang, I. & Huang, R. Fabrication and characterization of a new planar solid-state reference electrode for ISFET sensors. *Thin Solid Films* **406**, 255–261 (2002).
 50. Abe, H., Esashi, M. & Matsuo, T. ISFET's using inorganic gate thin films. *IEEE Trans. Electron Devices* **26**, 1939–1944 (1979).
 51. Chien, F. S. S. et al. Nanometer-scale conversion of Si₃N₄ to SiO_x. *Appl. Phys. Lett.* **76**, 360–362 (2000).
 52. Hiemstra, T., Van Riemsdijk, W. H. & Bolt, G. H. Multisite proton adsorption modeling at the solid/solution interface of (hydr)oxides: A new approach: I. Model description and evaluation of intrinsic reaction constants. *J. Colloid Interface Sci.* **133**, 91–104 (1989).
 53. Parizi, K. B., Xu, X., Pal, A., Hu, X. & Philip Wong, H. S. ISFET pH Sensitivity: Counter-Ions Play a Key Role. *Sci. Rep.* **7**, 1–10 (2017).
 54. Magnotta, V. A. et al. Detecting activity-evoked pH changes in human brain. *Proc. Natl. Acad. Sci.* **109**, 8270–8273 (2012).
 55. Liu, R. et al. High Density Individually Addressable Nanowire Arrays Record Intracellular Activity from Primary Rodent and Human Stem Cell Derived Neurons. *Nano Lett.* **17**, 2757–2764 (2017).
 56. Ha, S. et al. Silicon-Integrated High-Density Electroocortical Interfaces. *Proc. IEEE* **105**, 11–33 (2017).
 57. Maharbiz, M. M., Muller, R., Alon, E., Rabaey, J. M. & Carmena, J. M. Reliable Next-Generation Cortical Interfaces for Chronic Brain-Machine Interfaces and Neuroscience. *Proc. IEEE* **105**, 73–82 (2017).
 58. Jäckel, D. et al. Combination of High-density Microelectrode Array and Patch Clamp Recordings to Enable Studies of Multisynaptic Integration. *Sci. Rep.* **7**, 978 (2017).
 59. Huang, X. et al. A Dual-Mode Large-Arrayed CMOS ISFET Sensor for Accurate and High-Throughput pH Sensing in Biomedical Diagnosis. *IEEE Trans. Biomed. Eng.* **62**, 2224–2233 (2015).
 60. Zeng, J., Miscourides, N. & Georgiou, P. A 128×128 Current-Mode Ultra-High Frame Rate ISFET Array for Ion Imaging. *2018 IEEE International Symposium on Circuits and Systems (ISCAS)* 1–5 (2018).
 61. Nemeth, B., Piechocinski, M. S. & Cumming, D. R. S. High-resolution real-time ion-camera system using a CMOS-based chemical sensor array for proton imaging. *Sensors Actuators, B Chem.* **171–172**, 747–752 (2012).
 62. Nakazato, K. An Integrated ISFET Sensor Array. *Sensors (Basel)* **9**, 8831–8851 (2009).

63. Polo, E. & Kruss, S. Nanosensors for neurotransmitters Young Investigators in analytical and bioanalytical science. *Anal. Bioanal. Chem.* **408**, 2727–2741 (2016).
64. Hizawa, T., Sawada, K., Takao, H. & Ishida, M. Fabrication of a two-dimensional pH image sensor using a charge transfer technique. *Sensors Actuators, B Chem.* **117**, 509–515 (2006).
65. Smith, S. K. et al. Simultaneous Voltammetric Measurements of Glucose and Dopamine Demonstrate the Coupling of Glucose Availability with Increased Metabolic Demand in the Rat Striatum. *ACS Chem. Neurosci.* **8**, 272–280 (2017).
66. Yakushenko, A., Schöps, V., Mayer, D., Offenhäusser, A. & Wolfrum, B. On-chip fast scan cyclic voltammetry for selective detection of redox active neurotransmitters. *Phys. Status Solidi Appl. Mater. Sci.* **211**, 1364–1371 (2014).
67. Dragas, J. et al. In Vitro Multi-Functional Microelectrode Array Featuring 59760 Electrodes, 2048 Electrophysiology Channels, Stimulation, Impedance Measurement, and Neurotransmitter Detection Channels. *IEEE J. Solid-State Circuits* **52**, 1–15 (2017).
68. Rama, E. C., Costa-García, A. & Fernández-Abedul, M. T. Pin-based electrochemical glucose sensor with multiplexing possibilities. *Biosens. Bioelectron.* **88**, 34–40 (2017).
69. Wang, J., Liu, G. & Merkoç i, A. Electrochemical coding technology for simultaneous detection of multiple DNA targets. *J. Am. Chem. Soc.* **125**, 3214–3215 (2003).
70. Leonard, K. C. & Bard, A. J. The study of multireactional electrochemical interfaces via a tip generation/substrate collection mode of scanning electrochemical microscopy: The hydrogen evolution reaction for Mn in acidic solution. *J. Am. Chem. Soc.* **135**, 15890–15896 (2013).
71. Obien, M. E. J., Deligkaris, K., Bullmann, T., Bakkum, D. J. & Frey, U. Revealing neuronal function through microelectrode array recordings. *Front. Neurosci.* **9**, 423 (2015).
72. Massicotte, G., Carrara, S., Di Micheli, G. & Sawan, M. A CMOS Amperometric System for Multi-Neurotransmitter Detection. *IEEE Trans. Biomed. Circuits Syst.* **10**, 731–741 (2016).
73. Zimmermann, H. ATP and acetylcholine, equal brethren. *Neurochem. Int.* **52**, 634–648 (2008).
74. Burnstock, G. Adenosine Triphosphate (ATP). *Encycl. Neurosci.* **1**, 105–113 (2010).
75. Hasselmo, M. E. The role of acetylcholine in learning and memory. *Curr. Opin. Neurobiol.* **16**, 710–715 (2006).
76. Wang, C., Huang, C. Y. C. & Lin, W. C. Optical ATP biosensor for extracellular ATP measurement. *Biosens. Bioelectron.* **43**, 355–361 (2013).
77. Koizumi, S., Fujishita, K. & Inoue, K. Regulation of cell-to-cell communication mediated by astrocytic ATP in the CNS. *Purinergic Signal.* **1**, 211–217 (2005).
78. Moreira, F. T. C., Sale, M. G. F. & Di Lorenzo, M. Towards timely Alzheimer diagnosis: A self-powered amperometric biosensor for the neurotransmitter acetylcholine. *Biosens. Bioelectron.* **87**, 607–614 (2017).
79. Watanabe, M., Kimura, A., Akasaka, K. & Hayashi, S. Determination of acetylcholine in human blood. *Biochem. Med. Metab. Biol.* **36**, 355–362 (1986).
80. Stillman, M. J., Shukitt-Hale, B., Kong, R. M., Levy, A. & Lieberman, H. R. Elevation of

- hippocampal extracellular acetylcholine levels by methoctramine. *Brain Res. Bull.* **32**, 385–389 (1993).
81. Smart, J. L. & McCammon, J. A. Analysis of synaptic transmission in the neuromuscular junction using a continuum finite element model. *Biophys. J.* **75**, 1679–1688 (1998).
 82. Silinsky, B. E. M. On the association between transmitter secretion and the release of adenine nucleotides from mammalian motor nerve terminals. *J. Physiol.* **247**, 145–162 (1975).
 83. Burnstock, G. The Concept of Cotransmission: Focus on ATP as a Cotransmitter and its Significance in Health and Disease. *Eur. Rev.* **22**, 1–17 (2014).
 84. Kåhlin, J. et al. The human carotid body releases acetylcholine, ATP and cytokines during hypoxia. *Exp. Physiol.* **8**, 1–23 (2014).
 85. Redman, R. S. & Silinsky, E. M. ATP released together with acetylcholine as the mediator of neuromuscular depression at frog motor nerve endings. *J. Physiol.* **477**, 117–27 (1994).
 86. Poelchen, W., Sieler, D., Wirkner, K. & Illes, P. Co-transmitter function of ATP in central catecholaminergic neurons of the rat. *Neuroscience* **102**, 593–602 (2001).
 87. Piskuric, N. a, Zhang, M., Vollmer, C. & Nurse, C. a. Potential roles of ATP and local neurons in the monitoring of blood O₂ content by rat aortic bodies. *Exp. Physiol.* **99**, 248–61 (2014).
 88. Huckstepp, R. T. R., Llaudet, E. & Gourine, A. V. CO₂-Induced ATP-Dependent Release of Acetylcholine on the Ventral Surface of the Medulla Oblongata. *PLoS ONE* **11**, e0167861 (2016).
 89. Migita, S., Ozasa, K., Tanaka, T. & Haruyama, T. Enzyme-based field-effect transistor for adenosine triphosphate (ATP) sensing. *Anal. Sci.* **23**, 45–48 (2007).
 90. Lee, S. R. et al. Development of a highly-sensitive acetylcholine sensor using a charge-transfer technique on a smart biochip. *TrAC - Trends Anal. Chem.* **28**, 196–203 (2009).
 91. Futagawa, M. et al. Fabrication of a 128×128 Pixels Charge Transfer Type Hydrogen Ion Image Sensor. *IEEE Trans. Electron Devices* **60**, 2634–2639 (2013).
 92. Bai, H., Xu, J., Zhang, Y., Liu, X. & Rojas, O. J. Dynamics of cyclodimerization and viscoelasticity of photo-crosslinkable PVA. *J. Polym. Sci. Part B Polym. Phys.* **b**, 345–355 (2015).
 93. Sassolas, A., Blum, L. J. & Leca-Bouvier, B. D. Immobilization strategies to develop enzymatic biosensors. *Biotechnol. Adv.* **30**, 489–511 (2012).
 94. Nemani, K. V, Moodie, K. L., Brennick, J. B., Su, A. & Gimi, B. In vitro and in vivo evaluation of SU-8 biocompatibility. *Mater. Sci. Eng. C* **33**, 4453–4459 (2013).
 95. Zhu, C. et al. Electrochemical Sensors and Biosensors Based on Nanomaterials and Nanostructures. *Anal. Chem* **87**, 230–249 (2015).
 96. Nakamoto, S., Ito, N., Kuriyama, T. & Kimura, J. A lift-off method for patterning enzyme-immobilized membranes in multi-biosensors. *Sensors and Actuators* **13**, 165–172 (1988).
 97. Long, G. L. & Winefordner, J. D. Limit of Detection: A Closer Look at the IUPAC Definition. *Anal. Chem.* **55**, 712A-724A (1983).

98. Lee, S. H. & Rasaiah, J. C. Proton transfer and the mobilities of the H⁺ and OH⁻ ions from studies of a dissociating model for water. *J. Chem. Phys.* **135**, 124505 (2011).
99. Zhu, X.-H. et al. Quantitative Imaging of Energy Expenditure in Human Brain. *Neuroimage* **60**, 2107–2117 (2013).
100. Campo, A. del & Greiner, C. SU-8: a photoresist for high-aspect-ratio and 3D submicron lithography. *J. Micromechanics Microengineering* **17**, R81–R95 (2007).
101. Chang, C.-J., Yang, C.-S., Lan, L.-H., Wang, P.-C. & Tseng, F.-G. Fabrication of a SU-8-based polymer-enclosed channel with a penetrating UV/ozone-modified interior surface for electrokinetic separation of proteins. *J. Micromechanics Microengineering* **20**, 115031 (2010).
102. Wang, T. M., Holzhausen, L. C. & Kramer, R. H. Imaging an optogenetic pH sensor reveals that protons mediate lateral inhibition in the retina. *Nat. Neurosci.* **17**, 262–268 (2014).
103. Wu, Y. et al. PH imaging of mouse kidneys in vivo using a frequency-dependent paraCEST agent. *Magn. Reson. Med.* **75**, 2432–2441 (2016).
104. Zhou, J., Zhang, L. & Tian, Y. Micro Electrochemical pH Sensor Applicable for Real-Time Ratiometric Monitoring of pH Values in Rat Brains. *Anal. Chem.* **88**, 2113–2118 (2016).
105. Nabovati, G., Ghafar-Zadeh, E. & Sawan, M. A 64 pixel ISFET-based biosensor for extracellular pH gradient monitoring. *Proc. IEEE Int. Symp. Circuits Syst.* 1762–1765 (2015).
106. Duarte-Guevara, C. et al. Characterization of a 1024 × 1024 DG-BioFET platform. *Sensors Actuators, B Chem.* **250**, 100–110 (2017).
107. Kaisti, M., Zhang, Q. & Levon, K. Compact model and design considerations of an ion-sensitive floating gate FET. *Sensors Actuators, B Chem.* **241**, 321–326 (2017).
108. Cheah, B. C. et al. An Integrated Circuit for Chip-Based Analysis of Enzyme Kinetics and Metabolite Quantification. *IEEE Trans. Biomed. Circuits Syst.* **10**, 721–730 (2016).
109. Jiang, Y. et al. A high-sensitivity potentiometric 65-nm CMOS ISFET sensor for rapid E. coli Screening. *IEEE Trans. Biomed. Circuits Syst.* **12**, 402–415 (2018).
110. Hu, Y. & Georgiou, P. A robust ISFET pH-measuring front-end for chemical reaction monitoring. *IEEE Trans. Biomed. Circuits Syst.* **8**, 177–185 (2014).
111. Duarte-Guevara, C. et al. Enhanced biosensing resolution with foundry fabricated individually addressable dual-gated ISFETs. *Anal. Chem.* **86**, 8359–8367 (2014).
112. Druckmann, S. et al. Structured Synaptic Connectivity between Hippocampal Regions. *Neuron* **81**, 629–640 (2014).
113. Ogi, J. et al. Twenty-four-micrometer-pitch microelectrode array with 6912-channel readout at 12 kHz via highly scalable implementation for high-spatial-resolution mapping of action potentials. *Biointerphases* **12**, 05F402 (2017).
114. Südhof, T. C. Neurotransmitter release: The last millisecond in the life of a synaptic vesicle. *Neuron* **80**, 675–690 (2013).
115. Huang, X., Guo, J., Yan, M. & Yu, H. A 64x64 1200fps dual-mode CMOS ion-image sensor for accurate DNA sequencing. *20th Asia South Pacific Des. Autom. Conf. ASP-DAC*, 28–29 (2015).

116. Kleinfelder, S., Lim, S., Liu, X. & El Gamal, A. A 10000 frames/s CMOS digital pixel sensor. *IEEE J. Solid-State Circuits* **36**, 2049–2059 (2001).
117. Poghossian, A. S. The super-Nernstian pH sensitivity of Ta₂O₅-gate ISFETs. *Sensors Actuators, B. Chem.* **7**, 367–370 (1992).
118. Butt, H.-J. H. et al. Physics and Chemistry of Interfaces. Physics and Chemistry of Interfaces (Wiley-VCH, 2006). doi:10.1632/074069503X85526
119. Bousse, L., Bousse, L., De Rood, N. F. & Bergveld, P. Operation of Chemically Sensitive Field-Effect Sensors As a Function of the Insulator-Electrolyte Interface. *IEEE Trans. Electron Devices* **30**, 1263–1270 (1983).
120. Shepherd, L. & Toumazou, C. Weak Inversion ISFETs for ultra-low power biochemical sensing and real-time analysis. *Sensors Actuators, B Chem.* **107**, 468–473 (2005).
121. Maleki, N., Kashanian, S., Maleki, E. & Nazari, M. A novel enzyme based biosensor for catechol detection in water samples using artificial neural network. *Biochem. Eng. J.* **128**, 1–11 (2017).
122. Samei, E., Flynn, M. J. & Reimann, D. A. A method for measuring the presampled MTF of digital radiographic systems using an edge test device. *Med. Phys.* **25**, 102–113 (1998).

Acknowledgements

I thank all the people who related me during my Ph.D. course and helped me finish this thesis. Most of all, my endless thanks go to my supervisor Prof. Dr. Kazuaki Sawada. He gave me lots of opportunities to grow myself academically and personally.

Also very thanks to Prof. Jang-Kyoo Shin and Dr. Wanghoon Lee supported me with great mind and thought. Prof. Dr. Schuichi Koizumi in Yamanashi University always has told to me over a variety of topics and shown how various perspective exists in the research world as well as the real world. I am grateful to Prof. Dr. Kazuhiro Takahashi, Prof. Dr. Yasuhiko Ishkawa and Prof. Dr. Toshiaki Hattori for being co-referees of my thesis. Very thanks Prof. Dr. Toshihiko Noda for joining us.

A huge thanks go to all members of the Department of Electrical & Electronic Information Engineering. Especially, to secretary Ms. Roumiko Toyoda and researcher Ms. Tomoko Horio, they are my mentors in every way.

I like to thank all the technical and administrative staffs: Mr. Okumura Koichi, Mr. Fumihiko Dasai, Mr. Yasuyuki Kimura, Mr. Kensuke Murakami, Dr. Tatsuya Yoshimi, Ms. Sachiko Wakazuki, Ms. Miki Taki, Ms. Hiromi Sahara and Ms. Yuko Makino.

Further, I like to thank the other members of the Integrated Biosensor • MEMS group: Dr. Choi Yong Joon, Hayato Kumagai, Toshiaki Takahashi, Yoshitaka Arimi, Yuta Ogaeri, Naoya Shimmyo, Yusuke Nakamura, Yusuke Yamauchi, Yuya Sugihara, Kousuke Go, Reina Teramoto, Sawako Tanaka, Takahiro Shiguma, Ken Oono, Shin Kidane, Takuya Teshima, Atsuya Hirata, Kanata Tanaka, Junpei Uesaka, Ryouto Kanamori, Chinatsu Kawakami, Koutaro Sakamoto and Sylvia Loo Mei Lin.

I owe thanks to the rest of the VBL supporters: Dr. Takeshi Hizawa, Mr. Hiroyuki Takase and Mr. Ashiki Mitsuaki

The very special thanks go to my family who is being well in Korea for all year. I always wish they have joyful days.